Wind Turbine Forward Scatter - Qualitative Analysis, Vital Parameters and Avoidance

Submitted Dissertation at the

Department of Electrical Engineering

of Helmut Schmidt University,
Universität der Bundeswehr Hamburg, Germany

for the degree of

Doktor-Ingenieurs (Doctorate of Engineering)

by

Bilal Raza

Hamburg, Germany 2020

Supervisors:	AkadDir PD Dr.-Ing. Thomas Fickenscher Adj. Ass. Prof. (Griffith University) (Chair of High Frequency Engineering, Helmut Schmidt University, Hamburg, Germany)
	Prof. Dr.-Ing. Heyno Garbe (Institute of Electrical Engineering and Measurement Technology, Leibniz Universität, Hannover, Germany)
	Prof. Dr. rer. nat. habil. Marcus Stiemer (Chair of Theoretical Electrical Engineering and Computational Electromagnetics, Helmut Schmidt University, Hamburg, Germany)
Date of oral defence:	12th May, 2020.

Declaration

I hereby certify that I am the sole author of this thesis and to the best of my knowledge, my thesis does not infringe upon anyone's copyright nor violate any proprietary rights and that any ideas, techniques, quotations, or any other material from the work of other people included in my thesis, published or otherwise, are fully acknowledged in accordance with the standard referencing practices. I declare that this is a true copy of my thesis, including any final revisions, as approved by my thesis committee, and that this thesis has not been submitted for a higher degree to any other University or Institution.

Bilal Raza
Stuttgart,
May, 2020.

Acknowledgements

I would like to express my gratitude and appreciation to everyone who has supported and encouraged me in completing this dissertation. First and foremost, I wish to thank my supervisor PD Dr.-Ing Thomas Fickenscher without whom this research would not have been possible. His expertise, knowledge, discipline, positivity and enthusiasm have been invaluable. In addition to being a dedicated mentor, Dr. Fickenscher has also been a compassionate friend who has supported and guided me throughout this journey and for that I owe him an enormous debt of gratitude. I am extremely grateful to Prof. Dr.-Ing. C. G. Schäffer, Prof. Dr.-Ing Heyno Garbe and Prof. Dr. rer. nat. habil. Marcus Stiemer for their guidance, support and valuable suggestions which have been vital in the successful completion of this work. I would also like to thank them for taking time out of their busy schedules to be a part of the dissertation review committee.

The person with the greatest indirect contribution to this work is my mother Farhat Raza, who has been a constant pillar of strength throughout the years and without whom none of the good things in my life would have been possible. I must express my gratitude to my wife Zahra for her patience and continuous support every step of the way. I must also mention my wonderful children Muaz and Minal for the tremendous joy they bring to my life. A warm thanks to all my dear ones especially Waqas, Kashif, Rayyan, Maira and Humza. Finally, this dissertation is dedicated to my late father Raza Ashraf, who has been my biggest source of inspiration and my strongest role model.

Contents

1 Introduction

The rapid growth in wind energy development in recent years has resulted in wind turbines (WTs) being deployed at an increasing annual global rate of approximately 20% [1]. With each generation of WTs, the rotor diameter and the height of the supporting tower have increased significantly. Initially WTs were typically built on exposed land at high altitudes to take advantage of stronger winds. As their number increased, more and more turbines were being deployed close to more populated areas. The growing number, size and density of WTs are putting them in close proximity of radar and radio communication links, raising concerns about their impact on the performance of these systems. To ensure that the performance of a radar or radio communication system is not severely degraded in the vicinity of wind turbines, it is important to conduct a detailed analysis of the potential wind turbine interference (WTI) based on measurements or simulations. The prediction of WTI allows the planning of mitigative solutions to ensure the coexistence of wind energy and radio communication services. For existing radio links, once new WT installations are set up corrective measures are usually technically complex with high associated costs. For new radar and radio communication set ups, the prediction of interference from existing closeby WTs allows for a better planning of link configurations.

A typical Wind Turbine structure (Fig. 1-1) consists of a reinforced concrete tower, a nacelle which contains most of the fundamental machinery and a rotor with typically three blades usually made up of composite and fiber-glass materials [2, 11]. The rotation of the blades is used to convert the captured wind energy into electric power. The tower is the only part of the turbine that remains static. It carries the weight of the nacelle and the blades, providing stability to the entire WT geometry. Current WT tower height ranges from 40 m to as high as more than 120 m [3]. While

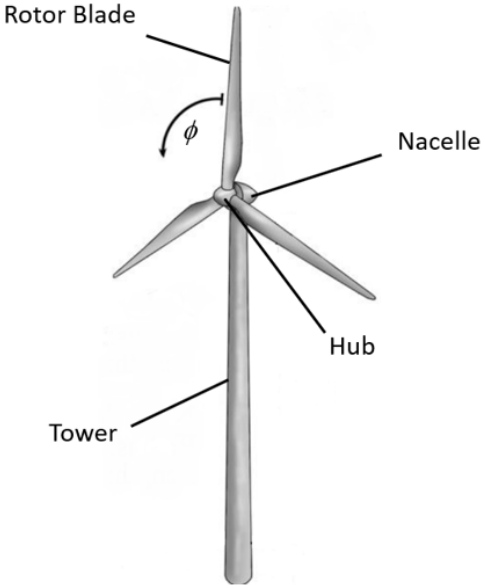

Figure 1-1: Wind Turbine Structure [61]

the earlier structures used a cylindrical tower, a tabular tower of conical shape is used in most of the current turbines [4]. The nacelle is an enclosure that houses all the necessary equipment for electric power generation. Its cover is composed of fiberglass-reinforced plastic and is most commonly rectangular, circular or egg shaped [5]. The rotor of a wind turbine typically consists of a hub and three blades [6]. The earliest wind turbine blades mostly used rectangular or triangular blades. Most blades these days use an airfoil design like that of airplane wings and form a curved structure [7, 39]. High grade fiberglass- reinforced plastic is most commonly used for the material composition of the rotor blades. This provides a high degree of mechanical strength and stiffness to the blades, while maintaining a low overall weight [8]. The rotor blades also contain an internal metallic conductor for lightening protection [4].

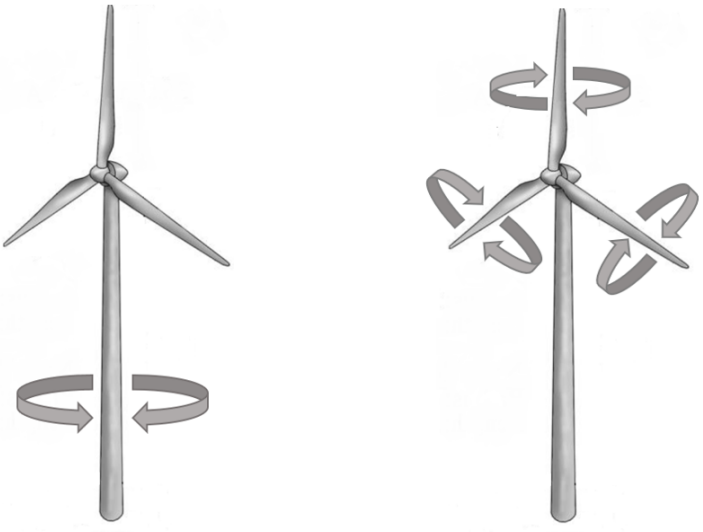

a) b)

Figure 1-2: a) Yaw and b) Pitch control of a Wind Turbine Structure [61]

The design and deployment of wind turbines is carried out aiming to ensure that maximum wind energy is captured and ultimately converted into electrical power. The nacelle contains sensors for the yaw control system (Fig. 1-2 a), to continuously measure the direction and speed of the wind. The average speed and direction of wind is used to change the orientation of the nacelle in order to align the turbine rotor in the direction of maximum wind energy to attain maximum efficiency [9]. This changes the aspect angle of a WT with respect to the antennas of a radar or radio communication system. There is an upper limit to the wind speed that can be handled by a given turbine. Beyond this cutoff speed, the amount of wind energy captured needs to be reduced in order to avoid damaging the turbine. This is achieved by the pitch control of the blades, which makes the blades turn along the longitudinal axis (Fig. 1-2 b) in order to allow the area of the blades cutting through the wind to be reduced [9, 10].

1.1 WTI Mechanisms

Three principle degradation mechanisms have widely been associated with WTI [25, 26]. These are mentioned below:

a) Near Field Effects
When a WT lies within the near field zone of a transmitting or receiving antenna, the prediction of the impact on the radio system becomes very complex, requiring consideration of reactive as well as radiated fields [27].

b) Diffraction
Diffraction of signals by a WT causes areas of increased as well as areas of diminished signal level to be observed beyond its structure [29]. The latter aspect is known as the shadowing effect and causes significantly reduced signal levels directly behind the WT. Diffraction effects occur predominantly in the forward scatter region, which includes a comparatively narrow sector behind the WT (as observed from the transmitter). Diffraction of a signal is independent of the reflective properties of the obstruction and hence each component of a WT geometry may contribute.

c) Reflection
Reflection of signals by a WT is predominantly associated with the backscatter region which includes a relatively wide sector on the sides and in front of the turbine (as observed from the transmitter) [26, 29].
The turbine blades are usually constructed of a fiber glass composite shell and have an internal metallic lightning conductor. At lower frequencies (VHF) the fiberglass in the blades will be transparent with only the metallic lightning conductor having any effect. At higher frequencies the blades become more visible and reflective [30]. The wind turbine tower is a large structure and hence can significantly reflect incident signals. The reflected signals may be observed in the receiver location as a time varying multipath channel due to the rotation of the rotor blades.

The reflected and diffracted signals by a wind turbine contain both amplitude and phase modulation, in synchronization with the rotation of the blades. This amplitude and phase modulation can cause service degradation of radar and radio communication links. Furthermore, the moving

blades cause a certain frequency shift of the signal. For radar systems, oscillatory motion or rotation of an object, or a part of an object, may induce a frequency modulation on the returned signal due to the so-called micro-Doppler effect [31]. Since wind turbines have no bulk motion and only micro-motions due to the rotating blades, such dynamics cause a frequency modulation on the back-scattered signal and will induce micro-Doppler frequency deviation [32, 33]. The Doppler frequency shift generated by micro-motions is a time varying frequency function and imposes a periodic time-varying modulation onto the carrier frequency. Moreover, it causes new features in a target's radar signature. The amplitude and phase modulated signal has a time variance in synchronization with the blade rotation and a frequency deviation is imposed on the diffracted signal [34]. For a target located in the forward scatter region of radar system, the signal is diffracted twice at the rotating blades, once along the forward path and once on the return after being scattered by the target. A strong two-way frequency deviation can cause errors in the measured Doppler spectrum of the target.

To summarize, WTs may cause (forward and backward) scattered signals of dynamic nature owing to the rotating blades. Due to the amplitude and phase modulation of the scattered signals, a certain frequency deviation may be induced on the received signal. The time and frequency characteristics of the scattered signal will depend on various factors like operational frequency, link distances, antenna characteristics and orientations, blade dimensions and shapes, rotational speed/wind speed, rotor angle, pitch and yaw of the turbine.

1.2 Impact of WTI

Services prone to performance degradation by WTI include radio links and radar systems. Radio links prone to WTI may include point to point communication systems [3, 8, 15] and broadcasting services (analogue [17-22] and digital television [15, 23-26]). Radar systems susceptible to WTI include Air Traffic Control Radars [27-32], weather radars, marine radars and VHF Omnidirectional Range (VOR) Navigation systems [33, 34].

a) Impact on Radio Links
There are two main degradation mechanisms that must be considered when a wind turbine is in the proximity of a radio link: diffraction effects due to a potential obstruction of the radio link and reflection of signals from the turbine structure [30, 36]. Near field effects are not as relavant in most practical scenarios and can be simply avoided by safeguarding the antenna terminals [35].

Diffraction effects of Wind turbines can cause serious reductions in the fade margin which in severe cases can result in a complete link failure due to the blocking of the signal. The diffracted signal can cause a time varying amplitude and phase modulation of the signal, which may decrease the overall signal level below critical values. It has traditionally been observed that the strongest impact of signal obstruction is encountered when the wind turbine impedes the first Fresnel zone [38]. Reflection of signals from the physical structure of a turbine gives rise to attenuated, time-delayed, and phase shifted replicas of the original signal, which vary with blade rotation and rotor orientation [40]. This produces a time varying multipath channel which has the potential to decrease the C/I (the carrier-to-interference) ratio well below the minimum requirement for the link.

The performance of the different digital transmission systems under the impact of WTI is yet to be comprehensively assessed and will mainly depend on the modulation and channel coding schemes used [35]. For fixed digital links using a higher order QAM transmission scheme, the time variant WTI may produce a significantly high pre-Viterbi bit error rate (BER) especially if the blades obstruct the line of sight (LOS) path. In analog television services, the amplitude and relative phase difference between transmitted and WT scattered signals can cause the ghosting effect, where a pale shadow appear on viewers' television screens. The same interference signal that may cause ghosting in analog television may not produce a similar effect in a digital television system but can degrade the signal beyond use [5, 43]. For DVB-T standard in Europe and ATSC systems in North America, WTI can force the signal level to be below the operational threshold, significantly distorting the quality of the received video [25, 43, 44].

b) Impact on Radar Systems

The key effects of wind turbines on radar services are beam blockage or desensitation due to obstruction of the radar beam, increase in clutter due to signal scattering, signal modulation in the forward scatter region and the degradation of the target Doppler signal due to the frequency deviation generated by the rotating blades [33, 34, 35, 38, 45, 46].

Target detection may be degraded when the radar beam is obstructed by one or more wind turbines, which may result in the loss of information in a certain area shadowed by the wind farm if a significant angular sector of the radar beam is obstructed [48]. The amplitude and phase modulation by the WT forward scatter may reduce the radar signal strength [49]. Moreover, signals reflected to the radar cause an increase in the clutter strength, which may create false targets or mask real objects [47]. Detection thresholds are also raised as a consequence of increased clutter, which gives rise to reduced detection capability or desensitization within the radar sector containing the wind turbine [49, 50].

Most radar systems have Doppler-based filters to suppress static clutter due to stationary objects. However, the dynamic clutter caused by the rotating blades does not get suppressed by the clutter filters and may be interpreted as a moving target [51]. The frequency deviation associated with the WT (forward and back) scattered signals may cause a degradation of the Doppler signal, making it difficult for the radar to accurately estimate the velocity of the target [52]. The frequency deviation introduced by WT scattered signals may also reduce the ability of a weather radar to accurately estimate wind speed [51]. An additional effect is that if the target is correctly detected, an error in the bearing angle may be encountered [47].

1.3 WTI- Analyses and Avoidance

For the analysis of signals scattered by WTs, several simple scattering models have been presented since the late 1970s. Some of the popular early models for scattering estimation in the UHF band include the ones by

Sengupta [53, 54], the BBC Research Department [32,33] or Van Kats [34]. The International Telecommunication Union (ITU-R) Recommendation ITU-RBT.805 presents a simple scattering model based on a flat metallic approximation of the rotor blades oriented for maximum signal power scattering [36]. The ITU-RBT.1893 was presented to overcome some of the basic limitations of the Rec. ITU-R BT.805 by considering blade shapes closer to those of actual rotor blades and including impact of the WT orientation against the wind [37]. However, all these models have major limitations, since they do not model the signal scattering variation due to blade rotation.

Over the years, WTI studies have mainly focused on the backscatter region, addressing issues such as clutter problems [55]. Consequently, most of the approaches for avoiding and mitigating WTI have been suggested with the primary focus on the WT reflected signals. While RCS has been widely used as the predominant parameter for the characterization of WT backscatter in most studies, it has been argued [19, 56], that the RCS is not applicable to objects on the ground, like a wind turbine. The general definition of the RCS implies a plane wave excitation and far-field condition. In case of a WT, the incident field at the WT has neither constant amplitude nor a uniform phase due to the illuminated ground. Moreover, far field condition for a WT considered as the source of the backscattered signal can easily exceed a distance of tens of kilometers. Hence it has been argued that RCS may not be a figure of merit when dealing with an object on the ground, like a wind turbine [19, 56]. However, RCS continues to be used in most WTI studies. Even global regulatory bodies like World Meteorological Organization (WMO), the European Organization for the Safety of Air Navigation (EUROCONTROL), and the National Telecommunications and Information Administration (NTIA) in North America continue to use RCS for the characterization of WT reflection effects [35, 38]. Other investigations [57, 58] have accounted for the effects of a non-uniform illumination by using target decomposition to divide the WT geometry into small parts that meet the far field criterion followed by coherent integration of the backscattered fields to estimate the so-called near field RCS of turbine. Various studies have used different values and forms of RCS to characterize the WT backscattered signal and the associated micro-Doppler effect [59-63, 72]. The WT backscattered signal has been rigorously studied in literature and the impact has been investigated for services like analog and digital TV [26, 41, 42, 43, 44, 66], Air Traffic Control

(ATC) Radars [30, 57, 67, 69, 80], weather radars [10, 46, 48, 58, 71, 73] and VHF Omnidirectional Range (VOR) Navigation systems [34, 49, 65].

Investigations in the forward scatter region have mostly been carried out by measurements and rigorous time-consuming numerical simulations. The diffraction effects – though well known – have mainly been studied in terms of the shadowing effect and signal blocking [91, 92]. There has not been a conclusive and comprehensive discussion in literature about the amplitude and phase modulation of the forward scattered signal caused by the rotating WT blades which in turn produces a periodic frequency deviation of the signal. Some notable observations are available in literature that underline the importance for a better understanding of the WT diffraction effects. In [76], an investigation of the shadowing effect showed that the WT forward scatter contains a seemingly well shaped pattern of maxima and minima with regions of obstruction loss as well as obstruction gain. In [30], while assessing the field measurement data at Lake Bonney in South Australia, a rapid variation in the received signal level was observed when the signal path was between two WT blades. It was concluded that the diffracted signals from the WT blades interfere constructively and destructively to produce rapid changes in the received signal level. In [75] it was noted that the signal degradation due to WTI reduces with increasing Fresnel zone clearance from the WT blades. In [74], an investigation of the effects of WT blockage on coherent weather radar performance concluded that WTs within a few kilometers of meteorological radars can prevent the radar's beam from correctly shaping and cause considerable radar estimation errors. It was shown that even a single WT blocking the radar beam can cause signal losses more than 2 dB. A comprehensive qualitative analysis of WT forward scatter along with a methodology to estimate the signal variability due to blade rotation in the forward scattering zone had not been established until a Fresnel diffraction modeling technique was presented in [112] which was later used to develop an indepth understanding of the WT forward scatter [122].

Detailed WTI studies can be carried out either by performing field measurements [1, 76, 77, 78, 81], or using a scaled model which reduces the size of a WT to more manageable dimensions for indoor analyses [82-84]. Field measurements need proper planning, extensive data acquisition, high end equipment and have high economical costs, whereas scaling the physical dimensions of a wind turbine can present the difficulty of preserving all complex material properties at the scaled frequency. A less

complicated and more flexible approach is the use of numerical methods and computational electromagnetic (CEM) techniques. Several simulation approaches using 3D simulation software tools based on asymptotic and rigorous techniques have been used for WTI studies with a primary focus on the backscatter region without considering complex scenarios involving ground plane reflections [85-87]. It has been noted that most available techniques are memory intensive for complex scenarios [85, 89]. Other indigenous standalone simulation models have mainly been based on RCS calculations [88, 89]. Other Models using parabolic equation (PE) and physical optics (PO) have been presented in [90-92]. These methods are helpful to get rough estimations but largely ignore diffraction effects and ground plane reflections. An estimation approach presented in [93] considers ground plane effects using image theory, however only backscatter region is considered, and diffraction effects are ignored. It is worth noting that simulation models for a comprehensive characterization of WT forward scatter in complex scenarios have not been presented in literature.

To minimize the impact of WTI, various mitigation techniques have been suggested. For radar systems, various data processing techniques such as adaptive spectrum processing [95], enhanced CFAR [99, 100], moving target detector processing [37], high resolution clutter maps and plot/-track filters [97,99] have been suggested for minimizing the WT clutter. Moreover, areas severely affected by clutter may be covered by a second so-called gap-filler radar [94]. However, these options can incur significant costs. For fixed radio links, improving the directivity of the receiving antenna has been suggested [37] to reinforce the direct signal while attenuating the WT scattered signals. However, this approach is not always applicable in the forward scatter region for cases when WTs are positioned between the transmitting and receiving ends. Another popular approach is to reduce the scattering from a wind turbine through the application of RCS minimization techniques such as the stealth technology to make the wind turbine less visible to a nearby radar and radio communication systems [97, 98]. Covering the blades with radar absorbing material (RAM) is likely to reduce the RCS but is highly impractical [98], since fully treating the blades with RAM may reduce the efficiency of the turbine by changing the airfoil profile of the blade or incurring significant weight penalty. One aspect that has been of primary concern is that a WT should not be installed in locations very close to a radar or radio communication link [47, 102]. The extent of the distance that needs to be maintained depends on the nature

of the communication system. Regulatory bodies for various radar and communication services have produced guidelines which aim to present certain rules-of-thumb and safeguarding zones that should minimize the effects of WTI. EUROCONTROL defines several zones and provides guidelines within each of these zones [29]. These range from "safeguarding zones", within which no wind turbines should be placed, through consultation zones requiring an impact assessment to be conducted, to safe zones in which no impact is expected. The exclusion zones or the safeguarding zones defined for radar systems have mainly been outlined for clutter problems arising from the backscattered signal as well as the shadowing effect due to the blocking of the radar beam. The consultation zones normally extend to a few kilometers and require a proper characterization of the back as well as forward scattered signals. The World Meteorological Organization (WMO) [68] recommends that wind turbines should be placed at distances greater than at least 5 km for C band radar and 10 km for S band radars. These exclusion distances are defined for minimizing the effects of clutter and radar beam blocking by wind turbines. For a radar system that is scanning, it cannot be guaranteed that the radar beam will never be blocked by a WT. Weather radars use pencil beams, and hence transmit the signal to very small sectors. As a weather radar may cover a distance of up to 150–300 km, significantly large geographical areas may be affected by the blocking of the radar beam. According to WMO guidelines, 10% blocking of the beam is the maximum acceptable value and most European countries adhere to this recommendation [101]. In Germany, strong impact of beam blocking is avoided by maintaining the minimum separation between the radar and WTs in accordance with WMO recommendations [37]. However, the impact of the blocking of the radar beam has not been comprehensively investigated from the prospective of the impact on a target located in the forward scatter region. In addition to signal blocking, the phase and amplitude modulation of the WT forward scatter may have an impact on errors in target detection, or in case of weather radars errors in wind speed [37].

For point to point and fixed communication links, the exclusion zones have been defined for each individual interference mechanism. Most of these zones are based on recommendations presented by DF Bacon in a study conducted on behalf of the independent regulator and competition authority for the UK communications industries OFCOM in October 2002 [102]. The exclusion zone for the near field effects is the smallest (as the

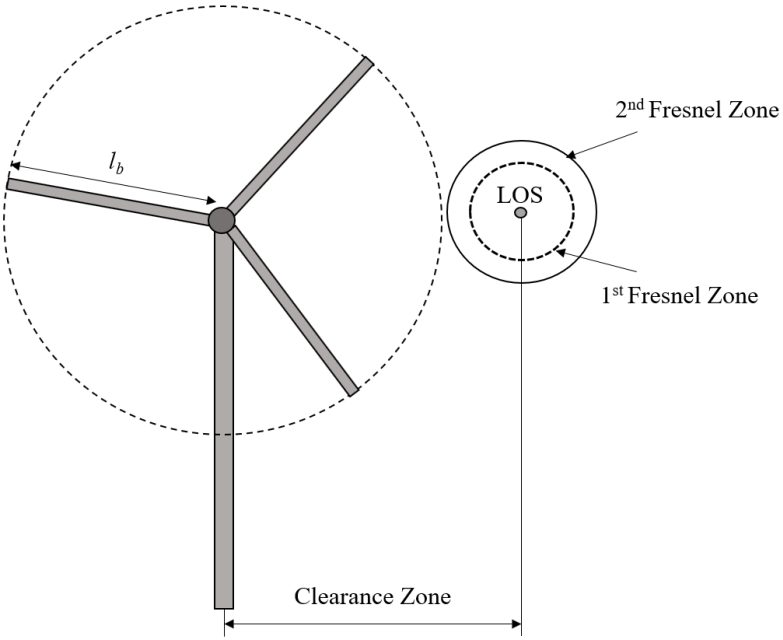

Figure 1-3: Diffraction clearance equal to 2nd Fresnel zone for fixed radio links [132]

near field zones of the transmitting and receiving antennas are considerably small) and can be ignored in most practical WT scenarios. The exclusion zone for reflection effects is determined for a recommended value of the carrier to interference ratio (C/I) that must be maintained for a good quality of the service. To calculate this exclusion zone, the interference caused by a wind turbine is assessed by means of the bistatic radar equation (eqn. 1.4), with the wind turbine characterized in terms of its maximum RCS. For diffraction effects, the study proposes a clearance volume around the radio path equal to the second Fresnel zone. Such a scenario is represented in Fig. 1-3. To illustrate, Bacon calculated the clearance zones for a typical practical scenario at a frequency of 7 GHz with a desired minimum C/I ratio of 50 dB. The maximum antenna gain considered is 32 dBi over a link length of 20 km. The RCS of the WT is taken as 30 m^2.

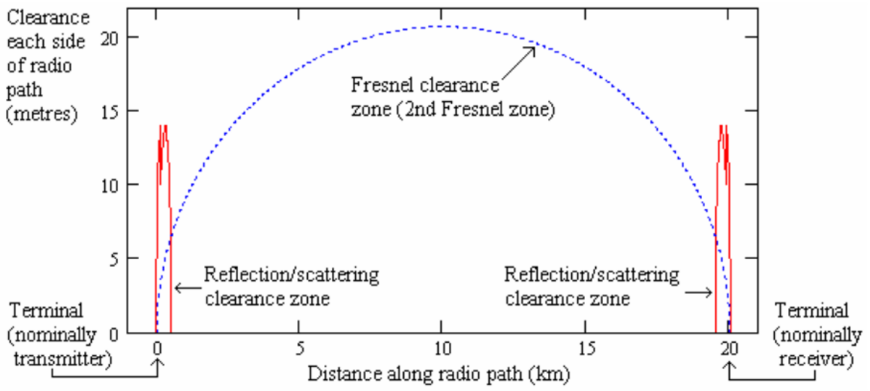

Figure 1-4: Exclusion zones by Bacon [102]

Figure 1-4 presents the clearance zones for reflection and diffraction effects as calculated by Bacon [102]. The near field effects have the smallest of the three exclusion zones and it is not even practicable to present them with good visibility on the same plot using the scale being used. The reflection/scattering clearance distance is significant only close to the transmitter and receiver and collapses to zero within around a kilometer of each terminal. The exclusion zone for diffraction is the largest of the three and is based on the 2nd Fresnel zone for the link. It is important to note that it dominates the overall clearance requirement over most of the path length.

Deriving from Bacon's method, a general setting of the exclusion zones can be drawn based on similar lines as shown in Fig. 1-5. The exclusion zone for reflection is dominant only in close vicinity to either terminal whereas the clearance volume for diffraction must be maintained over the entire link length. Thus, in terms of overall geographical area along the link, it can be said that the largest exclusion zone is for diffraction effects.

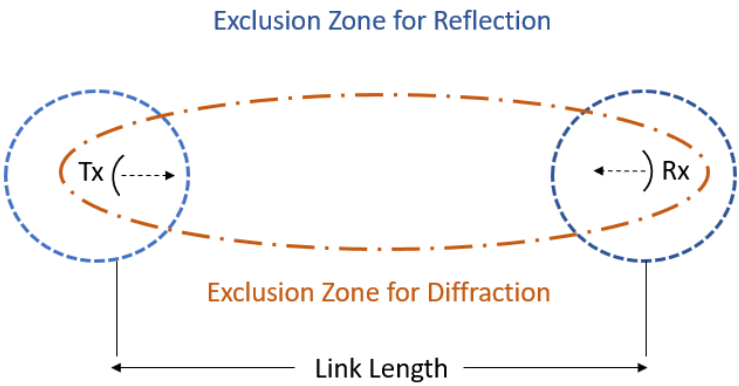

Figure 1-5: Exclusion zones for Reflection and Diffraction effects

1.4 Motivation

The performance of radar and radio communication systems can be significantly deteriorated owing to the interference caused by scattering, diffraction and near-filed effects of a nearby WT. Moreover, the rotating blades of the electrically large WT introduce a time variant deviation of the Doppler return, which can cause serious radar clutter problems. Most of the efforts to characterize the signal degradation caused by a WT have focused on the backscatter region, even though the WT diffraction effects (forward scatter) cause the largest size of exclusion zones in terms of overall geographical area around an operational radio communication link. The diffraction and shadowing effects – though well known – have only been handled in terms of measurements and time-consuming numerical simulations, without developing an in-depth understanding of the mechanism behind the seemingly well-organized diffraction patterns containing alternating areas of obstacle loss (shadowing) and gain. The motivation in this thesis is to conduct an in-depth analysis of the WT diffraction effects to develop a comprehensive insight into forward scattering of radar and radio communication signals which lies beyond the investigation of case by case studies. The first step in this regard is to have a modeling technique which effectively approximates the WT diffraction effects for complex scenarios while requiring easily affordable memory resources and low execution

times. Based on the in-depth understanding, the critical conditions of WT forward scatter will be identifying and the guidelines to avoid the scenarios of strong impact on communication links and radar systems will be outlined.

1.5 Structure of the Dissertation

The dissertation consists of seven chapters. After a brief overview of the impact of WTI on radio links and radar systems, along with the motivation behind this thesis is presented in chapter one, some fundamental concepts of space wave propagation have been outlined in chapter two. Chapter three focuses on the modeling of WT diffraction effects. An overview of various CEM techniques and their implementation in commercial 3D field simulators is briefly discussed. A simple 1D model applicable to limited propagation scenarios is introduced. An improved approach based on 2D Fresnel-Kirchhoff diffraction formula is then presented. This technique not only allows more freedom regarding the geometrical arrangement of the link LOS path and the rotor of the WT, but also includes the impact of a ground plane. Chapter four presents a qualitative analysis of WT forward scatter. The 2D Fresnel-Kirchhoff diffraction model is used to examine the amplitude and phase modulation due to diffraction by a WT. The patterns of time variant amplitude distortion due to diffraction by WT rotor are explained in terms of obstructed Fresnel zones. A similar approach is then applied to study the impact of the static tower as well as that of an illuminated ground plane. Chapter five discusses the impact of WT forward scatter on operational radar and radio communication links. First, the impact of the diffraction induced amplitude and phase modulation caused by the WT forward scatter on the performance of a fixed radio link using a higher order modulation system is considered. The focus is then shifted towards radar systems by studying the impact of an offshore WT on the error in measurement of radial speed by an S band marine radar of a large cargo vessel. The discussion presented verifies the concepts developed in chapter four and identifies the crucial aspects along with vital figures of merit for WT diffraction effects. Chapter six explores how various important parameters influence the forward scatter of a WT and discusses the critical conditions in terms of diffraction loss, phase

modulation and frequency deviation. Guidelines to avoid the scenarios of strong impact of the WT forward scatter on communication links and radar systems are also presented. The seventh chapter concludes the dissertation with a summary of the work presented along with important conclusions drawn.

2 Space Wave Propagation

Before delving into the various aspects of WTI, some fundamental concepts of wave propagation along with mechanisms that are noteworthy for interference studies are introduced in the following sections.

At frequencies above VHF, normally used for most radar and radio communication applications, space waves have traditionally been considered the dominant mode of wave propagation [12], [13]. These waves travel from the transmitter to the receiver either directly in a straight line or after reflection from earth's surface. Developing a comprehensive understanding of radio wave propagation in the presence of obstacles requires a rigorous approach involving Maxwell's equations and solution of the Helmholtz wave equation. A simpler way to gain a practical insight is by understanding how power is transferred outwards from a source towards a receiver. Such an approach is helpful in understanding the fundamental physical aspects of wave propagation, laying the foundation for more complicated cases encountered in interference studies. The simplest such case is the propagation of signals in free space, an environment devoid of obstacles like rough terrain, mountains, buildings, ground or other atmospheric effects. Consider a receiving antenna with gain G_r located at distance d (beyond the far field distance) from a transmitting antenna with gain G_t. If the transmitter power is P_t, then the power at the receiver P_r can be described as

$$P_r = \frac{P_t G_t}{4\pi d^2} \frac{G_r \lambda^2}{4\pi} \tag{2.1}$$

The first term in eqn.(2.1) is the power density at distance d from the trans-

mitter defined by the inverse square law, while the second term describes the effective aperture of the receiver in terms of its gain and operating wavelength λ. The product of the two terms represents the power absorbed by the receiver and is popularly known as the Friis transmission equation [14]. It is convenient to represent eqn. (2.1) in decibels as shown below

$$P_{r(\text{dBW})} = P_{t(\text{dBW})} + G_{t(\text{dBi})} + G_{r(\text{dBi})} + 20 \log \frac{\lambda}{4\pi d} \tag{2.2}$$

The last term in eqn. (2.2) is the negative of free space path loss, expressed in decibels. It symbolizes the loss of signal strength in reaching the receiver in free space [14]. It is interesting to note that there is only one loss term in eqn. (2.2). To account for more complex propagation scenarios compared to the free space model considered in this section, all expected losses can be lumped together and added, as propagation factor F in the last term of eqn. (2.2) to include effects of reflection, diffraction, absorption and fading.

Wave propagation in a real environment must deal with signal distortion and interference effects caused not only by wind turbines, but also by obstacles like buildings, mountains and ground plane. The range of space wave propagation is limited by the curvature of the earth and height of the antennas above the earth's surface. However, for distances less than about 10 km, the effect of the earth's curvature is often neglected, and a flat surface approximation is assumed [16]. Since most of the cases discussed in this work are concerned with distances less than the above-mentioned limit, a flat earth surface is assumed.

2.1 Reflection and Scattering

Scattered and reflected fields are quite similar in nature, mainly differing in the characteristics of the surface from which they originate. On striking the surface of an obstacle, the incident waves induce conduction or polarization currents, depending upon the material properties of the object. These currents act as secondary sources, producing fields which propagate

outwards at angles depending on the surface smoothness of the obstacle surface. Specular reflections are produced when the transmitted signal is bounced off a smooth surface much larger than the wavelength of the signal. The signal is reflected at an angle equal to the angle of incidence, in accordance with the optical law of reflection. The strength of the reflected field is determined by the reflection coefficient R of the reflecting surface and depends upon the conductivity and permittivity of the surface material along with the angle of incidence, frequency and the polarization of the incident wave [14, 16].

As the roughness of the surface increases, a gradual transition from coherent reflection to more random scattering is noticeable. Unlike reflections, scattered waves travel in numerous directions depending on the roughness of the object. Signal strength variations with changing angle of incidence caused by scattering from rough surfaces are not as noticeable as they are in case of reflections from a smooth surface. Due to the reflection and scattering of radio signals from an illuminated ground plane or a complex obstacle like a WT, propagation paths other than the direct path between the transmitter and receiver are possible. The difference in path lengths between reflected and direct signals leads to a phase difference causing interference between the two signals at the receiver [17]. The characterization of scattered fields is vital for radar applications, since radar operation is entirely dependent on fields scattered from an object for its detection and classification. For navigation, mobile and point to point radio communication links, it is also important to determine the impact of fields scattered from obstacles of different nature for link planning, system performance evaluation and interference studies. Ground plane reflections can have a major impact on the performance of radar and radio communication services. An important factor in this regard is the half power beamwidth (HPBW) of the antenna [16, 17]. Highly mounted antennas with very narrow beamwidths in elevation can end up avoiding the ground plane reflections, but that is not the case with a broader beamwidth profile. Most radio communication links use antennas with beamwidths that are broad enough for significant ground plane reflections. Broader vertical beamwidths (ranging from 11° to 30°) are also used in certain radar applications like marine radars as well as primary and secondary surveillance radars. In such application, ground plane reflections can have a major impact and cannot be ignored. The Two-Ray Ground Reflection

Model is popularly used to characterize the signal at the receiver in the presence of a multipath component formed predominantly by a single ground reflected wave [13]. For transmitter and receiver antenna heights h_1 and h_2 respectively, the propagation factor F determined for horizontal and vertical polarizations [129] can be used to modify eqn.(2.2) to account for the ground reflections as given below

$$P_{r(\text{dBW})} = P_{t(\text{dBW})} + G_{t(\text{dBi})} + G_{r(\text{dBi})} + 20\log\frac{\lambda}{4\pi d} + \begin{cases} 20\log(2|\cos\frac{2\pi h_1 h_2}{\lambda d}|) & \text{Vert. Pol.} \\ 20\log(2|\sin\frac{2\pi h_1 h_2}{\lambda d}|) & \text{Hor. Pol.} \end{cases} \tag{2.3}$$

The above equation is valid for a smooth perfectly conducting ground plane and can be modified for the case when the ground plane is not perfectly conducting by using the reflection coefficient of the plane. From eqn. (2.3), it can be deduced that in the presence of an illuminated ground plane the field strength at a given distance from the transmitter has maxima and minima determined by variations in wavelength and the heights of the transmitting and receiving antennas along with the distance between them. The maximum received field strength is twice that of the direct ray when there is constructive interference between the reflected and the direct ray [14]. Similarly, minima can be expected when there is a case of destructive interference, which in its worst form can cause a complete cancellation of signal at certain distance along the link. Figure 2-1 shows a typical space wave path loss curve based on eqn. (2.3) (neglecting any gain reduction of reflected path) for a link with parameters h_1 = h_2= 10 m, λ, = 0.23 m, G_r=G_t = 20 dBi.

In worst case scenarios, the nulls of the curve tend to be deep and show an almost complete cancellation of the signal. A real ground with lossy characteristics will not necessarily behave that way. Consequently, the interference between the direct and reflected rays may not lead to complete reinforcement or cancellation [13], which makes the prediction of the interference more complicated. For WTI studies, it is important to consider the

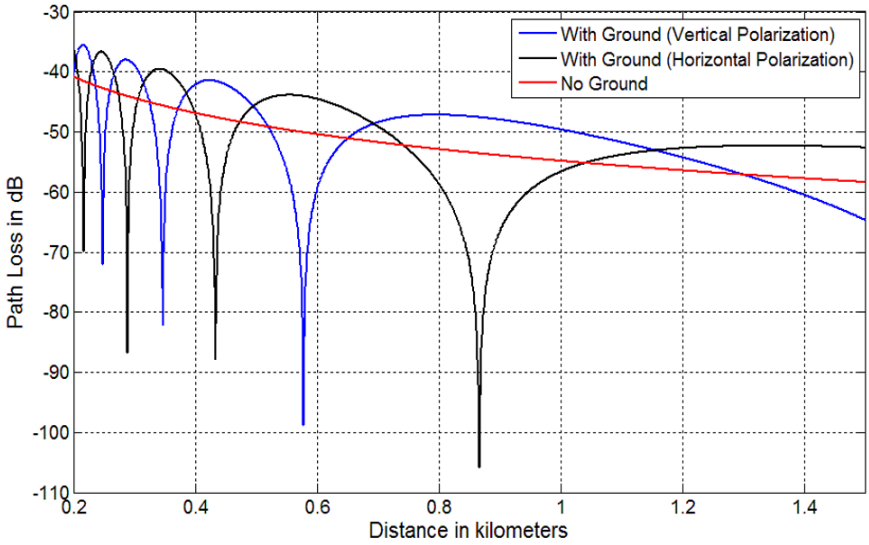

Figure 2-1: Path loss curve for space wave propagation over perfectly conducting ground, based on $h_1 = h_2 = 10$m, $\lambda = 0.23$m, G_r=G_t = 20dBi

ground plane reflections especially for applications using wider antenna beams. Link setup parameters like height and orientation of antennas along with distances between the transmitter and receiver dictate the interference pattern of the direct and ground reflected signals and the subsequent positions of the field maxima and minima along the length of the radio link.

In addition to reflections from the ground plane, another important aspect is the reflection of signals caused by the presence of obstructing objects in the path of the propagating wave. Such reflection and scattering effects are generally quantified through the concept of Radar Cross Section (RCS) [16]. RCS is the measure of an object's ability to reflect or scatter incident radio waves. Assuming plane wave illumination, it represents the scattering object in terms of an effective area, the power collected by which would, if re-radiated isotopically, give rise to the observed scattered power [18].

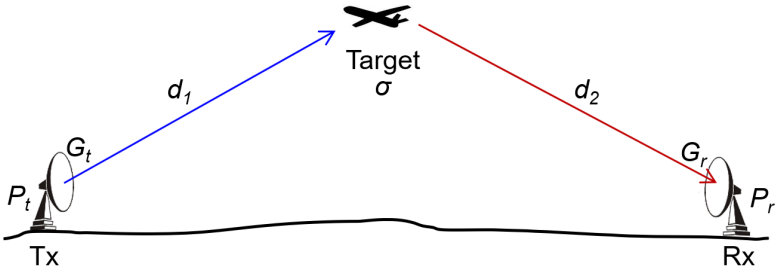

Figure 2-2: Link geometry for bistatic radar.

To account for reflections from a scattering object, the power at the receiver P_r, can be determined using the bistatic radar equation [16]

$$P_r = \frac{P_t G_t G_r \lambda^2 \sigma}{4\pi^3 d_1^2 d_2^2} \tag{2.4}$$

A bistatic radar setting is shown in Fig.2-2, where G_r and G_t are the receiver and transmitter antenna gain respectively in the direction of the scattering object, $d_1$and d_2 are the distances from the object to the transmitter and object respectively and σ is the RCS of the scattering object.

The basic definition of RCS implies illumination of the target by a plane wave and the measurement of the reflected waves under far field conditions [18]. The traditional expression for far field distance R_{ffc} is given below

$$R_{\text{ffc}} = \frac{2D^2}{\lambda}. \tag{2.5}$$

In eqn. (2.5), D is the largest dimension of the antenna or the object for which the far field distance is being calculated. For an extremely large obstructing object like a WT, the value of D (and the corresponding value of R_{ffc}) is extremely large, leading to the far field conditions to not be fulfilled in most practical situations. This leads to the observed RCS levels (and subsequent scattered fields) to be significantly different than the expected

values [19]. Moreover, the ground reflections and multipath effects produce considerably high field variations over the surface of a large object and can produce huge differences in predicted and observed RCS levels.

2.2 Diffraction

Diffraction is the modification of a radio wave when a part of an advancing wave front gets obstructed by an object [15]. Changes in signal strength caused by diffraction can have a strong impact on the performance of radar and radio communication systems [17]. The impact of diffraction on the propagation of waves through an aperture or around an object has widely been estimated by using the Huygens-Fresnel principle, according to which, every point on a progressing wave front can be considered an isotropic source of secondary wavelets [20]. The wave front at a given observation point can then be regarded as the sum of the contributions from all the secondary sources. In the case of an unobstructed path, this just reduces to an overcomplicated method of predicting the received power. However, in the presence of an obstacle, it provides an efficient way of determining the received field strengths at any distance from the obstacle. Thus, if the incident field over an aperture in a plane is known, the vector sum of the field components of all the secondary wavelets gives the total field at an observation point located at a certain distance from the plane containing the aperture [21]. To determine the diffraction effects in the far field region under the assumption that a plane wave is impinging on the aperture, the Fraunhofer diffraction equation is widely used [23]. This is the case where the distances between the source and aperture and between aperture and receiver are large enough so that the curvature of the incident and diffracted waves can be neglected. For other cases, where the distances between the transmitter, receiver and the obstructing object are not large enough for the plane wave approximation to be applicable, the Fresnel-Kirchhoff diffraction model may be used to determine the near field diffraction effects. Due to the extremely large electrical size of a WT, the transmitter and/or receiver of radio links are often located within its near field, making The Fresnel-Kirchhoff diffraction model to be more appropriate for WTI studies.

2.2.1 Fresnel-Kirchhoff Diffraction Model

In the theory originally proposed by Huygens [21], it was assumed that the secondary wavelets travelled isotropically. Additional arbitrary assumptions were included by Fresnel, who suggested that the secondary wavelets travelled only in the forward direction and there was no backward radiation. Furthermore, Fresnel introduced an obliquity factor which estimates the amplitudes of secondary waves depending on the direction of propagation. Fresnel's assumptions were mainly based on experimental results and were not backed by a comprehensive theoretical explanation. Kirchhoff placed Fresnel's concept on a firm mathematical basis through a quantitative analysis. The ad hoc assumptions by Fresnel emerge in a more natural manner from the mathematical derivation presented by Kirchhoff. The result is the Fresnel-Kirchhoff diffraction model, which uses an integral equation to directly calculate the diffraction effects from the input field [20].

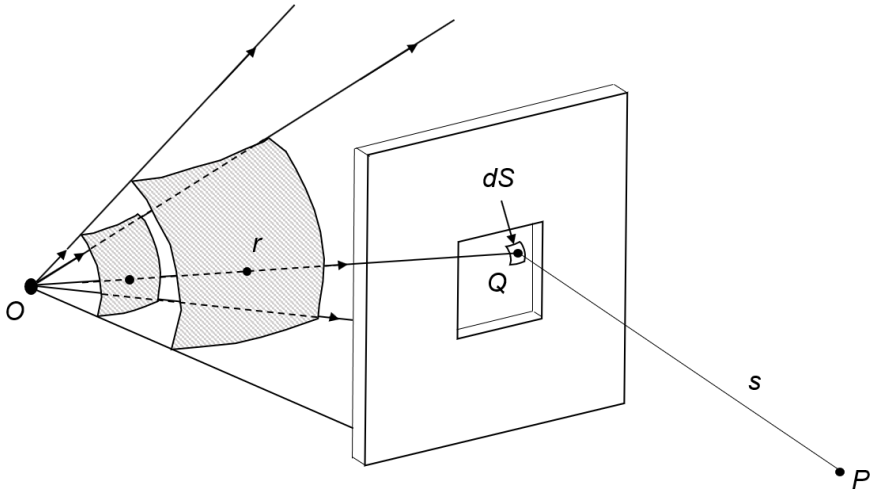

Figure 2-3: Parameters for typical Fresnel-Kirchhoff diffraction [20]

Figure 2-3 shows a typical setting with a point source O located at a distance r from a point Q on the wavefront at the aperture. The field at the receiver is observed at a point P, located at a distance of s from point Q. Since

the distances r and s are not significantly larger than the aperture size, Fresnel diffraction effects are observed at P and thus the approaching waves cannot be assumed to be plane in nature. To account for the points of the spherical wave front, the variation of r and s for different points of the aperture as well as field observation points must be considered. Moreover, the direction dependence of the amplitude of the secondary wavelets at the aperture must be taken into account. Each wavelet is assumed to be emanating from an infinitesimal region on the wavefront of elemental area dS on the wavefront [20]. Omitting the time periodic facor $e^{j\omega t}$, the electric field E_Q at point Q at the aperture can be given by

$$E_Q = \frac{E_O}{r} e^{-jkr}. \tag{2.6}$$

Where E_O is the amplitude at unit distance infront of the source O (normalized at unit distance; expressed in Volts). The field contribution E_P at point P due to the field at dS can thus be represented by

$$dE_P = \alpha_c \frac{E_O e^{-jkr}}{r} \frac{e^{-jks}}{s} dS. \tag{2.7}$$

Where α_c is a proportionality constant with dimensions of inverse length, which will be derived later.
The resultant amplitude of the electric field at P can be determined by the superposition of all the secondary wavelets at the aperture. Taking the surface integral of eqn. (2.7) for the entire aperture, E_p can be characterized as

$$E_P = \alpha_c E_O \iint\limits_{Aperture} \frac{e^{-jk(r+s)}}{rs} dS. \tag{2.8}$$

Eqn. (2.8) is the basis for the Fresnel-Kirchoff diffraction formula. Fresnel refined the above integral formula by including the obliquity factor $F(\theta)$, which attenuates the diffracted waves according to their direction of propagation. The modified formula is given below

$$E_P = \alpha_c E_O \iint\limits_{Aperture} F(\theta) \frac{e^{-jk(r+s)}}{rs} dS. \tag{2.9}$$

Where θ is the angle between the LOS axis and the diffracted ray such that θ=0° represents propagation in the forward direction along the LOS path and θ=180° represents backward propagation towards the source (Fig. 2-4(b)). Fresnel used experimental results to make assumptions about the value of the obliquity factor, and did not provide a solid theoretical backing for his claims. Kirchhoff presented a more rigorous mathematical basis for the diffraction integral, which not only defines the proportionality constant α_c in eqn. (2.9), but also provides an expression for $F(\theta)$. Kirchoff's derivation is based on the Kirchhoff-Helmholtz integral [21], which presentes the solution to the Helmholtz wave equation at an arbitrary point enlosed within a closed boundary S, in terms of the solution to the homogenious wave equation and its first-order derivatives at all points on S (see [21], [130]). According to the Kirchhoff-Helmholtz integral, if a function along with its normal derivates is known on a closed boundary, then it can be determined for any arbitrary point enclosed inside S. Figure 2-4 shows the geometrical arrangement for the mathematical derivation of Kirchhoff's diffraction integral. A point source O located at a distance r from a point Q on the wavefront at the aperture A_p. The field at a point P located at a distance s from the aperture will be the resultant sum of all the fields originating from the bounded surface enclosing P. According to the Kirchhoff-Helmholtz integral theorem the field E_P at point P can be given as

$$E_P = \frac{1}{4\pi}\left[\int\int\left(E_v \frac{\partial}{\partial n_r}\left(\frac{e^{-jks}}{s}\right) - \frac{e^{-jks}}{s}\frac{\partial E_v}{\partial n_r}\right) dS\right]. \tag{2.10}$$

Where E_v is the field inside surface S and n_r is the inward normal as shown in Fig. 2-4. Considering the closed surface formed by the intersection of a sphere of radius R_d with the plane containing the aperture A_p (Fig. 2-4(a)), eqn.(2.10) can be written as

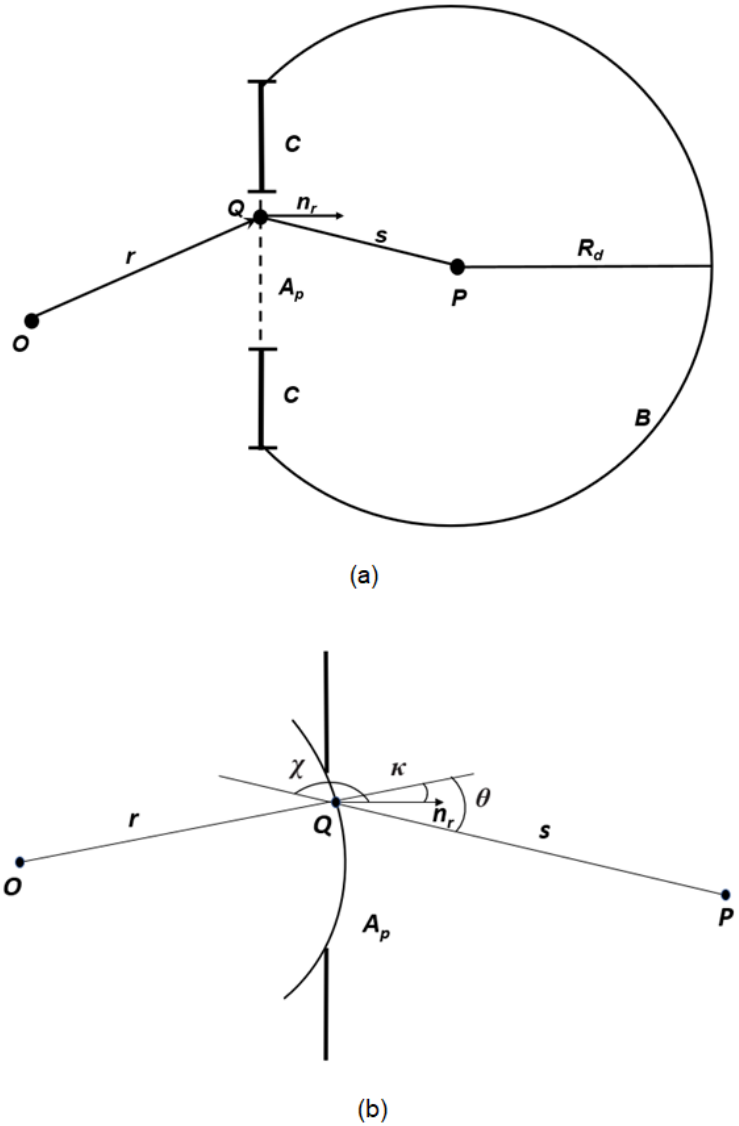

Figure 2-4: Kirchhhoff's diffraction formula: (a) geometrical arrangement for the derivation (b) detailed view of the aperture A_p [21], [130]

$$E_P = \frac{1}{4\pi}\left[\int\limits_{A_p} + \int\limits_{B} + \int\limits_{C}\left(E_v \frac{\partial}{\partial n_r}\left(\frac{e^{-jks}}{s}\right) - \frac{e^{-jks}}{s}\frac{\partial E_v}{\partial n_r}\right)dS\right]. \quad (2.11)$$

Where B is the part of the enclosing surface with boundary of radius R_d and C is the closed part of the plane containing the Aperture A_p. According to the boundary conditions, the field strength of E_v and its derivative at aperture A_p is the same as the field strength when there is no aperture. This is approximately equal to the field (E_Q) at point Q, given by eqn. (2.6). The field strength on the opaque part of the plane containing the aperture (surface C) is negligible. Moreover, for large values of R_d, the field strength on B can also be assumed to be negligibley small. These boundary conditions can be summarized as shown below:

$$E_v = \begin{cases} E_Q; & \text{For } A_p \\ 0; & \text{For } B \text{ and } C \end{cases} \quad (2.12)$$

Thus eqn. (2.11) can be simplified by only taking the integral for the aperture A

$$E_P = \frac{1}{4\pi}\left[\iint\limits_{Aperture}\left(E_Q \frac{\partial}{\partial n_r}\left(\frac{e^{-jks}}{s}\right) - \frac{e^{-jks}}{s}\frac{\partial E_Q}{\partial n_r}\right)dS\right]. \quad (2.13)$$

Using eqn. (2.6) in eqn. (2.13)

$$E_P = \frac{E_O}{4\pi}\left[\iint\limits_{Aperture}\left(\frac{e^{-jkr}}{r}\frac{\partial}{\partial n_r}\left(\frac{e^{-jks}}{s}\right) - \frac{e^{-jks}}{s}\frac{\partial}{\partial n_r}\left(\frac{e^{-jkr}}{r}\right)\right)dS\right]. \quad (2.14)$$

Using the angles shown Fig. 2-4(b), eqn. (2.14) can be written as

$$E_P = \frac{E_O}{4\pi}\left[\iint_{Aperture}\left(\frac{e^{-jkr}}{r}\frac{e^{-jks}}{s}(-jk-\frac{1}{s})\cos\chi - \frac{e^{-jks}}{s}\frac{e^{-jkr}}{r}(-jk-\frac{1}{r})\cos\kappa\right)dS\right]. \tag{2.15}$$

Since r and s are much larger than λ, the summands $\frac{1}{r}$ and $\frac{1}{s}$ are negligibly small as compared to the term jk. Thus eqn. (2.15) reduces to

$$E_P = \frac{jE_Ok}{4\pi}\left[\iint_{Aperture}\frac{e^{-jk(r+s)}}{rs}(\cos\chi - \cos\kappa)dS\right]. \tag{2.16}$$

For values of r much larger than the width of the aperture, the angle κ tends to zero while $\chi = \pi - \theta$. Using these values in eqn. (2.16) ,

$$\begin{aligned} E_P &= \frac{jE_Ok}{4\pi}\iint_{Aperture}\frac{e^{-jk(r+s)}}{rs}(1+\cos\theta)dS \\ &= \frac{jE_O}{\lambda}\iint_{Aperture}\frac{e^{-jk(r+s)}}{rs}\frac{(1+\cos\theta)}{2}dS. \end{aligned} \tag{2.17}$$

Comparing eqn. (2.17) with eqn. (2.9), some important deductions can be made. It can be seen that the constant of proportionality α_c with units of inverse length introduced by Fresnel is found by Kirchhoff to be equal to $\frac{j}{\lambda}$. Similarly, the obliquity factor $F(\theta)$ can be defined as

$$F(\theta) = \frac{(1+\cos\theta)}{2}. \tag{2.18}$$

The obliquity factor modifies Huygens secondary wavelets such that they cease to be isotropic with decreasing amplitude as the value of θ increases. In the backward direction (θ=π), the factor becomes zero and thus the amplitude of the wavelets in the backward direction is zero. Another important observation in eqn.(2.17) is the factor j, which introduces a phase

shift of $\pi/2$ for the diffracted waves relative to the primary incident wave. Both these factors play an important role in understanding the diffraction effects from an aperture and are presented in more detail in later discussions.
The result expressed by eqn.(2.17) still involves approximations, requiring that the source and screen distances remain large relative to the aperture dimensions and that the aperture dimensions themselves remain large relative to the wavelength of the optical disturbance. The integration specified by eqn. (1.12) is over a closed surface including the aperture but is assumed to make a contribution only over the aperture itself. Moreover, no scattering from aperture edges is considered [20].

2.2.2 Half Plane Diffraction

A theoretical mathematical model widely used for understanding the diffraction mechanism along with conservatively estimating its impact on signal propagation considers diffraction from a half plane obstruction, with a knife-like edge protruding into the line of sight path [22]. Figure 2-5 shows the scenario considered. A transmitter antenna Tx of height h_t is placed on one side of the knife edge obstruction K at a distance d_1, with a receiver antenna Rx of height h_r at a distance d_2 on the other end. The height of the obstruction protruding above the LOS path between the transmitter and receiver is h_{ke}.

According to the Huygen's principle, points above the knife edge obstruction can be considered secondary wavelet sources, responsible for producing the waves propagating toward the receiver [131]. This model aims to predict the ratio of the signal strengths with and without the obstruction, referred to as the diffraction loss or diffraction gain. The path length difference Δd between the LOS path Tx-Rx and obstructed path Tx-K-Rx can be given as

$$\Delta d = \sqrt{d_1^2 + h_{\text{ke}}^2} + \sqrt{d_2^2 + h_{\text{ke}}^2} - (d_1 + d_2) \tag{2.19}$$

For large values of d_1 and d_2 compared to the obstruction height (d_1,d_2>>h_{ke}),

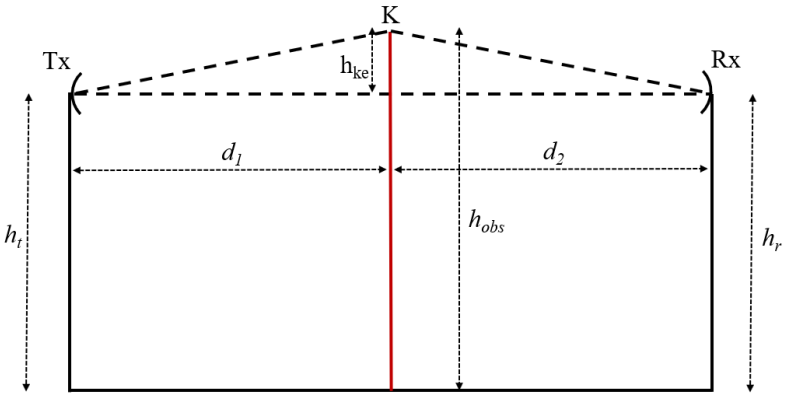

Figure 2-5: Knife edge diffraction model [131]

$$\Delta d \approx d_1\left(1+\frac{h_{\text{ke}}^2}{2d_1^2}\right)+d_2\left(1+\frac{h_{\text{ke}}^2}{2d_2^2}\right)-d_1-d_2$$

Thus,

$$\begin{aligned}\Delta d &= \frac{h_{\text{ke}}^2}{2}\left(\frac{1}{d_1}+\frac{1}{d_2}\right)\\ &= \frac{h_{\text{ke}}^2}{2}\left(\frac{d_1+d_2}{d_1 d_2}\right).\end{aligned} \tag{2.20}$$

The corresponding phase difference $\Delta\psi_d$ can be determined by multiplying the path difference by wave number k

$$\Delta\psi_d = \frac{\pi}{2}\left(h_{\text{ke}}^2\frac{2}{\lambda}\frac{d_1+d_2}{d_1 d_2}\right). \tag{2.21}$$

The term in the bracket can be referred to as the square of the Fresnel-

Kirchoff parameter v such that

$$v = h_{\text{ke}} \sqrt{\frac{2(d_1 + d_2)}{\lambda d_1 d_2}}. \tag{2.22}$$

From eqn. (2.22), it can be seen that v is essentially the size of the obstruction multiplied by a scalar value defined by the frequency of operation. Thus, the eqn. (2.21) reduces to

$$\Delta\psi_d = \frac{\pi}{2} v^2. \tag{2.23}$$

Eqn. (2.23) shows the phase difference for the single diffracted ray considered in this example. The corresponding electric field at the receiver E_R, relative to the field due to the LOS path E_S can be calculated by

$$E_R = E_S e^{-j\frac{\pi}{2}v^2}. \tag{2.24}$$

To calculate the overall electric field at the receiver, the impact of all the Huygen's wavelets above the obstruction must be considered. Thus, an integration of eqn. (2.24) from v to ∞ is performed to calculate the value of E_R

$$E_R = E_S \frac{(1+j)}{2} \int_v^\infty e^{-j\frac{\pi}{2}X^2} dX \tag{2.25}$$

In eqn. (2.25), the factor $(1 + j)/2$ represents that in the absence of the obstruction (v= $-\infty$), the field at the receiver is equal to the field due to only the LOS path (E_R=E_S). The diffraction loss is thus given by the complex Fresnel integral $F(v)$

$$\frac{E_R}{E_S} = F(v) = \frac{(1+j)}{2} \int_v^\infty e^{-j\frac{\pi}{2}X^2} dX. \tag{2.26}$$

This can be expanded as

$$F(v) = \frac{(1+j)}{2}\left[\int_{v}^{\infty} \cos\left(\frac{\pi}{2}X^2\right)dX - j\int_{v}^{\infty} \sin\left(\frac{\pi}{2}X^2\right)dX\right]. \tag{2.27}$$

where

$$\begin{aligned}\int_{v}^{\infty} \cos(\frac{\pi}{2}X^2)dX &= \int_{0}^{\infty} \cos\left(\frac{\pi}{2}X^2\right)dX - \int_{0}^{v} \cos\left(\frac{\pi}{2}X^2\right)dX \\ &= \frac{1}{2} - C(v).\end{aligned} \tag{2.28}$$

$$\begin{aligned}\int_{v}^{\infty} \sin(\frac{\pi}{2}X^2)dX &= \int_{0}^{\infty} \sin\left(\frac{\pi}{2}X^2\right)dX - \int_{0}^{v} \sin\left(\frac{\pi}{2}X^2\right)dX \\ &= \frac{1}{2} - S(v).\end{aligned} \tag{2.29}$$

In the above equations, $C(v)$ and $S(v)$ are Fresnel's cosine and sine integrals respectively [20] and are given below

$$\begin{aligned}C(v) &= \int_{0}^{v} \cos\left(\frac{\pi}{2}X^2\right)dX. \\ S(v) &= \int_{0}^{v} \sin\left(\frac{\pi}{2}X^2\right)dX.\end{aligned} \tag{2.30}$$

Eqn.(2.27) can thus be written as

$$F(v) = \frac{(1+j)}{2}\left(\left[\frac{1}{2} - C(v)\right] - j\left[\frac{1}{2} - S(v)\right]\right). \tag{2.31}$$

Eqn. (2.31) presents a simplified way to characterize the diffraction loss caused by an obstruction of the LOS path by an infinite half plane [131].

2.2.3 Fresnel Zones

Let us consider a single Huygens' wavelet elevated to a certain height above the LOS path. If this height is selected such that the path difference Δd between the direct and diffracted waves is equal to $\lambda/2$, then the corresponding phase shift $\Delta\psi_d$ is equal to π radians relative to the LOS path. This condition holds true for a locus of points forming an ellipsoid. If the height is further increased such that Δd=λ, a locus of all such points produces a second ellipsoid, where $\Delta\psi_d$ is now equal to 2π radians. This process can be repeated, obtaining zones with alternating in-phase and out of phase fields relative to the LOS path for every $\lambda/2$ increase in Δd. These zones are known as the Fresnel zones and can be defined in terms of the path difference in multiples of $\lambda/2$. The set of all points at which a propagating wave experiences an excess path length of precisely $n\lambda/2$ to be called the outer boundary of the n^{th} Fresnel zone. The radius of the n^{th} Fresnel zone R_n can be calculated by setting Δd =$\lambda/2$ in eqn. (2.20), thus

$$\frac{n\lambda}{2} = \frac{h_{\text{ke}}^2}{2}\left(\frac{d_1 + d_2}{d_1 d_2}\right) \tag{2.32}$$

In this case $R_n = h_{\text{ke}}$, Thus

$$R_n = \sqrt{\frac{n\lambda d_1 d_2}{d_1 + d_2}}. \tag{2.33}$$

The above expression gives the radius of the n^{th} Fresnel zone, which depends on the wavelength λ and the distances d_1 and d_1. It is worth noting that the radius of a given Fresnel zone is maximum when d_1=d_1. The zone size decreases as the obstruction is moved closer to either the transmitter or the receiver.

The concept of Fresnel zones is a significant aspect of radar and communication link studies and design. Fresnel zone information is used for the

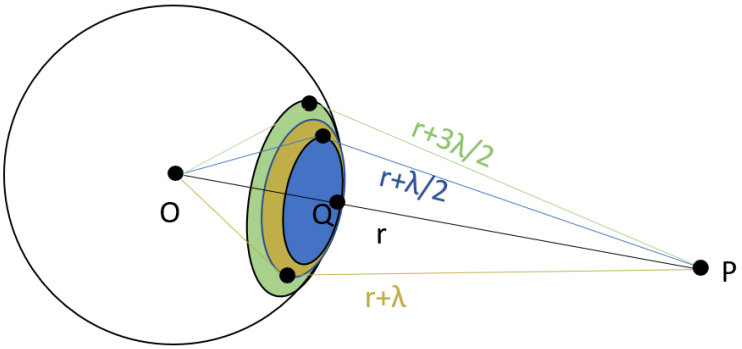

Figure 2-6: Fresnel half-period zones on a spherical wavefront emerging from an aperture [20]

determination of diffraction effects caused by obstructions that lie within the zone. In this regard, it is important to understand how each individual Fresnel zone contributes to the overall field at an observation point. Fresnel's method for understanding the contributions from different parts of the wavefront assumes a circular aperture, subdivided into zones with symmetry about the axis SOP, as shown in Fig. 2-6. A spherical wavefront is assumed to be centered at S. The zones are represented by circles on the wavefront, oriented such that each zone of area S_n is $\lambda/2$ farther from field observation point P than the zone preceding it. Consequently, every following zone has a contribution which is exactly out of phase with that of the zone before it. Furthermore, since the phase inside a Fresnel zone varies from one end to the other by 180°, every zone can be split into m subzones, with each subzone corresponding to $180°/m$ change in phase.

Figure 2-7 shows a phasor diagram for the case where each zone has been subdivided into 15 subzones (m=15). A phasor is used to represent individual contributions from each subzone. The first half-period zone (blue shaded line; Fig. 2-7) is completed after phasors for each of its constituent subzones end in a phasor opposite in direction to the first subzone phasor. The resultant of the subzones in the first Fresnel zone is denoted by amplitude $a1$ (vertical dashed line), perpendicular to the reference direction showing a phase difference of $\pi/2$ compared to the

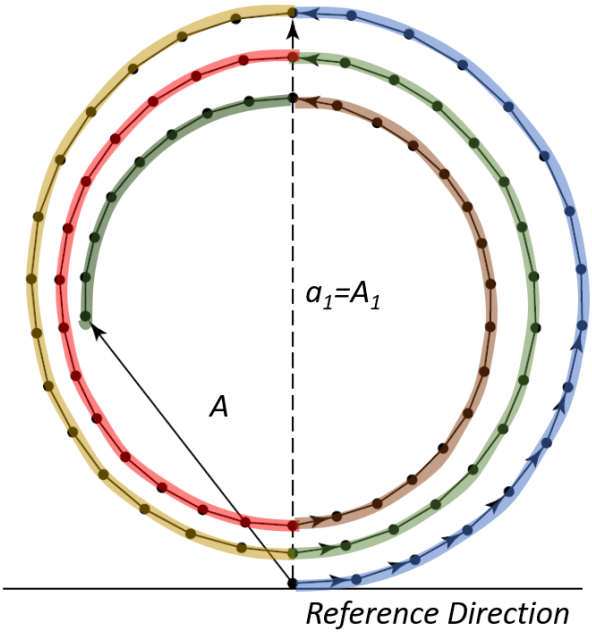

Figure 2-7: Phasor diagram for Fresnel zones [20]

first subzone phasor. For a large number of subzones, the phasor diagram becomes circular. The angle between the incident ray on a half period zone and the direction of the point of observation from the same zone is θ. The obliquity factor modifies Huygens wavelets such that have decreasing amplitude as the value of θ increases. Furthermore, due to the obliquity factor, each succeeding phasor becomes slightly shorter than the preceding one, resulting in the inwards spiraling of the circle. The amplitudes at P from n half period zones can thus be expressed as

$$\begin{aligned} A_n &= a_1 + a_2 e^{i\pi} + a_3 e^{i2\pi} + ...a_n e^{i(n-1)\pi} \\ &= a_1 - a_2 + a_3 - a_4 + a_5 ... + a_n \end{aligned} \tag{2.34}$$

For an odd number of zones (n=odd), eqn. (2.34) can be written as

$$A_n = \frac{a_1}{2} + \left(\frac{a_1}{2} - a_2 + \frac{a_3}{2}\right) + \left(\frac{a_3}{2} - a_4 + \frac{a_5}{2}\right) + ... + \left(\frac{a_{n-2}}{2} - a_{n-1} + \frac{a_n}{2}\right) + \frac{a_n}{2}. \tag{2.35}$$

In eqn.(2.35), the terms in the brackets present the sum of the amplitude of any zone with the average amplitude of its neighbouring zones. If these terms are positive, it can be concluded that A_n will have a value greater than the average of the amplitude of the first and n^{th} zone, i.e.

$$A_n > \left(\frac{a_1 + a_n}{2}\right). \tag{2.36}$$

Similarly, eqn. (2.34) can be rearranged as

$$A_n = a_1 - \frac{a_2}{2} - \left(\frac{a_2}{2} - a_3 + \frac{a_4}{2}\right) - \left(\frac{a_4}{2} - a_5 + \frac{a_6}{2}\right) - ... - \left(\frac{a_{n-3}}{2} - a_{n-2} + \frac{a_{n-1}}{2}\right) - \frac{a_{n-1}}{2} + a_n. \tag{2.37}$$

Using the same assumption that the bracket terms in eqn. (2.35) are positive, eqn. (2.35) can be used to deduce that

$$A_n < a_1 - \left(\frac{a_2 + a_{n-1}}{2}\right) + a_n \tag{2.38}$$

Since a_2 is only slightly smaller than a_1 (due to the obliquity factor), we can assume $a_1 \approx a_2$ and $a_{n-1} \approx a_n$. Thus from eqn. (2.36) and (2.38) , it follows

$$\left(\frac{a_1 + a_n}{2}\right) \leq A_n \leq \left(\frac{a_1 + a_n}{2}\right)$$

or

$$A_n = \left(\frac{a_1 + a_n}{2}\right) \tag{2.39}$$

In a similar fashion, it can be shown that for an even number of zones (n=even)

$$A_n = \left(\frac{a_1 - a_n}{2}\right) \tag{2.40}$$

If the the bracket terms in eqn. (2.35) are taken to be negative instead of the positive values used to deduce equations (2.39) and (2.40), a similar manner of arguments would lead to the same conclusions.

For further elaboration, consider Fig. 2-8 which shows a phasor diagram for the amplitude terms of eqn. (2.34) along with the corresponding composite phasors. Compared to the preceding phasor, each subsequent phasor is 180° out of phase and is shorter in length due to the obliquity factor. It can be seen (Fig. 2-8) that for a small value of n, large changes in the composite phasor A_n are observed as the contribution of each new Fresnel zone is added. For large values of n, the resultant amplitude tends to have a value larger than $a_1/2$ if n is odd and a value smaller than $a_1/2$ if n is even. This is in agreement with the equations (2.39) and (2.40).

This discussion makes an essential statement about the contributions of the individual Fresnel zones. The overall field at an observation point depends on the total number of contributing Fresnel zones. It can be said that for a small number of zones, if n is odd then the resultant amplitude is close to that of the first zone; whereas the resulatant amplitude is close to zero if n is even. For a large number of zones, the resultant amplitude has a value close to half that of the first zone $a_1/2$ [20]. Moreover, relative to the first zone, contributions from each subsequent zone alternate between a reinforcing and cancellation effect on the overall field.

2.3 Summary

In this chapter, the fundamentals of space wave propagation have been discussed. The important aspects in terms of signal reflection, scattering and diffraction effects have been highlighted. These essential concepts are vital in understanding the various aspects of WTI. In the chapters that follow, the Fresnel diffraction approach described in this chapter has been

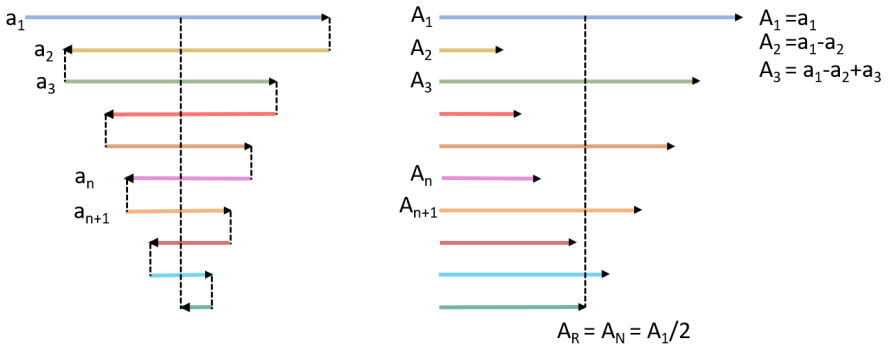

Figure 2-8: Phasor diagram for Fresnel zones (a) Individual phasors (b) Resultant phasors at each step [20]

used for the modelling of WT forward scatter effects and the analysis of WT diffracted fields by considering the Fresnel zones. In this regard, the concepts presented in this chapter go a long way in laying the foundation of the analysis presented in the rest of this dissertation.

3 WT Diffraction Modelling

The lack of a qualitative understanding of WT forward scatter in literature calls for an in-depth investigation of WT diffraction effects to comprehensively understand the central mechanisms involved. The first step in this regard is to have a modeling technique which effectively approximates the dynamic diffraction loss and associated phase modulation while requiring easily affordable memory resources and low execution times. This chapter aims to assess the capability of different simulation approaches and CEM methods for an efficient and thorough characterization of WT diffraction effects. An overview of various CEM techniques and their implementation in commercial 3D field simulators is briefly discussed. Solution techniques implemented in EM simulation software FEKO are investigated before drawing some important conclusions about the advantages and limitations of the available methods for an in-depth analysis of WTI. The suitability of Fresnel diffraction approach in efficiently characterizing WT forward scatter is then explored. As WTs are electrically large objects, the transmitter and/or receiver of radio links are often located within their respective near fields, Fresnel diffraction approach is deemed more suitable than the Fraunhofer approximation since the latter does not include near-field scenario. The discussion starts with a simple 1D diffraction model based on the knife edge diffraction technique. This approach is applicable only to relatively simpler propagation scenarios restricted to link geometries where the line of sight (LOS) path cuts right through the rotor swept area. For more complex scenarios, an improved approach based on 2D Fresnel-Kirchhoff diffraction formula is then presented. This technique not only allows more freedom regarding the geometrical arrangement of the link LOS path and the shape of the rotor of the WT, but also includes the impact of a ground plane (with finite or infinite conductivity). Projecting the WT into the plane of obstruction, rotor angle dependent amplitude ($\Delta\alpha$) and phase ($\Delta\beta$) distortion are calculated from the received field E_p comparing

the case with and without WT. It is important to note that the diffraction modeling approach presented in this chapter solely considers diffraction effects and any reflection and backscattering is ignored. The implementation of both of the presented techniques is performed in MATLAB and the results are evaluated by comparison with Uniform Theory of Diffraction (UTD) results obtained by FEKO.

3.1 CEM Techniques

For WTI studies, CEM methods presents an alternative to predict the potential interference effects without having to carry out rigorous measurements. It allows the analysis of various electromagnetic mechanisms prior to the design and installation of communication links and wind turbines, which permits potential problems to be identified well in advance. Different CEM methods have been developed for a wide range of EM problems. While each method is used to obtain essentially the same information about electromagnetic fields, every method significantly influences the efficiency and accuracy with which certain wave propagation mechanisms are analyzed. Commercial EM field solver platforms provide a variety of CEM methods. The operation of these solvers is based on the numerical solution of Maxwell equations in differential or integral form, either in the time domain or the frequency domain. EM problems are analyzed by subdividing all systems into smaller individual components or elements, whose behaviors are easier to understand. An important aspect is the selection of the most appropriate method for a given problem with each method having its individual set of advantages and shortcomings. It is important to understand these aspects to make an informed decision about the suitability of different EM software and solution methods for the analysis of WTI.

3.1.1 Full Wave Analysis Techniques

Most Commercial EM field solvers are developed around Full wave analysis techniques, which solve the complete set of Maxwell's equations

without any simplifying assumptions and consider all field components involved to derive a rigorous numerical solution [104, 105]. These techniques are classified into differential and integral methods. Integral equation methods make use of Maxwell's equations in integral equation form and reduce them to a set of simultaneous linear equations that may be solved using standard algebra [105, 108]. Differential equation methods use partial differential equations derived directly from Maxwell's curl equations or the Helmholtz wave equations with little analytical preprocessing [105]. Method of Moments (MoM) is the most popular integral equation full wave analysis method in the frequency domain. It uses integral form of Maxwell's equations along with the appropriate boundary conditions, with electric or magnetic currents being the unknown quantities [107]. Finite element method (FEM) is the most widely used frequency domain differential equation method, whereas Finite Integration Technique (FIT) and Finite Difference Time Domain (FDTD) are examples of other popular time domain solution methods [107].

One major aspect of CEM methods is the consideration of space around the object under investigation. Differential equation methods, like FEM, FDTD and FIT, use volume discretization where the entire solution domain is segmented or meshed. Integral equation techniques use surface discretization which requires only the surface of the object to be segmented, leaving the space around it unmeshed. WTI studies are concerned not only with the very large turbine structures, but also involve large scale space and distances. Thus, for WTI studies, using volume discretization would require extremely large memory resources and simulation execution times, making integral equation methods the obvious choice. However, the discretization of the geometry in differential elements is performed with sizes of approximately $\lambda/8$ or $\lambda/10$ [106]. Therefore, for WTI analysis, full wave analysis becomes limited by the availability of computational resources. A strong emphasis has been placed on developing rigorous techniques with new formulations based on multipoles and multilevel, such as the fast multipole method (FMM) and the multilevel fast multipole method (MLFMM) [106]. These developments, together with the intensive use of the parallel computation using large computer clusters, have allowed rigorous full wave techniques to be applied to solve electrically large problems. However, WTs present a special challenge owing to their extremely large sizes, since a typical WT has dimensions greater than 30 wavelengths even at frequencies at the lower end of the UHF band. Thus except for single case studies, it is impractical to compute full wave solutions even with

high memory resources.

3.1.2 High Frequency Asymptotic Methods

High frequency asymptotic methods approximate Maxwell's equations to obtain solutions whose accuracy increases with frequency. While this approach considerably simplifies the problem of electrically large structures and reduces the computational overheads, the accuracy of the obtained solutions is reduced since not all field components are accounted for. It is worthwhile to note that these methods do not have an intrinsic frequency limitation. The only restriction to their application is imposed by the condition that the size of a scatterer must be large compared to the wavelength, making these methods especially suitable for problems involving extremely large structures [105]. The most popular asymptotic techniques are Geometrical Optics (GO), Physical Optics (PO), Geometrical Theory of Diffraction (GTD) and Uniform Theory of Diffraction (UTD). Geometric Optics is a ray-based technique that uses classic optic theories like Snell's law of refraction and Fermat's Principle to model objects based on optical propagation. GO is applicable only for directly illuminated or the deep lit regions of an object and ignores diffraction effects [105, 108].

Physical optics (PO) is an intermediate method, between geometrical optics (GO) and full-wave electromagnetics. The PO method involves integrating the currents obtained from GO using the exact integral representation of the scattered fields. This approach assumes that the current on a surface is only dependent on the incident field and the geometrical parameters of each point on the surface [105]. The current is considered null in the shadowed areas of the surface, and the scattered field is obtained from the exact integral representation of that field as a function of the induced currents. This approach is relatively simple and does not require high computing resources. However, since the current at the shadowed region is set to zero, the calculated field values at wide angles and in shadow regions are not accurate. Moreover, effects like surface waves, multiple reflections and edge diffractions are not accounted for.

GTD and UTD are also ray-based techniques like GO, and model objects

based on optical propagation, reflection and refraction theory [108]. These methods aim to overcome the shortcomings of GO (and PO) in terms of dealing with the shadowed regions. GTD is an extension of geometrical optics which accounts for diffraction. Moreover, it is applicable to directly illuminated areas as well as the shadowed regions [109]. However, field calculations at the shadow boundary regions are not possible. This shortcoming is overcome by the UTD method. UTD is valid for all three (illuminated, shadowed, shadow boundary) regions, but is only applicable for flat metallic surfaces [104].

While full wave analysis techniques produce highly accurate results, they require very high computational times and memory resources due to their rigorous nature. Using high frequency asymptotic methods is the only practical way to handle extremely large electrical structures like wind turbines. However, each of these methods has a realm where it is most useful. PO and GO are better suited for problems focusing on reflection and scattering of signals whereas GTD and UTD are more suitable in applications where diffraction effects need to be analyzed.

3.1.3 3D EM Field Simulator Software

EM simulators are not merely Maxwell equation solvers, but powerful simulation and design tools with visualization capabilities. While solution method variety with affordable computational cost is the most vital factor in selecting a software package for WTI investigations, other features like structure modeling and definitions, material properties support, ground plane effects and other user-friendly aspects also need to be considered. Some popular commercial EM field simulators offer an attractive set of solutions for the electromagnetic analysis of a large structure like a WT and seem capable of assisting in WTI characterization. Remcom's XGtd is a general-purpose ray-based software tool which combines UTD with PO and method of equivalent currents (MEC) to predict important propagation mechanisms [115]. NewFASANT is an electromagnetic simulation suite developed by The Computational Electromagnetics Group of the University of Alcalá, Spain. It is a collection of different code modules, each designed for a specific application. NewFASANT supports different solu-

tions methods like MoM, PO, GO and UTD and offers separate modules for simulating different aspects of interference scenarios [116]. SuperNEC is a hybrid MOM-UTD antenna and electromagnetic simulation program, developed by Poynting Software (Pty) Ltd. It requires external control commands through MATLAB to define the geometry to be simulated as well as to view the simulation results [113]. Compared to the simulators mentioned above, the widest range of solution techniques is supported by FEKO, presented by EM Software and Systems [106, 114]. It is a MoM based software that also offers various hybrid solutions like MoM-PO, MoM-GO, MoM-UTD and MoM-FEM, along with a faster variant of MoM-PO known as large element PO (LEPO). It also supports MLFMM which enables users to perform full wave analyses with significantly lower computational costs. In addition, it offers other desirable features like support for different material types, infinite ground planes for some solution types, CAD model imports and easy to navigate environment definitions. For WTI characterization using FEKO, MoM and MLFMM have high computational costs and hence a full wave analysis cannot be considered practical. MoM-PO does not consider diffraction and multiple reflection effects, moreover the computational costs (while significantly lower than full wave techniques) are still considerably high. LEPO allows for much larger mesh sizes compared to conventional PO (1.5 λ instead of $\lambda/6$), thus significantly reducing the required memory and simulation run time. However, it is not applicable to dielectric materials and can only be used with perfect electric conductor (PEC) structures. FEKO offers GO solutions for structures with dimensions larger than 20 λ. The mesh can be very coarse; thus, no major mesh storage problems are faced. Conducting as well as dielectric materials are supported. It is good for scattering analysis with multiple reflections. Its major disadvantage is that diffraction effects are not accounted for. UTD solutions can be used for the scattering analysis of very large structures where diffraction effects are important. However, UTD has the disadvantage that in its current FEKO implementation, it is only applicable for flat conducting surfaces and does not account for dielectrics and curved surfaces. Moreover, the solution calculation becomes rather complex if ground plane effects need to be considered. It is interesting to note that each solution method seems suitable for a particular nature of analysis. While PO has the most desirable combination of accuracy and affordable computational costs for the RCS and backscatter investigation of a wind turbine, UTD seems the most suitable for the diffraction analysis but has limited material support. For scenarios involving ground reflections, UTD

solutions can only be obtained for PEC ground planes of finite dimensions and scenarios where reflections from a finite conductivity ground are to be considered, the UTD solution would be difficult to obtain.
It must be mentioned here that the information presented in this section is valid only till the time this investigation was carried out and by no means should this overview be considered as conclusive.

3.2 1D Diffraction - Knife Edge Diffraction Model

The knife edge diffraction model (section 2.2.2) is generally used to estimate the diffraction effects caused by an obstructing half-plane. A similar approach is presented in this section to calculate WT diffraction effects for a limited set of scenarios [110].

Depending on the region of interference of the signal path and WT, two cases can be considered, as shown in Fig. 3-1. In the first scenario, the signal path is assumed to be below the rotor swept area and only the stationary WT tower is causing the obstruction. This is represented by the red shaded region (zone 1) in Fig. 3-1. In this case, the 1D diffraction model can be applied along a horizontal axis perpendicular to the line-of-sight path, such that the origin of x and y coordinate is aligned with the axis of the signal path in the plane of obstruction. The electric field amplitude at a receiver located on the axis of the signal path can be determined by

$$\begin{aligned} E_p &= E_u \frac{(1+j)}{2} \int_{v_{\min}}^{v_{\max}} A(v) e^{-j\frac{\pi}{2}v^2} dv \\ &= E_u \frac{(1+j)}{2} \left\{ \Big[C(v) - jS(v) \Big]_{v_{x_2}}^{+\infty} + \Big[C(v) - jS(v) \Big]_{-\infty}^{v_{x_1}} \right\} \end{aligned} \tag{3.1}$$

where E_u is the amplitude of the electric field at the receiver when there is

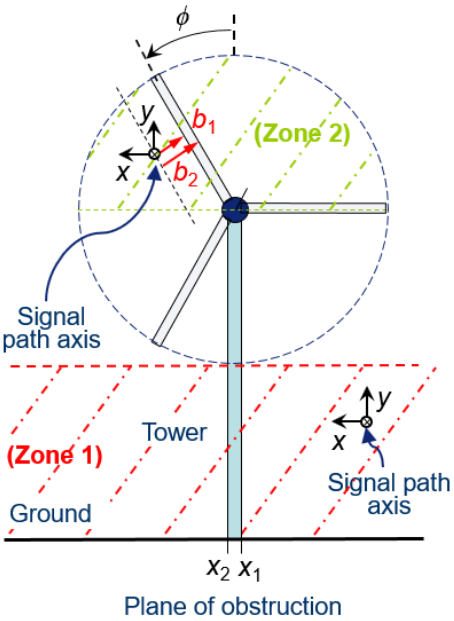

Figure 3-1: 1D Model in plane of obstruction – WT in specular direction (head-on view) [110]

no obstruction and v is a dimensionless aperture coordinate. For zone 1, it can be calculated as given below

$$v_{x_{1/2}} = x_{1/2}\sqrt{\frac{2}{\lambda}\left(\frac{1}{d_1}+\frac{1}{d_2}\right)} \tag{3.2}$$

The coordinates x_1 and x_2 represent the edges of the WT tower in the plane of obstruction, as shown in Fig.3-1. For a given value of the aperture coordinate v, the function $A(v)$ equals 1 in the absence of any obsturction and is taken to be 0 for obstruction at point v. C and S are Fresnel integrals mentioned in section 2.2.2 [20]. Wavelength of the signal is represented by λ, while d_1 and d_2 are the distances from WT to transmitter and WT to receiver respectively as defined in section 2.2.2.

In the second scenario, the signal path lies inside the upper half of rotor swept area (above nacelle) and is obstructed only by the rotating WT blades, assumed to be rectangular in shape. This time variant obstruction zone is represented by the green shaded region (zone 2) in Fig. 3-1. The 1D diffraction model is applied to a plane spanned by the signal path axis and aligned perpendicular to the edge of the nearest located blade. Only one blade of infinite length is considered here, instead of three blades of finite length of an actual WT. The amplitude of the electric field at a receiver located on the axis of the signal path for zone 2 can be determined by using equations (3.1) and (3.2), with $x_{1/2}$ replaced by $b_{1/2}$. The dimensionless aperture coordinate for zone 2 can thus be calculated by determining $b_{1/2}$ as given below:

$$b_{1/2} = -\sqrt{x_0^2 + y_0^2}\,\sin\left(\phi + \arctan\frac{x_0}{y_0}\right) \pm \frac{w_b}{2} \tag{3.3}$$

Where x_0 and y_0 are the coordinates at the rotor axis, ϕ is the rotor angle and w_b is the blade width. The + sign is applicable for b_1 and the – sign for b_2.

3.3 2D Fresnel Kirchchoff Diffraction Model

The 1D Diffraction model presents a relatively simple and straightforward method to approximate the WT diffraction effects, but only a very limited set of propagation scenario can be considered. It has some noticeable shortcomings since only a single rotor blade is considered. Moreover, signal paths outside the rotor swept area and ground plane effects are not supported.
To overcome the limitations of the 1D model, an improved 2D approach is presented in this section. This 2D Diffraction model calculates the periodic amplitude and phase modulation caused by WT forward scattering as a function of the time-variant rotor angle ϕ, by using the Fresnel-Kirchhoff diffraction approach described in section 2.2.1 [111]. The WT geometry is projected into a plane referred to as the plane of obstruction. The effect of an illuminated ground plane (reflected path between transmitter and WT

as well as between WT and receiver/target) is accounted for by considering an image transmitter and an image receiver.

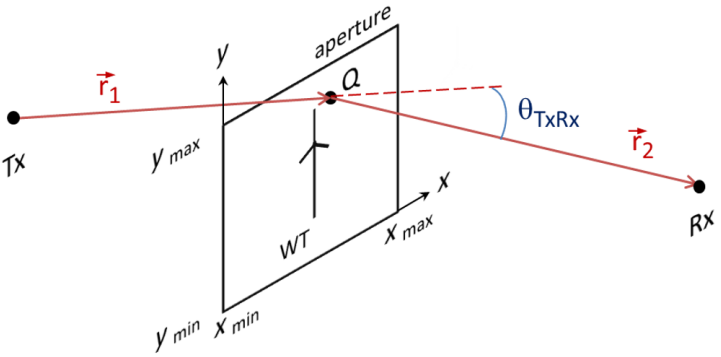

Figure 3-2: Aperture used for 2D Fresnel approximation of WT forward scattering [112]

A typical setting of a WT obstructing a signal path is represented in Fig. 3-2. A transmitter (Tx) is located at $\vec{r_1}$=(x_{Tx}, y_{Tx}, -d_1) at a distance of d_1 in front of the plane of obstruction, while a receiver (Rx) is located at a distance of d_2 behind the plane of obstruction at $\vec{r_2}$=(x_{Rx}, y_{Rx}, d_2). The plane of obstruction is illuminated according to the complex antenna pattern of the transmitter. The WT geometry is projected into the plane of obstruction to form the aperture, which is defined by the function $A(x, y)$ such that

$$A(x,y) = \begin{cases} 1 & \text{for no obstruction at (x,y)} \\ 0 & \text{for obstruction at (x,y).} \end{cases} \tag{3.4}$$

Due to the rotation of the WT blades, $A(x, y)$ is also a function of time. The 2D Diffraction model uses the Huygens-Fresnel principle to determine the resultant electric field amplitude E_P at a point P behind the aperture by the superposition of all secondary wavelets from the wavefront at the aperture.

3.3.1 Non Illuminated Ground Plane

For scenarios where the ground plane is assumed to be not illuminated, E_P can be determined by the equation below

$$E_P = j\frac{E_S}{\lambda}\int\int AP(x,y)A(x,y)F(\theta_{\text{TxRx}})\frac{e^{-jk(r_1+r_2)}}{r_1 r_2}dxdy \tag{3.5}$$

where E_S is the electric field amplitude at unit distance of the source, $AP(x,y)$ represents the complex antenna pattern of the transmitter, which can be taken as 1 for nondirectional antennas (here in the Cartesian coordinate system utilized for the integration), $F(\theta_{\text{TxRx}})$ is the obliquity factor given by

$$F(\theta_{\text{TxRx}}) = \frac{1+\cos(\theta_{\text{TxRx}})}{2} \tag{3.6}$$

k is the wavenumber, λ is the wavelength, r_1=$|\vec{r_1}|$ is the distance from the phase center of the transmit antenna to point $Q = (x,y,0)$ on the plane of obstruction, and r_2=$|\vec{r_2}|$ is the distance from the point Q to the phase center of the receive antenna.

For a good approximation, the integration in eqn. (3.5) should be performed numerically over a sufficiently large area defined by the coordinates $x = x_{\text{min}}\ldots x_{\text{max}}, y = y_{\text{min}}\ldots y_{\text{max}}$ (e.g. more than ten Fresnel zones). This holds true until the grid resolution is much larger than width of the obstructed Fresnel zones.

For a well illuminated aperture, the numerical integration in eqn. (3.5) can require a considerable amount of computation time. To ensure a faster computation, an artifice based on the Babinet's principle can be used [111]. This approach considers the integration area of eqn. (3.5) for three separate scenarios ; (a) obstruction by entire WT geometry, (b) obstruction by the complementary aperture of the rotor, and (c) obstruction by WT tower. This is shown in Fig. 3-4. Since the sum of the received field amplitude of case (a) and (b) is equal to the received field amplitude of case (c), $E_{P(\text{a})}$ can be calculated as

$$E_{P(\text{a})} = E_{P(\text{c})} - E_{P(\text{b})} \tag{3.7}$$

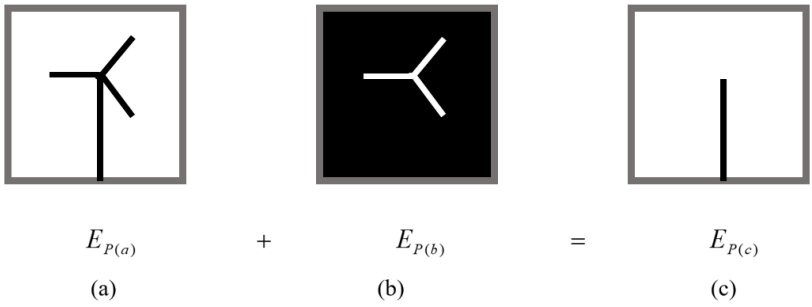

Figure 3-3: Modified Babinet's principle: (a) obstruction by WT, (b) obstruction by complementary rotor, and (c) obstruction by WT tower with respective received field amplitude $E_{P(a)}$, $E_{P(b)}$, and $E_{P(c)}$ [112]

The received field amplitudes for cases (a) and (b) ($E_{P(a)}$ and $E_{P(b)}$ respectively) have to be calculated for each value of rotor angle ϕ, whereas for case (c) the field amplitude $E_{P(c)}$ has to be determined only once, since the tower remains stationary. Moreover, the numerical integration of eqn. (3.5) for cases (b) is performed much faster compared to that of case (a) due to smaller lit area. By using this artifice, a significant reduction in the computational effort can be achieved. For rotor angles where an overlap of the rotor and tower is observed in the plane of obstruction, the overlap area should be removed from the aperture of the complementary rotor.

3.3.2 Illuminated Ground Plane

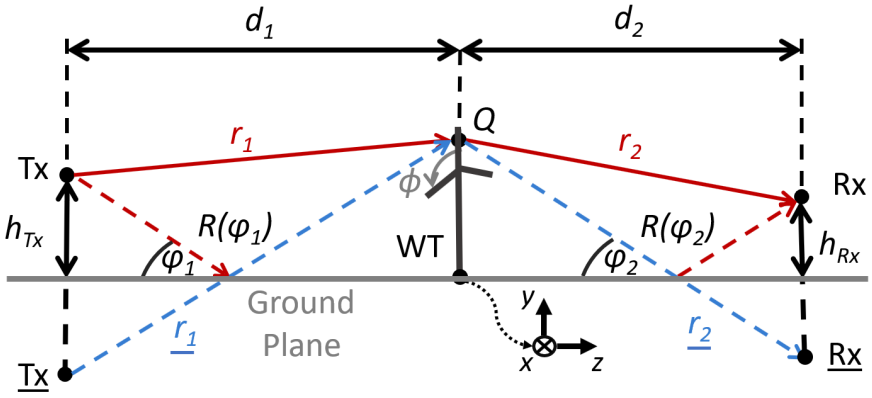

Figure 3-4: WT on ground plane: Forward scattering at point Q obtained as the superposition of 4 paths: Tx–Q–Rx, $\underline{\text{Tx}}$–Q–Rx, Tx–Q–$\underline{\text{Rx}}$, and $\underline{\text{Tx}}$–Q–$\underline{\text{Rx}}$ [111]

To account for the reflections from an illuminated ground plane, the antenna image theory can be used. Instead of computing the ground reflections between the transmitter Tx and the WT, an image transmitter $\underline{\text{Tx}}$ located at $\vec{r}_{\underline{\text{Tx}}}=(x_{\text{Tx}}, -y_{\text{Tx}}, -d_1)$ can be considered, as shown in Fig. 3-4 . Similarly, the reflection between the WT and the receiver Rx can be approximated by assuming an image receiver $\underline{\text{Rx}}$ located at $\vec{r}_{\underline{\text{Rx}}}=(x_{\text{Rx}}, -y_{\text{Rx}}, d_2)$. For each point Q on the aperture, the contributions of four signal paths Tx–Q–Rx, $\underline{\text{Tx}}$–Q–Rx, Tx–Q–$\underline{\text{Rx}}$, and $\underline{\text{Tx}}$ –Q– $\underline{\text{Rx}}$ are considered. The associated phase shifts for each path is given by the corresponding respective reflection coefficients $R(\varphi_1)$ and $R(\varphi_2)$. The resultant field amplitude at the receiver can be obtained by the superimposition of individual contributions from the four paths, followed by an integration over the entire aperture. For the integration, the lower limit in the plane of obstruction (y_{min}) is dictated by the ground plane located at y=0. Assuming the electric field vectors of all paths to be collinear, the field at the receiver can thus be given as

$$E_P = j\frac{E_S}{\lambda}\int\int A(x,y)\Bigg[F(\theta_{\text{TxRx}})\frac{e^{-jk(r_1+r_2)}}{r_1 r_2} + R(\varphi_1)F(\theta_{\underline{\text{Tx}}\text{Rx}})\frac{e^{-jk(\underline{r_1}+r_2)}}{\underline{r_1} r_2} + R(\varphi_2)F(\theta_{Tx\underline{Rx}})\frac{e^{-jk(r_1+\underline{r_2})}}{r_1\underline{r_2}} + R(\varphi_1)R(\varphi_2)F(\theta_{\underline{Tx}\,\underline{Rx}})\frac{e^{-jk(\underline{r_1}+\underline{r_2})}}{\underline{r_1}\,\underline{r_2}}\Bigg]dxdy \tag{3.8}$$

where the diffraction angle θ_{TxRx} for the path Tx–Q–Rx is given by

$$\theta_{\text{TxRx}} = \arccos\frac{\vec{r_1}\vec{r_2}}{r_1 r_2} \tag{3.9}$$

the diffraction angle $\theta_{\underline{\text{Tx}}\text{Rx}}$ for the path $\underline{\text{Tx}}$–Q–Rx is

$$\theta_{\underline{\text{Tx}}\text{Rx}} = \arccos\frac{\vec{r_1}\vec{r_2}}{\underline{r_1} r_2} \tag{3.10}$$

the diffraction angle $\theta_{\text{Tx}\,\underline{\text{Rx}}}$ for the path Tx–Q–$\underline{\text{Rx}}$ is given by

$$\theta_{\text{Tx}\,\underline{\text{Rx}}} = \arccos\frac{\vec{r_1}\vec{r_2}}{r_1\underline{r_2}} \tag{3.11}$$

and the diffraction angle $\theta_{\underline{\text{Tx}}\,\underline{\text{Rx}}}$ for the path $\underline{\text{Tx}}$–Q–$\underline{\text{Rx}}$ is given by

$$\theta_{\underline{\text{Tx}}\,\underline{\text{Rx}}} = \arccos\frac{\vec{r_1}\vec{r_2}}{\underline{r_1}\,\underline{r_2}}. \tag{3.12}$$

The angle of incidence φ_1 (between wave vector and ground plane) in front of the plane of obstruction is given by

$$\varphi_1 = \arcsin\left(\frac{y + y_{\text{Tx}}}{\underline{r_1}}\right). \tag{3.13}$$

Similarly, the corresponding angle behind the plane of obstruction φ_2 is given by

$$\varphi_2 = \arcsin\left(\frac{y + y_{\text{Rx}}}{r_2}\right). \tag{3.14}$$

The signal reflected from the ground plane experiences a change in amplitude and phase in accordance to the ground's reflection coefficient R, which depends on material parameters (relative permittivty ϵ_r and conductivity σ) along with the signal polarization (defined according to Fig. 3-5) , and is calculated as shown below [129]

$$R(\varphi) = \begin{cases} \frac{\sin\varphi - \sqrt{\epsilon_r - j\sigma/\omega\epsilon_o - \cos^2\varphi}}{\sin\varphi + \sqrt{\epsilon_r - j\sigma\omega\epsilon_o - \cos^2\varphi}} & \text{Hor. Pol.} \\ \frac{(\epsilon_r - j\sigma/\omega\epsilon_o)\sin\varphi - \sqrt{\epsilon_r - j\sigma/\omega\epsilon_o - \cos^2\varphi}}{(\epsilon_r - j\sigma/\omega\epsilon_o)\sin\varphi + \sqrt{\epsilon_r - j\sigma/\omega\epsilon_o - \cos^2\varphi}} & \text{Vert. Pol.} \end{cases} \tag{3.15}$$

The complex reflection coefficient R of eqn. (3.15) can be represented in terms of the corresponding changes in amplitude ρ and phase ς as shown below

$$R = \rho e^{j\varsigma}. \tag{3.16}$$

The polarization of the incident wave has a strong impact on the value of R. If the ground plane is perfectly conducting (PEC), all incident waves are considered to be almost completely reflected (ρ = 1) assuming no absorption losses . Figure 3-5 defines the orientation of the field vectors after reflection from a PEC plane, where the subsripts i and r are used for incident and reflected field vectors respectively. As a 180° phase shift is already provided by the definition of the field vector E_r for the grazing angle φ, a vertically polarized wave would be reflected by a PEC plane without phase shift (ς =0°, thus R=+1). In contrast, a horizontally polarized wave would be out of phase upon reflection (ς =180°, thus R=-1) [13, 129]. Reflections from finite conductivity (lossy) grounds can be taken into account by using the appropriate reflection coefficient as calculated by eqn. (3.15).

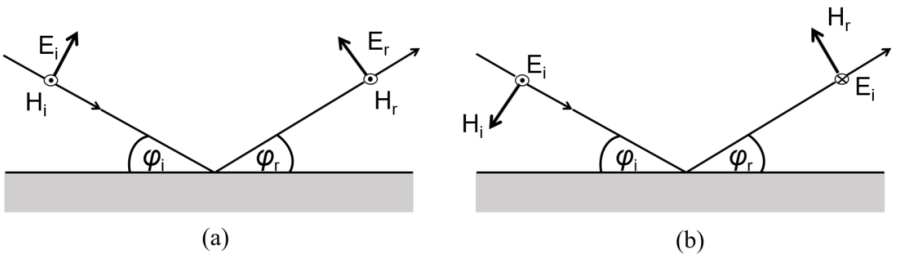

Figure 3-5: Definition of field vectors for signal reflection from PEC plane a) vertical polarization b) horizontal polarization; Phase shift of 180° inherent to definition of E_r

3.4 Verification and Discussion

For the verification of the diffraction models presented in this chapter, the values calculated for the received signal strength are compared with UTD simulation results obtained by FEKO. Figure 3-6 shows general parameters of the scenarios considered for the discussions presented henceforth. For the 2D model, the three blade rotor shown in Fig. 3-6 is used, whereas for the 1D model, only one blade of identical width is considered. The rotor blades are assumed to be rectangular in shape with length l_b and width w_b. The WT hub is located right on top of the tower at a height of h_{tow}. Assuming the same height of Tx and Rx (h_{Tx}=h_{Rx}), y_{off} and x_{off} are the vertical and horizontal offset of the LOS path from the rotor axis respectively. The value of y_{off} is positive when the LOS path lies above the rotor axis and negative below it. The horizontal offset x_{off} is taken to be positive when the LOS path lies on the left of the rotor axis, as viewed from the transmitter and vice versa. Figure 3-6 shows the case when both y_{off} and x_{off} are positive.

To verify the 1D Diffraction model, first a point-to-point radio link obstructed only by a cylindrical tower is considered. The tower is assumed to have a diameter of 6 m and a height of 200 m. Other important parameters considered are d_1 = d_2 = 4000 m, frequency f = 1.3 GHz, h_{Tx} = h_{Rx} = 100 m. Figure 3-7 displays a comparison of the path loss as a function of the horizontal offset x_{off} of the cylinder from the LOS path calculated with UTD

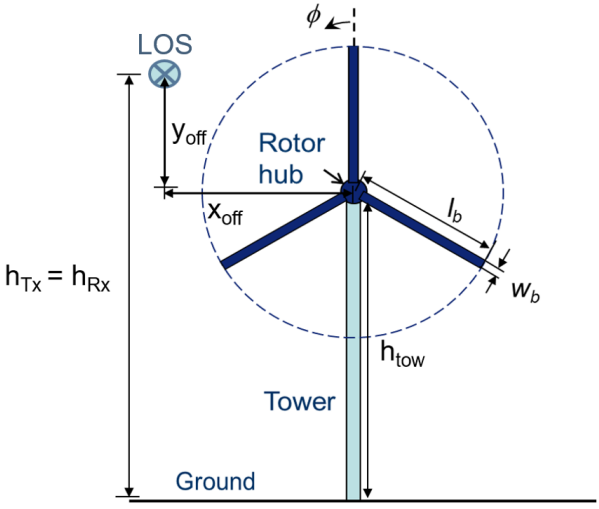

Figure 3-6: General parameters for considered scenarios (as seen from transmitter) - three blade rotor used for 2D model; only positive values of y_{off} and x_{off} displayed

(FEKO) and the diffraction loss $\Delta\alpha$ calculated by the 1D model. Though scattering from the edges of the obstacle is ignored in the Fresnel-Kirchhoff diffraction approach both results agree fairly well even for significant high values of offset. It can be concluded that the signal scattering from the edges as well as reflections contribute very little to the overall received field in the forward scattering region.

Next, the impact of the rotor (Zone 2) is considered. A WT with rectangular blades of length l_b = 64 m and width w_b = 1.5 m is assumed to be at d_1=500 m away from the transmitter while the receiver is located at d_2=7500 m away from the WT. The signal path is set to be 60 m above the rotor axis (close to the tip of the blade; x_{off} = 0 m y_{off} = 60 m). For simplicity the WT tower and ground plane effects are omitted. For a frequency of 1.3 GHz, the calculated values of $\Delta\alpha$ and $\Delta\beta$ vs rotation angle ϕ are shown in Fig. 3-8 a) and b). At ϕ =0°, the upper blade is upright, while at ϕ =60° its distance from the axis of the signal path is the same as that to the next blade following in clockwise direction. Thus, all plots contain an even

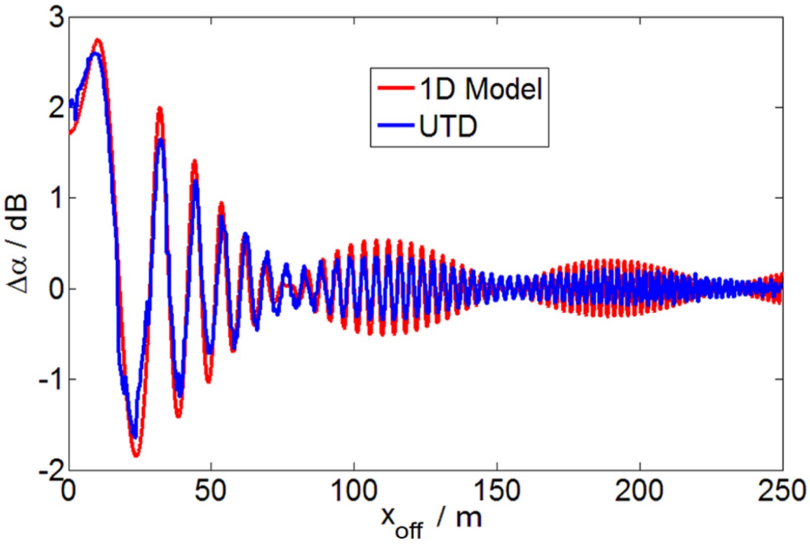

Figure 3-7: Obstructing cylinder of 6 m diameter and 200 m height: Comparison of diffraction loss $\Delta\alpha$ vs offset from LOS path calculated by 1D Model and by 3D field simulation (UTD)

symmetry along ϕ for every 60°. A slight disagreement can be observed between the calculated and simulated curves presented in Fig. 3-8 This can be attributed to the fact that the FEKO simulations consider a rotor with three rectangular blades, whereas the 1D model only takes into account a single infinite long blade. At values of ϕ around 60°, the second rotor blade which is not considered in the 1D model starts approaching the signal path to the same extent as the first blade. It is however, interesting to note that for most values of the rotor angle ϕ, the two results seem to have a good agreement.

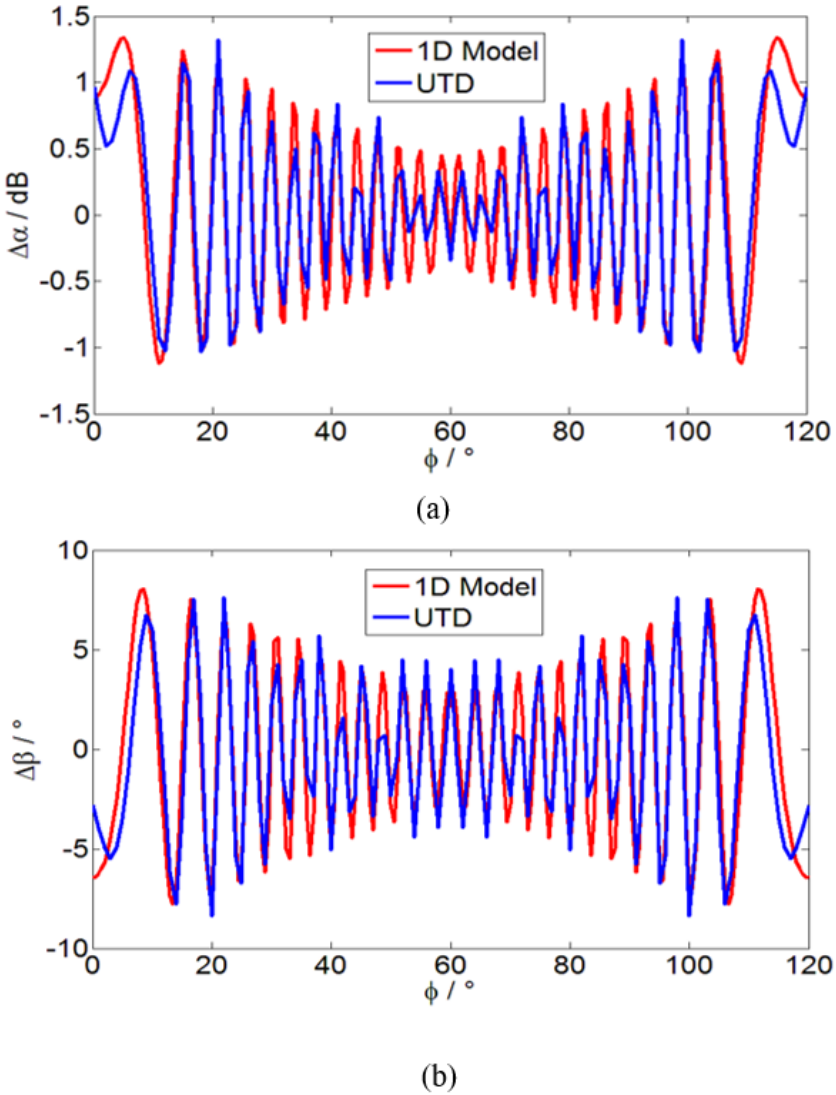

Figure 3-8: (a) $\Delta\alpha$ and (b) $\Delta\beta$ vs rotor angle ϕ calculated by (UTD) and obtained with 1D Fresnel diffraction model; for d_1 = 500 m and d_2 = 7500 m, signal axis 60 m right below rotor axis, no ground plane considered.

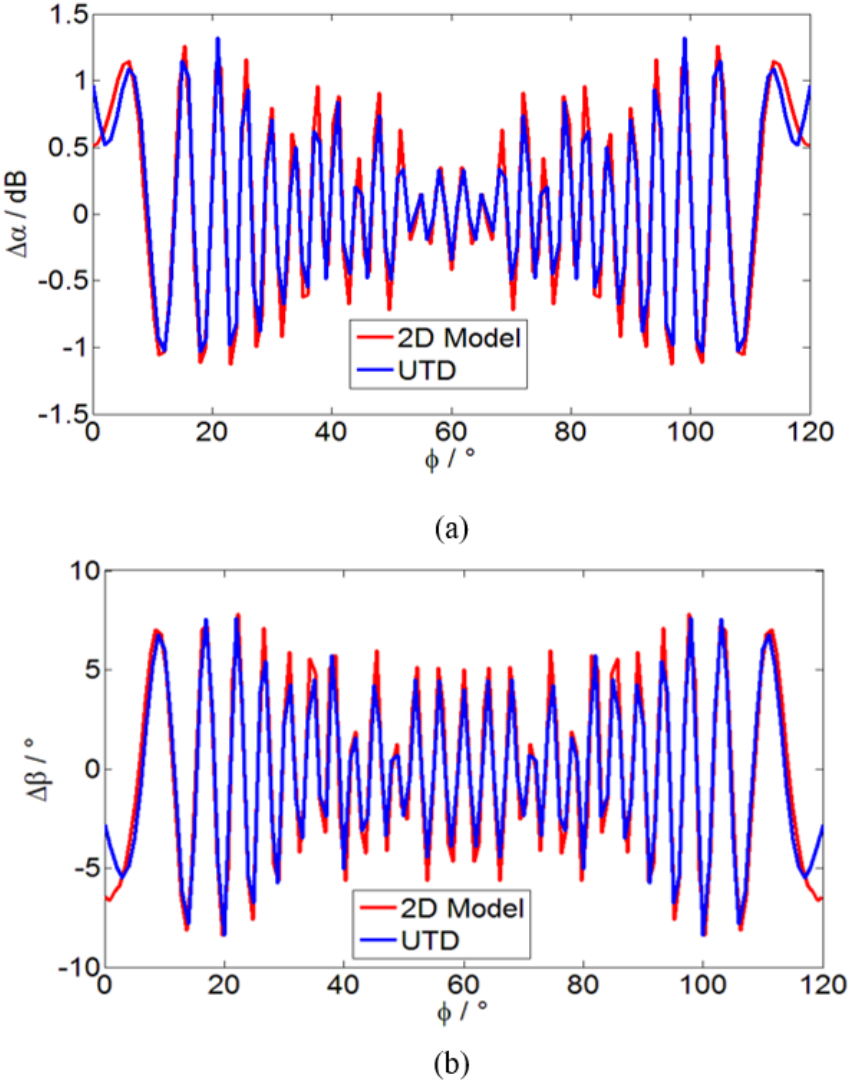

Figure 3-9: (a) $\Delta\alpha$ and (b) $\Delta\beta$ vs rotor angle ϕ calculated by (UTD) and obtained with 2D Fresnel diffraction model; for d_1= 500 m and d_2 = 7500 m, signal axis 60 m right below rotor axis, no ground plane considered.

The same scenario is considered for the verification of the 2D model and the results obtained are shown in Fig. 3-9. While the results obtained by the 1D model (Fig. 3-8) seem to be less accurate for ϕ=0 (close to the LOS path) and ϕ=60° (midway between two blades), the 2D model results agree very well with the UTD simulation. This underlines the fact that for a comprehensive characterization of WT diffraction effects, it is important to consider the three blades. It can also be concluded that the scattering from the blade edges contributes only very little to the overall field at the receiver.

Next, the WT rotor is considered to be midway between the transmitter and the receiver (d_1 = 4000 m and d_2 = 4000 m), while the rotor axis is aligned collinear 90 m right above the line of sight (LOS) path between Tx and Rx (x_{off} = 0 m y_{off} = -90 m). Figure 3-10 displays a comparison of the values of $\Delta\alpha$ as well as $\Delta\beta$ versus rotor angle ϕ obtained by the 2D model and by UTD simulations. It can be seen that the results have an almost perfect match.

For a verification of the illuminated ground plane approach, the scenario of Fig. 3-10 is modified by adding a perfect conducting (PEC) ground plane 10 m below the transmitter and receiver, thus making the rotor axis to be 100 m above the ground. Signal polarization is assumed to be vertical (R=+1 as defined in Fig. 3-5). In the absence of the WT, this setting produces an almost ideal constructive interference between the LOS path and the ground reflected path. It can be seen in Fig. 3-11 that the values of $\Delta\alpha$ and $\Delta\beta$ versus rotor angle ϕ for the WT rotor on PEC ground obtained by the 2D Model and by UTD simulations agree pretty well. The maximum values of the calculated diffraction loss and obstacle gain is in the order of 0.8 dB and 1.2 dB at ϕ =15° and ϕ =21°, respectively.

Next, the height of the transmitter and receiver is increased to 20 m without changing any of the other parameters. This new setting results in a destructive interference of the LOS path and the ground reflected path. Again, as shown in Fig. 3-12 a good agreement is observed between the calculated and UTD simulated values. It is also interesting to note the maximum values of diffraction loss (6.3 dB at ϕ=14°) and obstacle gain (3.5 dB at ϕ=10°) as well as maximum phase shift $\Delta\beta$ (32° instead of 7.6°) are much higher than the previous case of constructive interference.

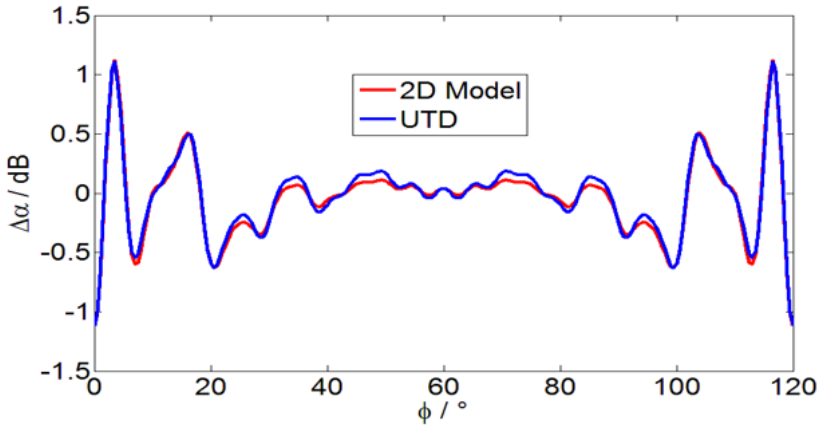

(a)

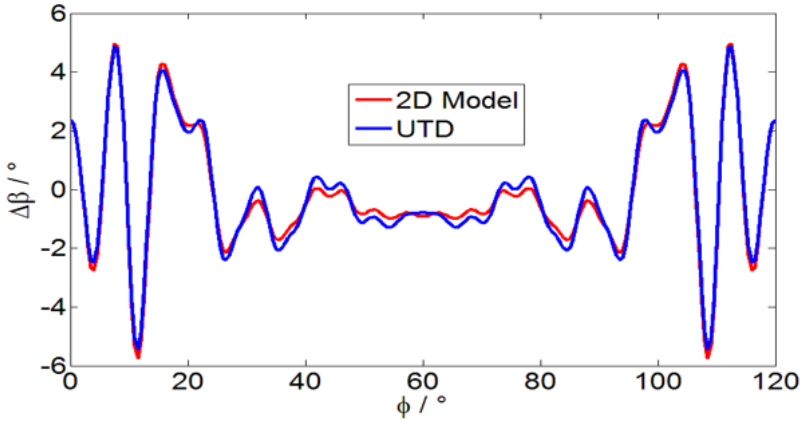

(b)

Figure 3-10: (a) $\Delta\alpha$ and (b) $\Delta\beta$ vs rotor angle ϕ calculated by (UTD) and obtained with 2D Fresnel diffraction model; for d_1= d_2 = 4000 m, signal axis 60m right below rotor axis, no ground plane considered.

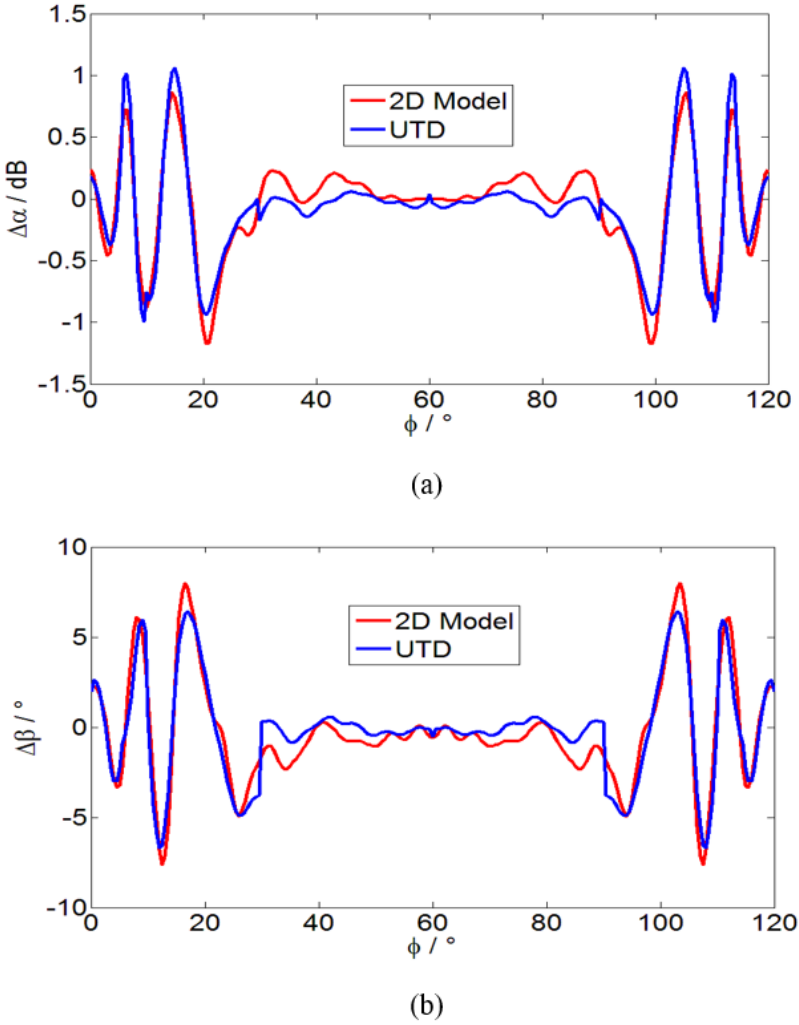

Figure 3-11: (a) $\Delta\alpha$ and (b) $\Delta\beta$ vs rotor angle ϕ calculated by (UTD) and obtained with 2D Fresnel diffraction model; for $d_1 = d_2$ = 4000 m, signal axis 60m right below rotor axis, PEC ground plane 10m below Tx and Rx.

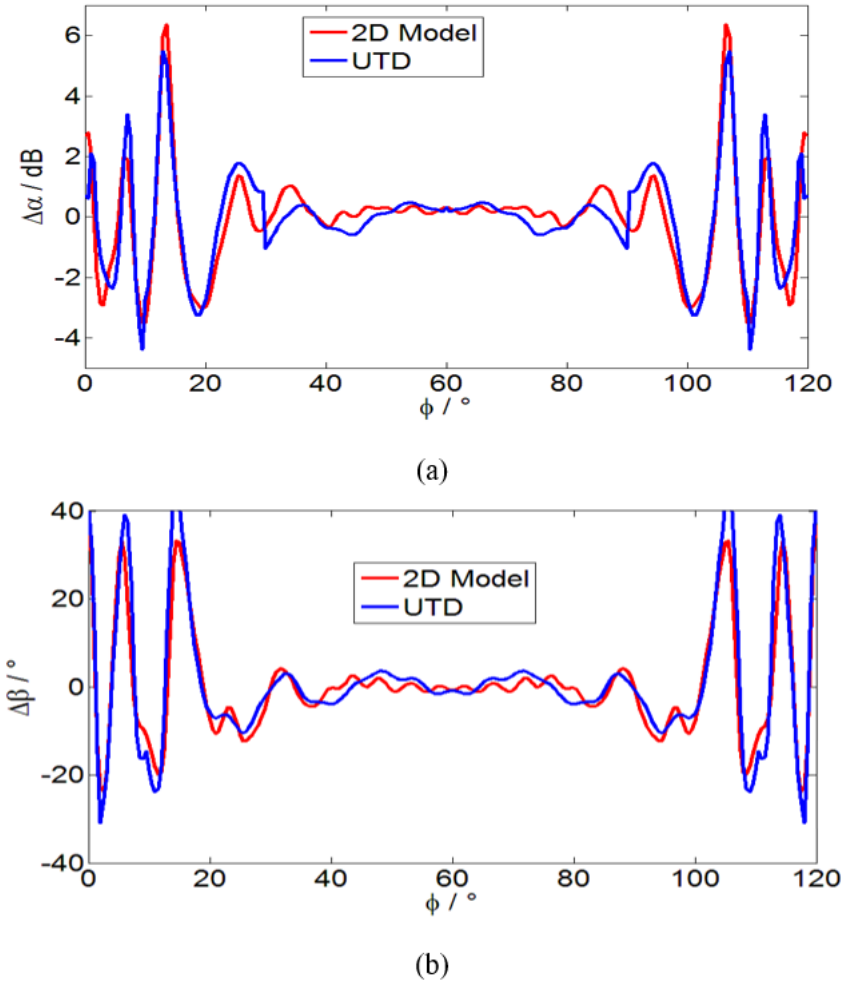

Figure 3-12: (a) $\Delta\alpha$ and (b) $\Delta\beta$ vs rotor angle ϕ calculated by (UTD) and obtained with 2D Fresnel diffraction model; for d_1= d_2 = 4000 m, signal axis 60m right below rotor axis, PEC ground plane 20m below Tx and Rx.

3.5 Summary

This chapter presented a brief overview of various simulating techniques that can be used for the prediction and characterization of WTI. The suitability of Fresnel diffraction approach in efficiently and effectively modelling WT forward scatter has been explored, starting with a 1D diffraction model for the calculation of the dynamic amplitude $\Delta\alpha$ and phase modulation $\Delta\beta$. While this model is simple to use and can be used for a decent approximation of WT forward scatter, it has certain major shortcomings regarding its accuracy and ability to handle complex scenarios. It does not account for the impact of an illuminated ground plane which further limits its application. Furthermore, it is only applicable for some selected geometries. A more accurate and versatile 2D Fresnel-Kirchhoff diffraction approach has been applied to overcome the limitations of the 1D model and the results have been verified by comparison with those obtained by 3D field simulations. It has been shown that scattering from blade edges – which is not accounted for in the 1D and 2D models – has little contribution to the overall received field. Impact of an illumintaed ground plane has been accounted for by considering an image transmitter and an image receiver. It has been shown that link settings which produce a destructive interference of the LOS and ground reflected paths are more prone to provide high values for the maximum diffraction loss, obstacle gain and phase variation as compared to case when a constructive interference exists between the LOS and ground reflected paths. From all the results presented, it can be observed that the 2D Fresnel-Kirchhoff diffraction model results agree well with those obtained by UTD and thus can be efficiently used for the modelling and analysis of WT forward scatter. The forward scatter plots in this chapter contain seemingly well-organized patterns of alternating maxima of obstacle gain and obstacle loss, which further underline the importance to an in-depth analysis of the mechanisms involved. The discussion in the following chapters aims to develop a comprehensive understanding of the WT forward scatter.

4 Qualitative Analysis of WT Forward Scatter

Diffraction by a WT results in obstruction loss as well as in obstruction gain in the forward scatter region [117]. Moreover, the rotation of the blades causes a periodic amplitude and phase modulation of the forward scattered signal which in turn results in a periodic frequency deviation of the signal [118]. In order to improve the performance of radar and radio communication systems under these conditions, it is imperative to have an analytical understanding of the signal modulation by the rotating blades. WTI investigations in the forward scatter region have mainly been performed using a case to case approach using numerical field simulations without an analytical insight into the time variant pattern of those signals [76, 91, 92]. The interpretation of patterns of time variant amplitude and phase distortion appears to be even more complicated when an illuminated ground plane is taken into consideration. The typical lobbing effect due to an illuminated ground plane has been observed in the field distribution behind the WT or in the plane of obstruction [74]. However, this complex field pattern does not provide an immediate analytical insight into the time variant pattern of amplitude and phase distortion caused by the WT.
In this Chapter, a qualitative analysis of WT forward scatter is presented. The amplitude and phase modulation due to WT diffraction is examined by using the 2D Fresnel-Kirchhoff diffraction model. The patterns of time variant amplitude and phase distortion caused by the diffraction by WT rotor are explained by taking into account the obstructed Fresnel zones. A similar approach is then applied to study the impact of the static tower. The impact of an illuminated ground plane is then investigated by inspecting the obstruction of the Fresnel zones of the four paths (Tx–Rx, Tx–Rx, Tx–Rx and Tx–Rx). This detailed analysis provides an in-depth

insight into forward scattering of radar and radio communication signals at a WT which lies beyond the investigation of case by case studies based on 3D numerical field simulations. To make the task of understanding of WT diffraction mechanisms easier, propagation scenarios have been chosen such that it is convenient to visualize the impact of the rotating blades on the field at the receiver. The rotor blades are assumed to be rectangular in shape. Other blade shapes will be investigated in chapter 6. The simple rectangular shape makes it easier to fully understand the dynamics of the signal modulation. All simulations have been performed using MATLAB.

4.1 Diffraction by WT Rotor

For the analysis of the WT diffraction patterns, first only the impact of the rotor is considered [125]. The scenario under consideration assumes an operational frequency of 1.3 GHz. The distance between the transmitter and the plane of obstruction is d_1 = 4000 m and the distance between the plane of obstruction and receiver is d_2 = 4000 m. A rotor with three rectangular blades of length l_b = 64 m and width w_b = 1.5 m is considered. The rotor axis is aligned collinear 60 m right below the LOS path (y_{off}=60 m ; Fig. 4-1(right)). The beam of the transmitting antenna is assumed to be wide enough such that a significant number of Fresnel zones are illuminated. Figure 3-2 can be used to visualize the scenario under consideration (by omitting the WT tower, thus assuming just the rotor partly obstructing an incident beam instead of an entire WT). In the absence of an obstruction, the phase of the received signal is equal to that of the LOS path. The signal at Rx is the sum of the individual contributions from all the Fresnel zones. The shortest path between the transmitter and receiver is the LOS path (Tx-Rx). Owing to their larger path lengths, all other possible paths (Tx-Q-Rx) will contribute to the overall field with a larger phase compared to that of the LOS path. As the distance from the center of the first Fresnel zone increases, the phase of any path Tx-Q-Rx will also increase. Thus, the contributions from higher order Fresnel zones will have a larger phase. Due to the factor j in the Fresnel-Kirchhoff Formula (eqn. (3.5)), the signal phase in the center of the 1st Fresnel zone is advanced by $\pi/2$ compared to the LOS path. Thus, at the boundary of the 1st Fresnel zone, the signal phase is retarded by $\pi/2$ as compared to the LOS path.

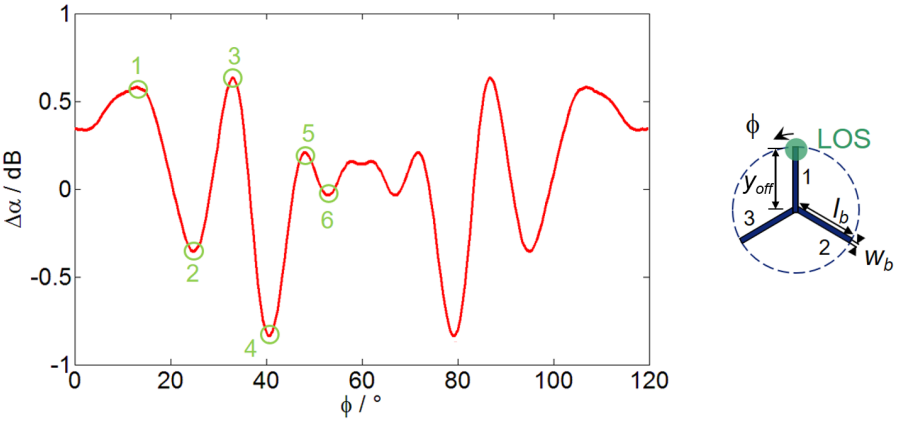

Figure 4-1: Diffraction loss $\Delta\alpha$ vs rotor angle ϕ (left) for the three-blade rotor setting considered (right). The digits in green next to the peaks represent the obstructed Fresnel zones.

Figure 4-1 shows the diffraction loss $\Delta\alpha$ versus rotor angle ϕ for the scenario under analysis. The position of the rotor blades along with the LOS path is shown in the illustration on the right in Fig. 4-1. The rotor angle ϕ is counted counterclockwise, with ϕ=0 representing the orientation with one blade vertically pointing upwards (as shown in Fig. 4-1). Figure 4-2 shows the orientation of the rotor blades along with the Fresnel zones in the plane of obstruction for rotor angles corresponding to the maximum and minimum values of $\Delta\alpha$ displayed in Fig. 4-1. The first maximum of the obstruction loss occurs at ϕ=13.5°. The corresponding rotor orientation is shown in Fig.4-2 (a), where one blade lies inside the 1st Fresnel zone. The maximum obstruction loss can be expected for blade positions which result in the maximum obstruction of the in-phase signal of the whole beam. For a significant number of illuminated Fresnel zones (wide beam of the transmit antenna), the contribution of the 1st Fresnel zone is in-phase with the whole beam. The signal has a phase advancement of $\pi/2$ in the center and a $\pi/2$ phase retardation at the outer boundary of the 1st Fresnel zone compared to that of the whole contribution of the 1st Fresnel zone. Between these two extremes, the signal is in-phase with the whole beam. At this point, the corresponding path difference with respect to the LOS

path is $\lambda/4$ (see Fig. 2-6). By using $\Delta d = \lambda/4$ in eqn. (2.20), we get

$$\begin{aligned} \frac{\lambda}{4} &= \frac{h_{\mathrm{ke}}^2}{2}\left(\frac{d_1+d_2}{d_1 d_2}\right) \\ h_{\mathrm{ke}} &= \sqrt{\frac{\lambda d_1 d_2}{2(d_1+d_2)}} \\ h_{\mathrm{ke}} &= \frac{1}{\sqrt{2}} R_1. \end{aligned} \tag{4.1}$$

In eqn. (4.1) , h_{ke} represents the radial distance from the LOS path where the maximum obstruction of the in-phase signal inside the first Fresnel zone occurs. Thus, the maximum obstruction loss can be expected when a blade is positioned at about $1/\sqrt{2}$ times the radius of the first Fresnel zone (in this case at ϕ=13.5°). In Fig. 4-1, the first maximum of obstruction gain occurs at ϕ = 24.5°, which corresponds to one rotor blade lying tangentially inside the second Fresnel zone (Fig. 4-2 (b). The signal contribution of the second Fresnel zone is retarded in phase by π compared to that of the first Fresnel zone, and thus interferes destructively. A maxima of obstruction gain can be expected at rotor angles where this destructive interfering signal is being obstructed. In the considered example, the blade tangentially aligned inside the second Fresnel zone at ϕ = 24.5° is causing an obstruction of the destructive interfering signal and consequently a maxima of obstruction gain is observed. A general conclusion can be drawn that the maxima of obstruction loss occurs for blade orientations tangentially aligned inside an odd Fresnel zone and maxima of obstruction gain occur for blade orientations tangentially aligned inside an even Fresnel zone. Therefore, the maxima of $\Delta\alpha(\phi)$ in Fig. 4-1 at ϕ =33.5° and ϕ =48° can be attributed to a blade (blade 1 in this case) tangentially obstructing the 3rd and 5th Fresnel zone (Fig. 4-2 (c), (e)) respectively. Similarly, the minima of $\Delta\alpha(\phi)$ at ϕ = 41° and ϕ= 53° are caused by blade 1 tangentially oriented in the 4th and 6th Fresnel zone (Fig. 4-2 (d), (f)) respectively. Due to the three blade rotor, the $\Delta\alpha(\phi)$ plot has an even symmetry along ϕ for every 60°.

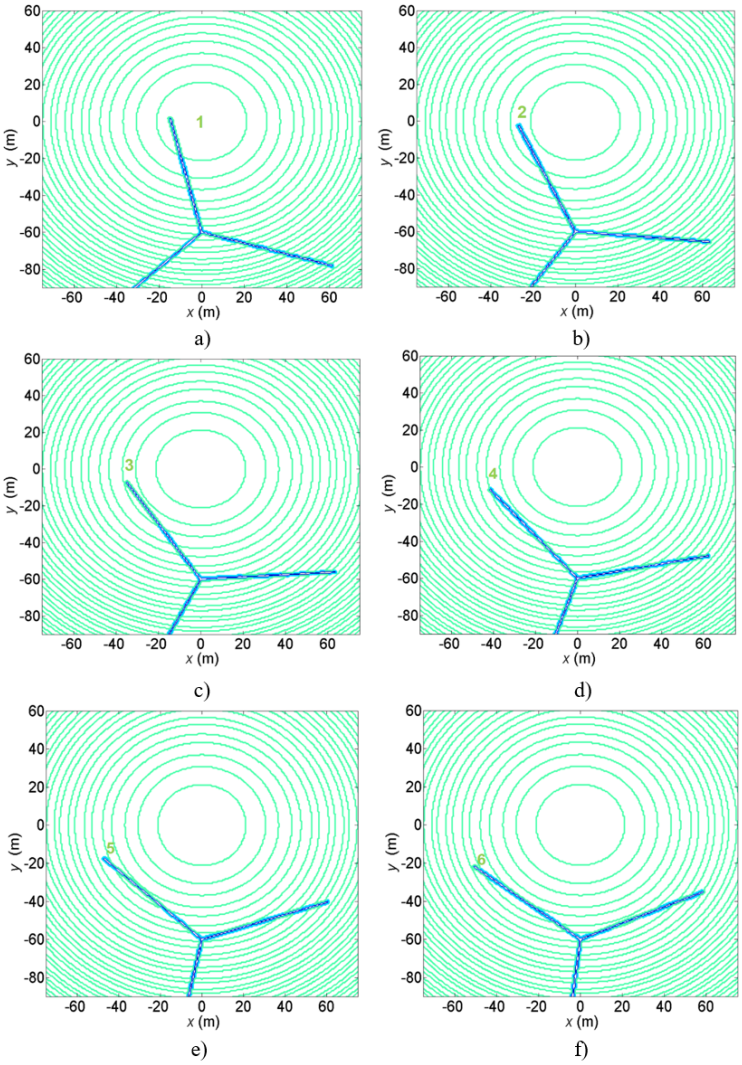

Figure 4-2: Plane of obstruction: rotor (blue) and Fresnel zones (green) (a) ϕ=12°, (b) ϕ=24.5°, (c) ϕ=33°, (d) ϕ=40.5°, (e) ϕ=47°, (f) ϕ=53°; offset of LOS path y_{off}=60m above rotor axis

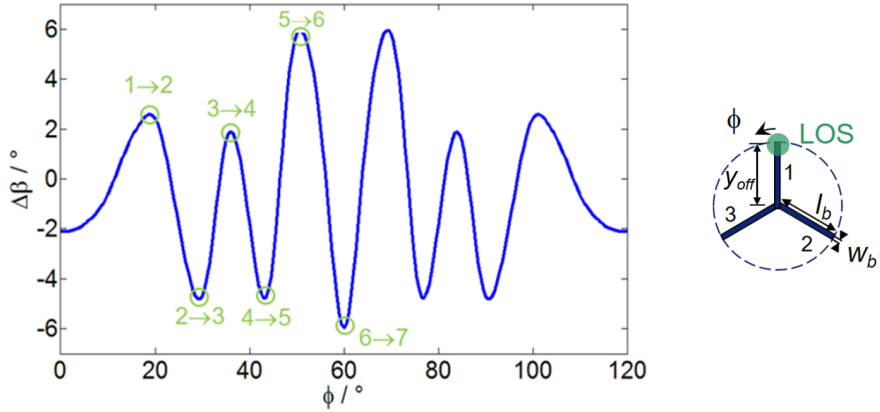

Figure 4-3: Phase shift $\Delta\beta$ vs rotor angle ϕ (left) for the three-blade rotor setting considered (right).

Another notable effect of a three blade rotor is that two blades can both be tangentially aligned to the Fresnel zones at the same time. In the considered example, this occurs at ϕ=60°, ϕ=180° and ϕ=300°. The interaction of the diffracted fields from the two blades is significant as the individual contributions from each of the blades add together. This is discussed in more detail in the following.

The corresponding $\Delta\beta(\phi)$ plot is displayed in Fig. 4-3. Maxima of the curve occur at rotor angles of 20°, 37°, and 51° while the minima are observed at 30°, 43.5°, and 60°. The corresponding positions of the rotor blades are shown in Fig. 4-4. It can be observed that the maxima of $\Delta\beta(\phi)$ occur at rotor angles where one blade is located at the outer boundary of an odd Fresnel zone, whereas the minima occur for rotor angles when one blade is oriented at the outer boundary of an even Fresnel zone. If a Fresnel zone is being tangentially obstructed by a single blade, such that the blade width w_b is smaller than the width of the Fresnel zone, $\Delta\beta$ is expected to diminish significantly for values of ϕ where the maxima and minima of $\Delta\alpha$ are observed. However, from Fig. 4-1 and Fig. 4-3, it can be observed that this does not hold true for the extrema of $\Delta\alpha$ for ϕ values between 30°-90°.

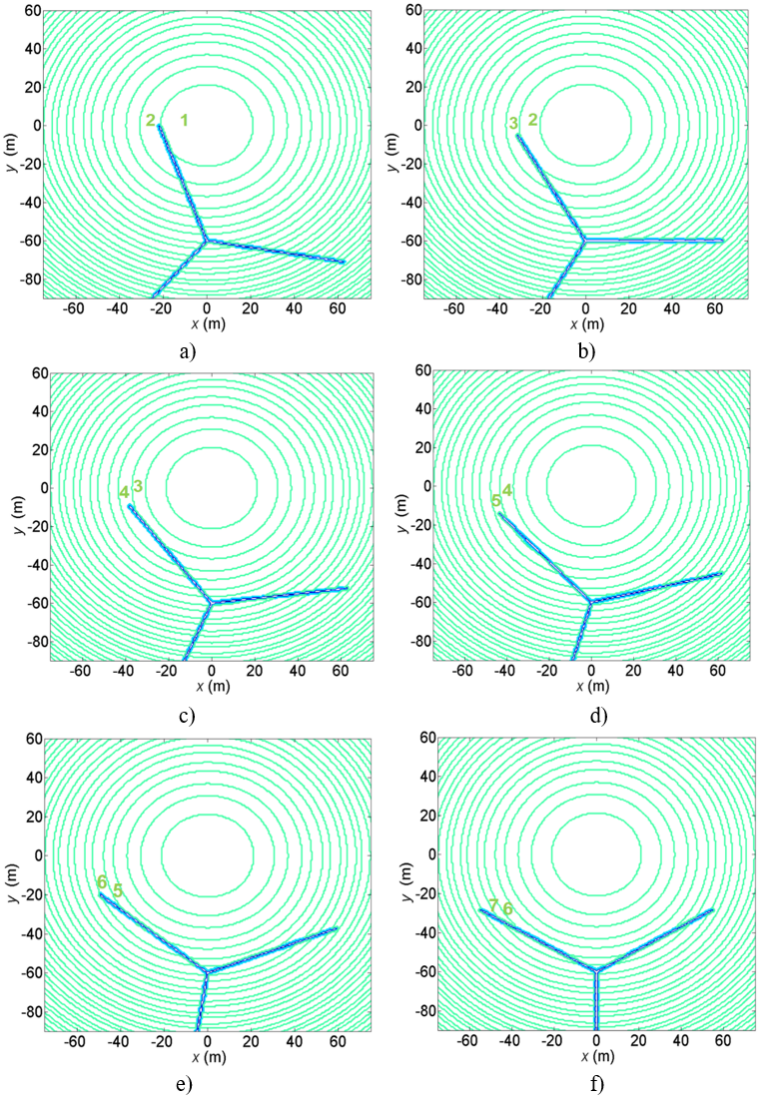

Figure 4-4: Plane of obstruction: rotor (blue) and Fresnel zones (green) for rotor angle (a) ϕ=20°, (b) ϕ=30°, (c) ϕ=37°, (d) ϕ=43.5°, (e) ϕ=51°,(f) ϕ=60°; offset of LOS path y_{off} =60m above rotor axis [125]

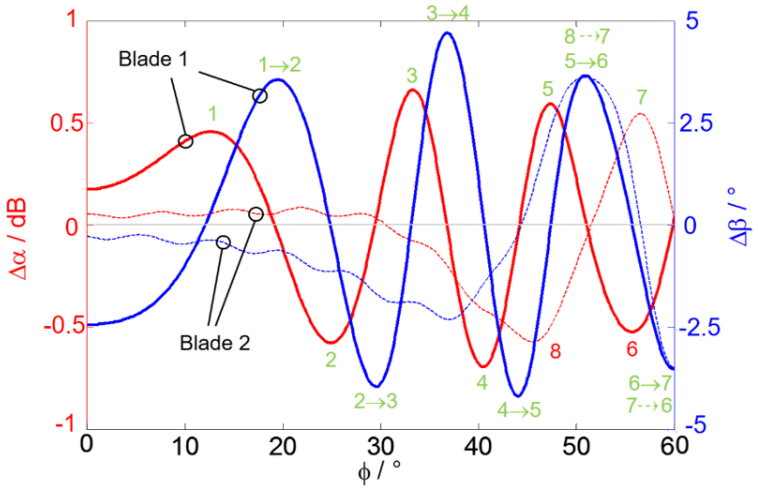

Figure 4-5: diffraction loss $\Delta\alpha$ (red) and phase shift $\Delta\beta$ (blue) vs rotor angle caused by blade 1 (solid lines) and caused by blade 2 (dotted lines); a single number indicates number of Fresnel zone cut tangentially by respective blade at particular ϕ, two numbers with arrow indicate transition of Fresnel zones. [125]

From the corresponding rotor positions for ϕ = 43.5°, 51° and 60° depicted in Fig. 4-4, it can be seen that for all these rotor angles, the illuminated Fresnel zones are being tangentially obstructed by not one but two blades (number 1 and 2). This strongly indicates that the overall diffracted field by the rotor is significantly impacted by the superposition of the contributions of the two blades.

Figure 4-5 shows the individual field contributions of blade 1 and blade 2, with the ϕ axis plotted only till 60° owing to the even symmetry due to the three blades. The overall change in field at the receiver due to the WT rotor is the sum of the individual field contributions of the blades. For instances when two blades are aligned tangential to the Fresnel zones, the third blade is oriented almost perpendicular to the Fresnel zones and has a negligible contribution to the shading of the overall field. During the interval $\phi \approx$ 45°-75°, the individual amplitude modulation caused by blade 1 is almost

completely out of phase compared to that of blade 2. Consequently, only a minor change in the overall $\Delta\alpha$ for the entire rotor (Fig. 4-1) is observed for this interval. The corresponding phase shifts induced by the two blades are almost in phase with each other and produce two maxima (at ϕ= 51° and 69°) and a minimum (at ϕ= 60°) of the $\Delta\beta$ curve for the entire WT rotor, as seen in Fig. 4-1. It is also interesting to note that at ϕ= 51°, blade 1 is moving from Fresnel zone 5 to 6 while blade 2 makes the transition from zone 8 to 7. Both the blades are located at the outer boundary of an odd Fresnel zone, resulting in a maximum of $\Delta\beta$. At ϕ= 60°, both the blades are located at the outer boundary of an even zone with, with blade 1 proceeding from Fresnel zone 6 to zone 7 while blade 8 moving in zone 7 from zone 6, resulting in a minimum of the $\Delta\beta$ curve. It can be concluded that the overall amplitude and phase modulation due to two blades tangentially aligned to the Fresnel zones is dependant on the phase of their individual shaded fields. The mechanical coupling between the blades is such that when one of the two tangentially oriented blades moves towards the LOS path, the other moves away from it. This causes the phase of their respective shaded fields to change rapidly in opposite directions during the rotation of the WT rotor.

In the considered example, when two blade are tangentially oriented with respect to the same Fresnel zone at the same time, an obstruction of the field contribution at the transition from an even to an odd Fresnel zone occurs. This can be seen at ϕ= 60° where both blade 1 and blade 2 are located at the boundary between zones 6 and 7. For other link scenarios, this symmetric rotor position with respect to the LOS path and the consequent phase of the fields shaded by the two blades will depend on the offset of the LOS path from the rotor axis. Thus, the signal modulation by WT rotor will be strongly dependent on the distance between the LOS path and the rotor axis. In the current scenario, the area shaded by the two blades will shift if the vertical offset y_{off} (shown in the illustration on the right in Fig. 4-1) between the LOS path and the rotor axis is varied. For small changes in y_{off}, the phase of the individual field contributions of the two blades will experience rapid shifts in the opposite direction along the ϕ axis, producing significant variations in the $\Delta\alpha(\phi)$ and $\Delta\beta(\phi)$ curves. The impact of y_{off} on diffraction loss $\Delta\alpha$ and phase shift $\Delta\beta$ is shown in Fig. 4-6. It can be seen that small changes (from 57.1 to 62.5m) in distance of the rotor axis from the LOS path produce a variation of almost 2.3 dB

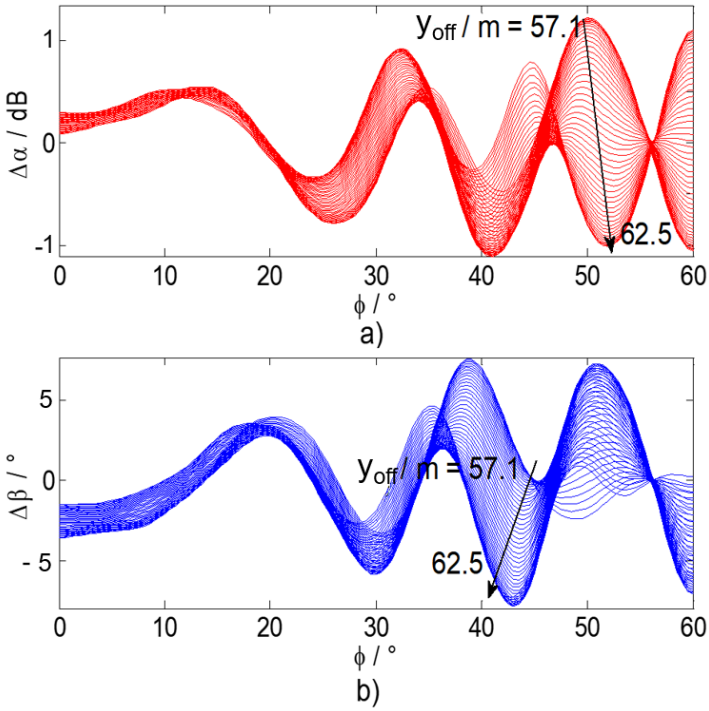

Figure 4-6: Impact of parameter vertical offset of LOS path y_{off} on (a) diffraction loss $\Delta\alpha$, (b) phase shift $\Delta\beta$ [125]

and 18° in maximum values of $\Delta\alpha$ and $\Delta\beta$ respectively. Thus, it can be concluded that the impact of the two blades oriented tangentially to the Fresnel zone is determined by the offset of the LOS path from the rotor axis. In contrast when only one single blade is tangentially aligned to the Fresnel zones, small changes in the value of the said offset do not produce major variations in the $\Delta\alpha(\phi)$ and $\Delta\beta(\phi)$ curves.

4.2 Diffraction by WT Tower

An overlap of the static tower and the dynamic rotor can have an impact on the signal modulation caused by a WT. This interaction consists of two parts as shown in Fig 4-7 [123]:

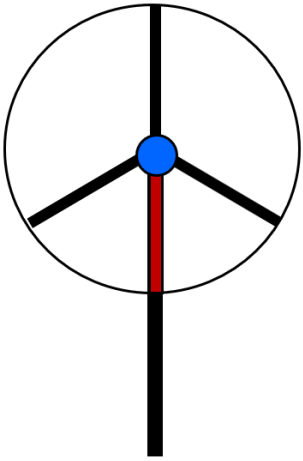

Figure 4-7: Time invariant (blue) and time variant (red) overlap of static tower and dynamic rotor.

- A time-invariant interaction between tower and rotor hub which results in an offset of the DC component of the diffraction loss $\Delta\alpha$ and phase modulation $\Delta\beta$.

- A time-variant interaction between tower and rotor blades which produces a variation of the AC component of $\Delta\alpha$ and $\Delta\beta$.

To study this phenomenon, consider a WT with a tower of height h_{tow} = 98 m, and a hub of radius r_{hub} = 5.5 m. The height of Tx and Rx with respect to the base of the tower is $h_{\text{Tx}} = h_{\text{Rx}}$ = 68 m. The LOS path has a horizontal offset of x_{off} =25 m (to the left) from the rotor axis. All other parameters are same as in the scenario considered in section 4.1 (frequency =1.3 GHz, d_1 =

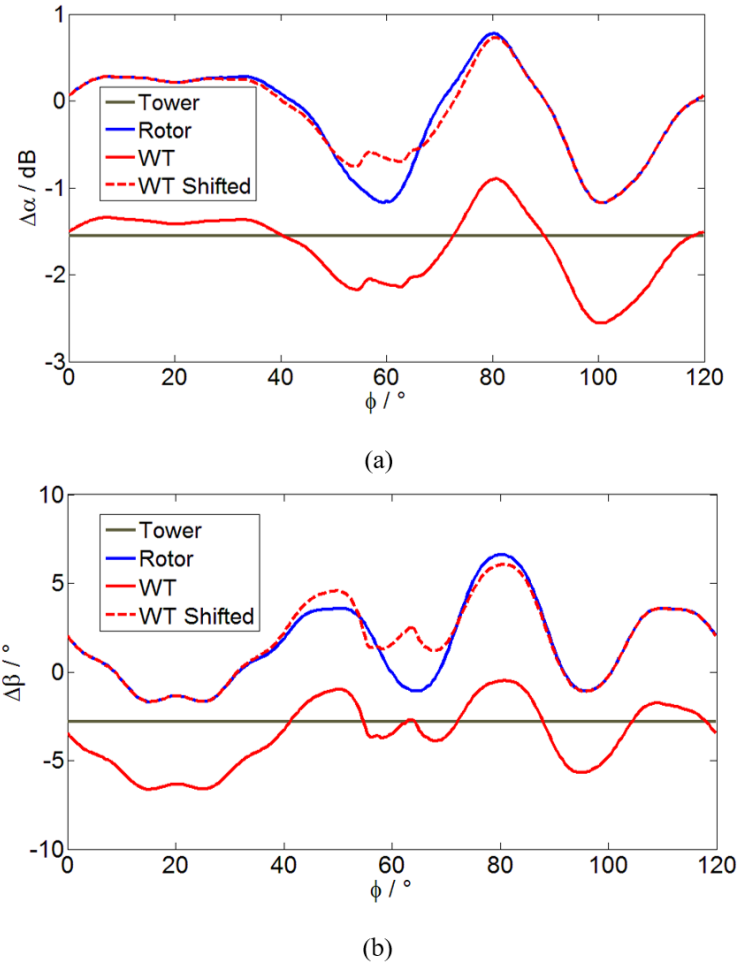

Figure 4-8: Comparison of (a) diffraction loss $\Delta\alpha$ and (b) phase distortion $\Delta\beta$ of individual components of WT vs rotor angle ϕ without ground; $h_{Tx} = h_{Rx} = 68$ m [123]

d_2 =4000 m, l_b = 64 m, w_b = 1.5 m). Fig. 4-8 (a) shows the calculated diffraction loss $\Delta\alpha$ versus rotor angle ϕ for the entire WT structure as well as for the rotor and tower individually. In the considered example, the tower is aligned tangentially inside the 2nd Fresnel zone, producing an obstacle gain of 1.6 dB. The $\Delta\alpha$ curve for the rotor contains one distinct maxima of diffraction loss at ϕ= 80°, where two rotor blades are oriented tangentially inside the 3rd Fresnel zone – as shown in Fig. 4-9 (a). Two significant maxima of diffraction gain are observed at ϕ= 60° with one blade tangential to the 2nd Fresnel zone while being positioned downwards infront of the tower, and at ϕ= 100° with one blade tangentially obstructing the 2nd Fresnel zone as shown in Fig. 4-9 (b). To study the impact of the tower, a copy of the $\Delta\alpha$ curve of the entire WT geometry is shifted upwards by 1.6 dB (shown by the red dotted line in Fig. 4-8 (a)) in order to match it with the $\Delta\alpha$ curve of the rotor at ϕ= 0°. The offset is almost equal to the obstruction gain introduced by the WT tower. The slight difference is subject to the diffraction by the small (time-invariant) overlap between tower and hub as well as subject to a slight phase mismatch of the received fields when considering the scenario of diffraction individually for tower and rotor at ϕ=0°.

For instances, where a rotor blade experiences a significant overlap with the tower ($\phi \approx$ 40°-80°), a notable disagreement between the $\Delta\alpha(\phi)$ curve of rotor and the shifted $\Delta\alpha(\phi)$ curve of the entire WT can be observed. The maximum overlap of tower and rotor occurs at ϕ= 60°. At this rotor angle, the blade positioned downward and overlapping with the tower is aligned tangentially to the 2nd Fresnel zone such that the tangent point lies almost half way down the blade. At this instance, the rotor will produce a maximum of obstruction gain due to the tangential obstruction of an even Fresnel zone. Since the maximum overlap of the rotor and tower occurs at the same instance, the AC component of $\Delta\alpha(\phi)$ for the entire WT geometry will experience the maximum impact of the tower. Consequently, the difference between the the $\Delta\alpha(\phi)$ curve of rotor and the shifted $\Delta\alpha(\phi)$ curve of the entire WT reaches a maximum (around 0.5 dB in the considered example). Other than the offset between $\Delta\alpha(\phi)$ curves for the rotor and the entire WT, the impact of the tower is only noticable during the interval where the overlap between the rotor blades and tower occurs.

Similar trends can be observed for the diffraction induced phase distortion $\Delta\beta(\phi)$, as shown in Fig 4-8 (b). The tower produces a maximum phase

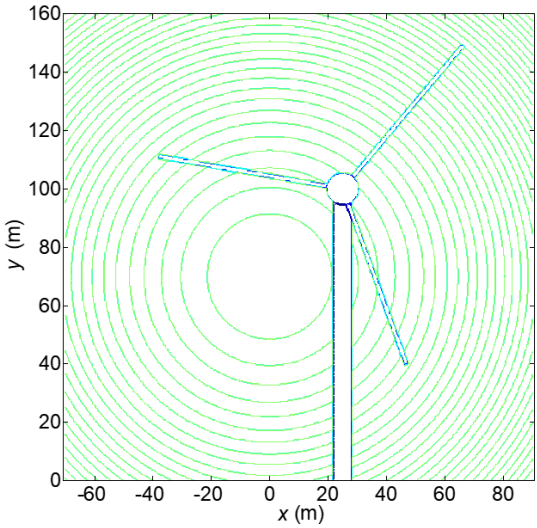

(a)

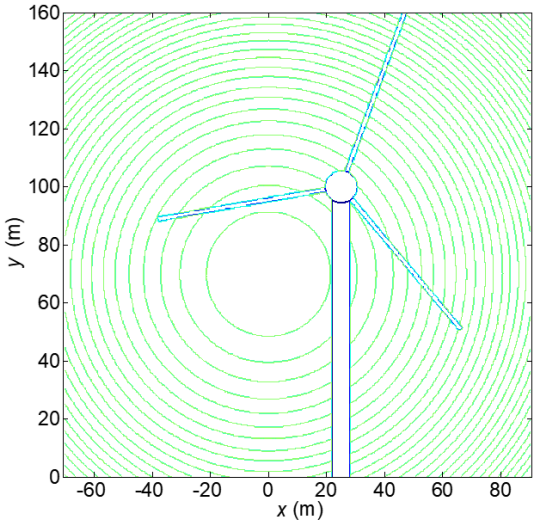

(b)

Figure 4-9: Plane of obstruction: WT (blue) and Fresnel zones (green) for rotor angle (a) ϕ=80° and (b) ϕ=100° [123].

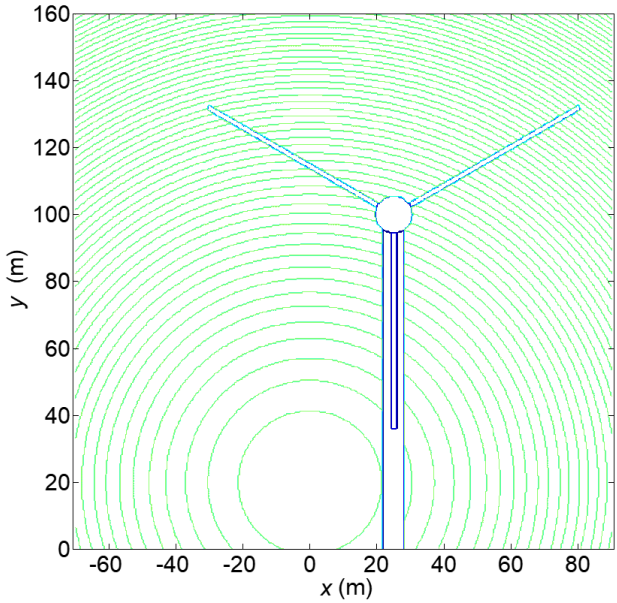

Figure 4-10: Plane of obstruction with WT (blue) and Fresnel zones (green) for rotor angle ϕ=60°; h_{Tx} = h_{Rx} = 68 m (without ground plane) [123]

modulation of almost 3°. A copy of the $\Delta\beta$ curve for the entire WT gemetry is shifted by an offset value close to the value of phase modulation caused by the tower, in order to match it with the $\Delta\beta$ curve of the rotor at ϕ= 0°. Maxima of $\Delta\beta(\phi)$ occur for rotor angles where a blade is oriented at the outer boundary of an odd Fresnel zone (e.g. maxima observed at ϕ= 78°, one blade on the outer boundary of the third Fresnel zone). Minima of $\Delta\beta(\phi)$ occur where a blade is oriented at the outer boundary of an even Fresnel zone (e.g. minima at ϕ =95°, one blade at the outer boundary of the second Fresnel zone). Again, the impact of the tower on $\Delta\beta(\phi)$ is only visible where there is an overlap between blades and tower (ϕ ≈40°-80°).

For further investigation, a second scenario is considered simply by reducing the antenna heights to h_{Tx} = h_{Rx} = 20 m, while all other parameters are kept constant (same as for Fig. 4-8). The corresponding plane of obstruction for ϕ= 60° is shown in Fig. 4-10. In this scenario, during the maximum

overlap between a rotor blade and the tower, the blade is not tangentially aligned within a Fresnel zone.This produces only a minor impact of the tower on the $\Delta\alpha$ curve of the entire WT (Fig. 4-11).

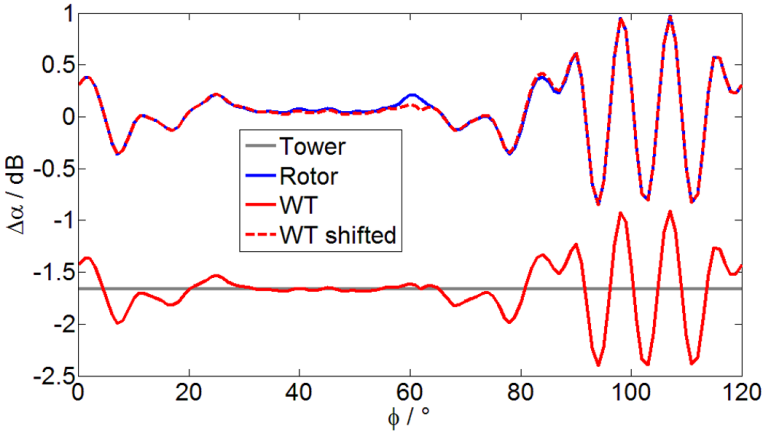

Figure 4-11: Comparison of diffraction loss $\Delta\alpha$ of individual components of WT vs rotor angle ϕ without ground; $h_{\mathrm{Tx}} = h_{\mathrm{Rx}} = 20$ m [123]

4.3 Impact of illuminated Ground Plane

The analysis is now extended in a consistent way to explain the impact of an illuminated ground plane [124]. Before delving into the details, it is important to make some observations about the calculation set up of time variant pattern of amplitude distortion caused by the WT. Fig. 4-12 (a) shows the plane of obstruction for a case where the ground reflected paths are ignored and the only obstruction in the aperture is caused by the WT. This holds true if

a) No considerable field exists in the plane of obstruction for $y < 0$.

b) All ground reflected paths between Tx and Rx can be neglected.

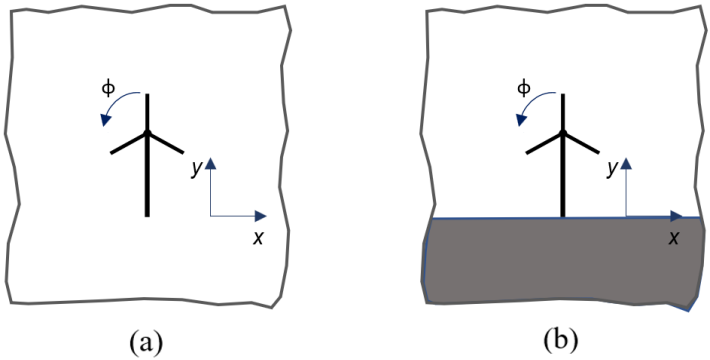

Figure 4-12: WT plane of obstruction (a) without and (b) with ground plane [124]

The first condition is easily fulfilled for applications using narrow beam antennas (e.g. weather radar) and hence the obstructing half plane below the WT displayed in Fig. 4-12 (b) can be ignored. The second condition requires that the field contributions from all ground reflected paths is negligible compared to the contribution of the LOS path. This requirement is difficult to satisfy especially at low elevation of the transmit and receive antennas over ground since the signal emanating from the image transmitter and the signal received by the image receiver will have significant levels. To investigate the impact of ground plane reflections on the WT forward scatter, two factors need to be considered. Firstly, the diffraction caused by the ground plane in the plane of obstruction (which acts as an obstructing half plane as displayed in Fig. 4-12 (b)) and secondly, the signal contributions from all ground reflected paths. The first factor will only introduce an offset in the $\Delta\alpha(\phi)$ and $\Delta\beta(\phi)$ curves, since there is no rotor angle ϕ dependant overlap between the WT and the obstructing half plane underneath it. The part of the aperture lying below the ground at $y< 0$ makes no contribution to the overall received field.

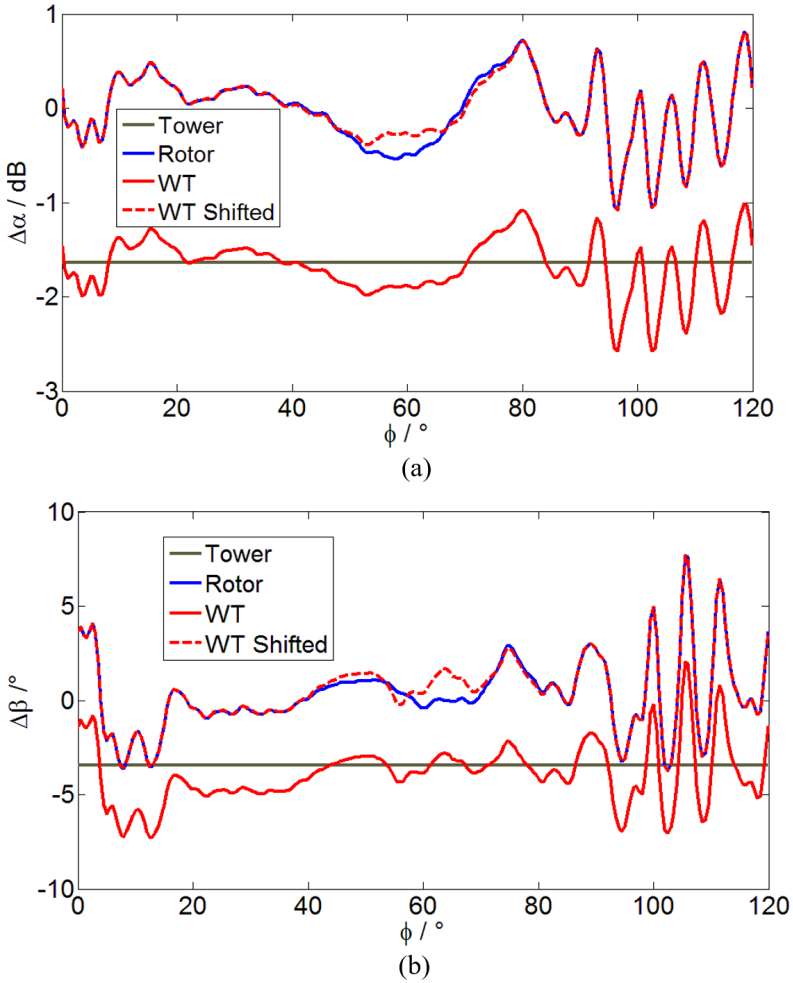

Figure 4-13: Comparison of (a) diffraction loss $\Delta\alpha$ and (b) phase distortion $\Delta\beta$ of individual components of WT vs rotor angle ϕ with ground; $h_{Tx} = h_{Rx} = 68$ m [124]

To illustrate the impact of ground reflections, a PEC ground plane is now considered for the scenario presented in section 4.2 (Fig. 4-8). The polarization is assumed to be vertical. The corresponding curves for $\Delta\alpha$ and

$\Delta\beta$ versus rotor angle ϕ are shown in Fig. 4-13. The values of obstruction gain and phase modulation caused by the tower are the same as in the previous section ($\Delta\alpha$= -1.6 dB, and $\Delta\beta \approx 3°$). However, more maxima and minima (with moderately higher amplitudes) are noticable for the $\Delta\alpha(\phi)$ and $\Delta\beta(\phi)$ curves for the rotor and the entire WT. For the considered link setting, a constructive interference between the LOS path and the ground reflected path is produced in the absence of the WT. For geometries where without WT there is an almost destructive interference between LOS path and ground reflected path significantly higher amplitude of $\Delta\alpha(\phi)$ can arise.

Fig. 4-14 displays the relative amplitude and phase of the total field at the receiver along with the individual signal contributions of the four paths Tx–Rx, Tx–Rx, Tx–Rx and Tx–Rx. As Fig. 4-14 shows the relative amplitude of the received field instead of the diffraction loss, the displayed field contribution due to the Tx-Rx path is essentially a mirrored and shifted version of the $\Delta\alpha(\phi)$ plot in Fig. 4-8 where no ground plane was considered. It is interesting to note that the difference between the field at the receiver due to only the path Tx–Rx for the cases with and without the ground plane is equal to the offset caused by the obstructing half plane underneath the WT in the plane of obstruction (5.7 dB in this case). Also, the curve for the total received field amplitude versus rotor angle in Fig. 4-14(a) is also a mirrored and shifted version of the diffraction loss curve in Fig. 4-13. Due to the symmetry (h_{Tx}= h_{Rx} and d_1= d_2) in the considered scenario, the relative amplitude and phase contributions by the paths Tx–Rx and Tx–Rx are identical (Fig. 4-14 (a) and (b)). It can also be seen that these components are almost in phase with the Tx–Rx component, resulting in a constructive interference scenario with the relative amplitude of the overall field greater than each of the individual components. In the Fig. 4-14, distinct maxima and minima are observed in the relative amplitude and phase curves for the paths Tx–Rx and Tx–Rx during the interval $\phi \approx$ 80°-130° (curves repeat themselves after 120°). Due to the superposition of the signal contributions from all four paths, these maxima and minima are also present in the amplitude and phase curves of the total received field (Fig. 4-14) as well as in the $\Delta\alpha(\phi)$ and $\Delta\beta(\phi)$ plots (Fig. 4-13). It is interesting to note that the signal level of the contributions from these two paths are closer to that of the LOS path Tx–Rx. Consequently the extrema in the individual contributions from these paths are clearly visible in the curves for the overall field due to all four paths as well as the $\Delta\alpha(\phi)$ and

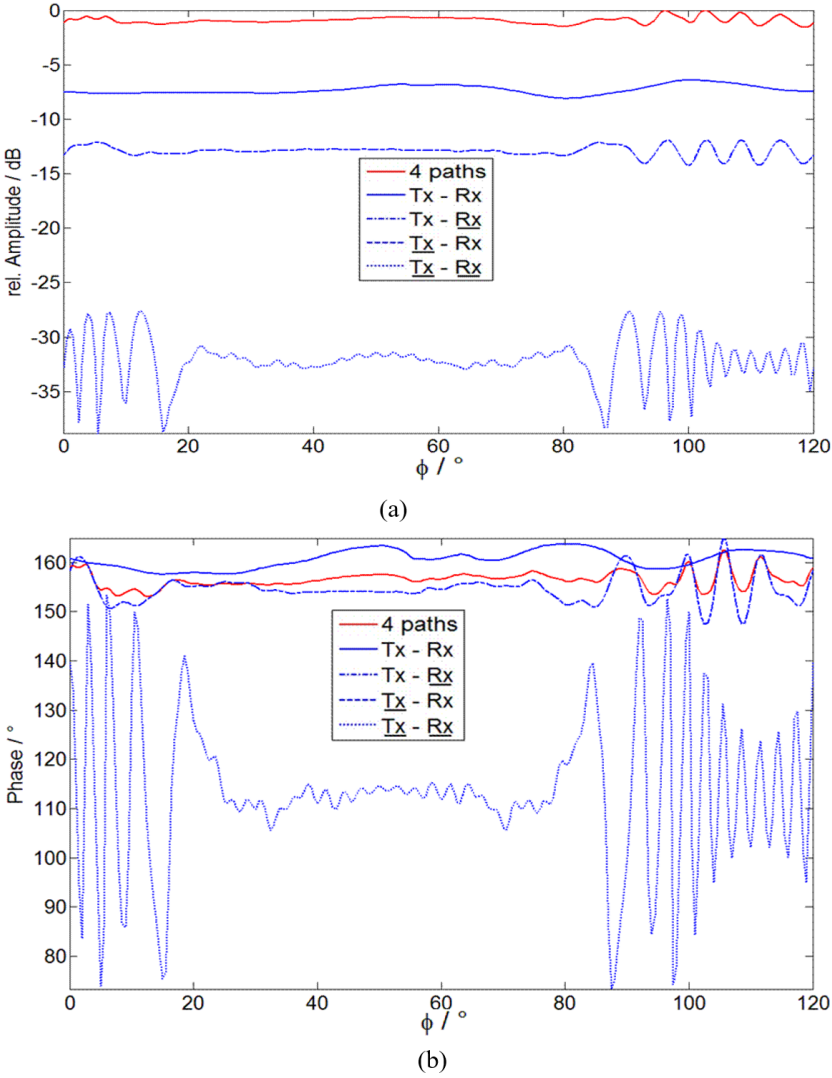

Figure 4-14: Point-to-point link obstructed by WT on PEC ground. Total received field and contribution of the four paths Tx–Rx, Tx–Rx, Tx–Rx and Tx–Rx vs rotor angle ϕ: (a) relative amplitude and (b) phase [124].

$\Delta\beta(\phi)$ plots. The extrema can be explained by investigating the obstruction of the Fresnel zones by the rotor blades for each path. Consider the maximum of diffraction loss observed at ϕ=119° originating from the paths Tx–Rx and Tx–Rx. Fig(a) shows the corresponding orientation of the rotor blades along the Fresnel zones for the path Tx–Rx. The same figure can be used to explain the Fresnel zone obstruction for the path Tx–Rx since the field contributions from the two paths is identical due to the symmetry in the considered scenario. It can be seen that a rotor blade is oriented tangentially along an odd (21st) Fresnel zone, thus producing a maximum of diffraction loss. Similarly, Maxima of obstruction loss can be attributed to blade orientations tangentially within an even Fresnel zone related to the respective path.

For the considered example, the path Tx–Rx has the smallest contribution to the overall field. This is mainly because of the high elevation of the transmit and receive antennas, which causes the image transmitter and the image receiver to be located at the same level underneath the ground. Due to the impact of the obstructing half plane below the WT (Fig 4-12(b)), the corresponding signal contribution is about 20 dB lower than that of the paths Tx–Rx and Tx–Rx and about 30 dB lower than the signal contribution from the LOS path Tx–Rx (Fig. 4-14(a)). Thus, the impact on the overall signal at the receciver is almost negligible.

Another important aspect is the frequency modulation associated with each of the four paths. This is determined by the order of the obstructed Fresnel zones. The higher order Fresnel zones are narrower than the lower order ones and are thus traversed faster by the rotor blades, due to which higher order frequency components of $\Delta\alpha$ and $\Delta\beta$ are produced. Therefore, while the path with no ground reflection (Tx–Rx) has a higher signal amplitude, it contains low frequency modulation components due to the obstruction of lower order Fresnel zones (Fig. 4-14). Similarly, the path with double ground reflection (Tx–Rx) has the highest frequency modulation components due to the obstruction of higher order Fresnel zones. Consider the maximum of diffraction loss at ϕ=16°. Fig. 4-15(b) shows the corresponding orientation of the rotor blades along the Fresnel zones for the path Tx–Rx. It can be seen that a rotor blade is partially obstructing an odd (the 61st) Fresnel zone at ϕ=16°. Though a single blade can only obstruct a small part of a Fresnel zone the difference between maximum

and minimum value of the curve for the received signal for the path Tx–Rx can be more than 10 dB. The reason for this is that only the contribution of higher order Fresnel zones add to the received signal. This signal while small in total, is the sum of many destructively interfering Fresnel zones. Even a partial obstruction of one such contributing zone can have a significant impact on the overall sum of all interfering signals.

4.4 Summary and Notes

An in-depth analysis of the WT forward scatter has been presented, by using 2D Fresnel-Kirchhoff diffraction approach. The patterns of $\Delta\alpha(\phi)$ and $\Delta\beta(\phi)$ have been explained in terms of the obstructed Fresnel zones. For a WT rotor, when a significant (or a small but odd) number of Fresnel zones are illuminated, if a single blade is tangentially oriented with respect to the illuminated Fresnel zones while the width of the blade w_b is small compared to the width of the obstructed zone, general conclusions about the impact of diffraction can be drawn as follows: Maxima (minima) of diffraction loss $\Delta\alpha$ occur for blade orientations tangentially inside an odd (even) Fresnel zone, maxima (minima) of diffraction induced phase shift $\Delta\beta$ occur for blade orientations at the outer boundary of an odd (even) Fresnel zone. The strongest impact of WT rotor diffraction is observed for rotor angles when two blades are aligned almost tangential to the illuminated Fresnel zones. During these intervals of ϕ, the third blade is almost perpendicular to the Fresnel zones and has negligible contribution to the overall signal modulation. The phase of the respective shaded fields of the two blades tangentailly obstructing the Fresnel zones depends on the offset of the LOS path from the rotor axis. The mechanical coupling between the two blades is such that when one of the two tangentially oriented blades moves towards the LOS path, the other moves away from it. This causes the phase of their respective shaded fields to change rapidly in opposite directions during the rotation of the WT rotor. Thus, the overall impact strongly depends on the offset of the LOS path from the rotor axis.

General conclusions can also be drawn about the interaction of the WT rotor and tower in the context of forward scattering. For the DC com-

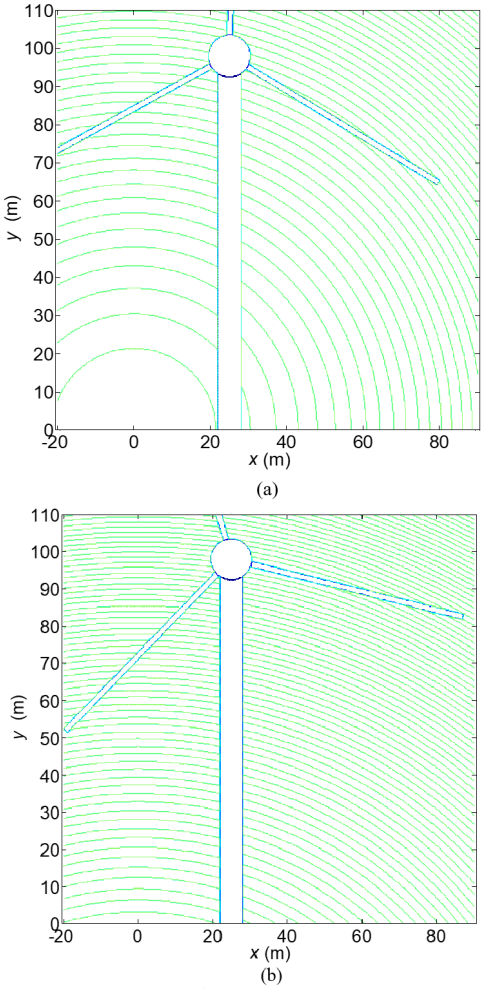

Figure 4-15: Plane of obstruction: WT (blue) and Fresnel zones (green) for rotor angle (a) ϕ=119° (path Tx–Rx) and (b) ϕ=16° (path Tx–Rx) [124]

ponent of the diffraction loss of the whole WT, the tower introduces an offset almost equal to the diffraction loss caused by the tower itself. A small difference is caused by the slight overlap between the tower and hub. The time-variant overlap between the tower and rotor blades produces a change in the AC component of $\Delta\alpha$ around $\phi = 60°$. A significant impact in this regard is observed only if the tower is oriented tangentially within a Fresnel zone or obstructs the LOS path at about $1/\sqrt{2}$ times the radius of the 1st Fresnel zone. Similar trends are observed for the diffraction induced phase modulation $\Delta\beta$.

An analytical insight into the forward scatter patterns of a WT in the presence of an illuminated ground plane has been presented by inspecting the obstruction of the Fresnel zones of the LOS path Tx–Rx as well as the ground reflected paths Tx–Rx, Tx–Rx, and Tx–Rx. Typically, the path without ground reflection (Tx–Rx) has a higher signal amplitude (low diffraction loss due to ground, smaller diffraction angles) and lower modulation frequency components. Paths including a single ground reflection (Tx–Rx and Tx–Rx) have smaller signal amplitudes and higher modulation frequency components, while the path including double ground reflection (Tx–Rx) has very small signal amplitudes but the highest modulation frequency components due to the obstruction of higher order Fresnel zones.

The comprehensive understanding presented here allows for targeting worst case scenarios while avoiding time consuming brute-force methods. The following chapter explores the performance of radar and radio communications under conditions of strong impact of WT forward as highlighted in this chapter.

5 Application to Radar and Radio Links

After developing an analytical and qualitative understanding of WT forward scatter, the focus is now shifted towards studying its impact on operational radar and radio communication links. Using the concepts developed in the preceding discussion, some practical scenarios of radar and communication systems under the influence of WTI are studied in this chapter. The discussion presented aims to further verify the concepts developed in the previous chapters and in the process intends to identify the crucial aspects of wind turbine forward scatter along with vital figures of merit. This is of particular interest when it comes to finding the worst-case scenario within given boundaries for a large set of parameters.

First, the impact of the diffraction induced amplitude and phase modulation caused by the WT forward scatter on the performance of a fixed radio link using a higher order modulation is considered. The 2D Fresnel-Kirchhoff diffraction model is used to analyze the quality of the received signal of a 16-QAM system by calculating the Bit Error Rate (BER) and Modulation Error Ratio (MER) of raw data with and without WT rotor. A PEC ground plane is considered to illustrate the role played by the ground plane reflections. The periodic amplitude and phase modulation caused by the rotating WT blades, along with white Gaussian noise (AWGN) is used to characterise the time-variant channel. The impact of signal scattering from objects other the WT rotor and ground plane is ignored. Imperative conditions for scenarios with a significant impact of WT forward scatter are outlined. The focus is then shifted towards radar systems by studying the impact of an offshore WT on the error in measurement of radial speed by an S band marine radar of a large cargo vessel. In addition to the impact

of quasi-static amplitude and phase modulation, instantaneous Doppler deviation and time-frequency spectrum using short-time Fourier transform (STFT) are taken into account. A flat earth approximation is used for this investigation, which while not accurate even for the assumption of low sea state, provides an adequate insight into the impact of WT forward scatter on the radar output.

5.1 Higher Order Modulation Systems

Investigations about WTI effects on fixed communication links have mostly focused on analogue television systems. The performance of different digital transmission schemes under WTI is yet to be comprehensively assessed [37]. In this section, phase and amplitude modulation caused by WT forward scatter has been used to define the time varying channel characteristics to analyze the performance of a 16 QAM system under WTI. Other modulation schemes can also be investigated using the same apporach. Early digital communication systems represented digital signal quality based only on the BER of the received signal, measured before the application of any error correction algorithm (like FEC or Viterbi). This so-called pre-Viterbi BER gives a good indication of how hard the error correction algorithm must work in order to maintain an acceptable quality of signal transmission [120]. More recent trends have shown the use of MER, which is the ratio of the average symbol power to the average error power [119]. In effect, MER compares the actual location of a received symbol to its desired location. As the signal degrades, the received symbols are located further from their ideal locations and the measured MER value will decrease.

The channel model used in this section to study the impact of WT rotor forward scattering on the MER and BER of raw data of a 16-QAM system is shown in Fig. 5-1 [121]. The signal $x(t)$ undergoes modulation and up-conversion before being sent out by transmitted (Tx) towards the receiver (Rx). In addition to AWGN, this RF signal encounters the periodic amplitude and phase distortion caused by the WT rotor, represented by the function $c(\phi)$, which can be represented as given below

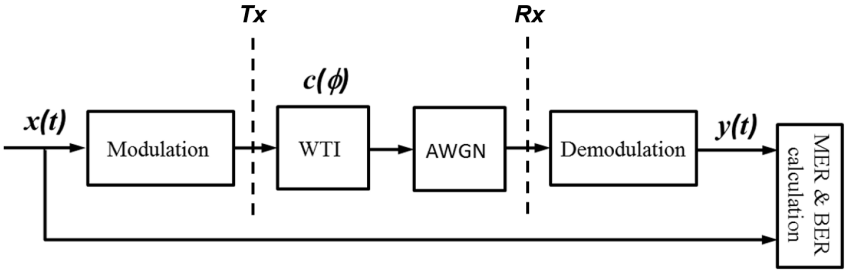

Figure 5-1: Channel model used for BER calculation of 16-QAM system with wind turbine interference (WTI) und additive white Gaussian noise (AWGN) [121]

$$c(\phi) = \Delta\alpha(\phi)e^{j\Delta\beta(\phi)} \tag{5.1}$$

At the receive terminal, the signal is down converted followed by demodulation. A comparison of the demodulated signal $y(t)$ with $x(t)$ is used to calculate the MER and BER of the raw data. It is assumed that the spectrum of the diffraction induced amplitude and phase modulation lies above the crossover frequency of the amplitude and phase control loops of the receiver and will remain unaffected by filtering at the receiver. For narrowband RF signals, the 2D Fresnel-Kirchhoff diffraction model can be used to calculate the function $c(\phi)$ for the carrier frequency ω_o. Once the function $c(\phi)$ has been determined for the carrier frequency ω_o, the up and down conversion of the signal does not need to be considered any further. The Fresnel-Kirchhoff diffraction formula involves approximations (in particular $r_1, r_2 >> \lambda$) that limit the frequency range at the lower end and, thus, do not allow to calculate the (time-variant) impulse response of the channel. For the same reason, a time-domain representation of the Fresnel-Kirchhoff integral formula cannot be derived. Besides these limitations, another difficulty is presented by the the phase shift factor $j{=}e^{\frac{j\pi}{2}}$. Therefore, only frequency domain approach is considered in the investigation presented in this section. Moreover, a flat narrowband channel is assumed and the function $c(\phi)$ remains constant.

For the investigation, the tower of the WT is ignored as the interest lies pri-

marily on the impact of the rotating blades. The scenarios considered have been simulated using MATLAB. In the first scenario, the ground plane is assumed to be non-illuminated. The LOS path is positioned to be collinear 90 m below and 90 m to the right (as viewed from Tx) of the rotor axis. This setting results in a link clearance of over 2 Fresnel zones. Rest of the link parameters are same as considered in examples of sections 4.1 and 4.2 (f=1.3 GHz, d_1=d_2=4000 m, l_b=64 m, w_b=1.5 m). All the results have been verified by comparison with FEKO UTD simulations [121]. The calculated $\Delta\alpha(\phi)$ and $\Delta\beta(\phi)$ curves are shown in Figure 5-2 . For simplification, an isotropic antenna pattern has been considered. As expected, the maxima of the curve for $\Delta\alpha(\phi)$ occur for rotor angles where a blade is oriented tangentially within an odd Fresnel zone, while the minima occur for blade orientations tangentially within an even Fresnel zone. The maximum diffraction loss for this case is almost 0.5 dB, whereas the maximum obstruction gain is around 0.7 dB. The phase modulation lies in the range of almost -3.5° to +3.3°. A Pseudo Random Bit Sequence (PRBS 2^{16}-1) using Gray code mapping is used to calculate the corresponding instantaneous modulation error ratio (MER) (displayed in Fig 5-2 (c)) with an assumed SNR=∞. As expected, a significant drop in the values of instantaneous MER occurs for the interval ($\phi \approx$ 50°-100°) where significant values of $\Delta\alpha$ and $\Delta\beta$ are observed. The MER value decreases to about 25 dB in the said interval, while the average value of MER (over ϕ=0°-120°) is 33.4 dB. This level is still high enough for the link to remain error free (BER=0 for all values of ϕ). Thus, in the absence of an illuminated ground plane, a link clearance of over 2 Fresnel zones can be assumed to maintain a satisfactory link performance.

The investigation is then taken forward by considering the ground plane effects. In this regard, two different cases are taken into account. First, a perfect ground plane is assumed to be 100 m below the rotor axis, thus making the height of the transmit and receive antennas to be 10 m. All parameters are kept the same as used for the example considered before. The polarization of the signal is taken to be vertical. In the absence of WT, a constructive interference of LOS path and ground reflected path occurs for this case. Next, the heights of Tx and Rx are increased to 20 m, which results in an almost destructive interference of LOS path and ground reflected path without the WT. In the discussion that follows, the scenario with constructive interference of the two paths will be referred to as case (I), whereas the destructive interference scenario will be called

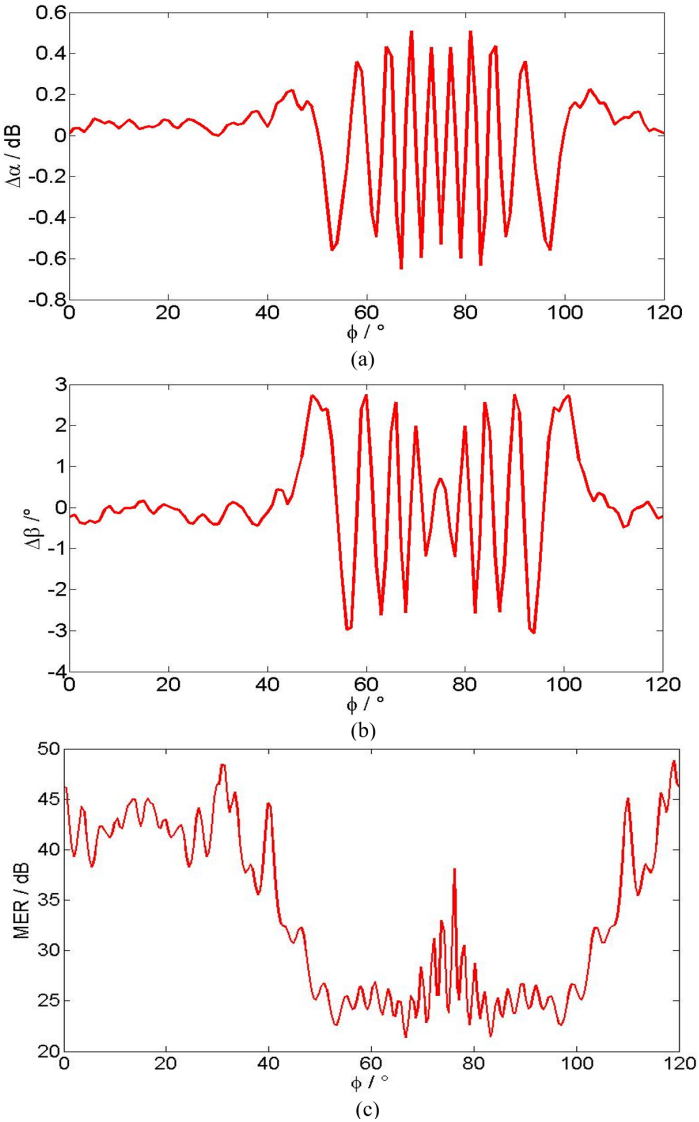

Figure 5-2: Simulated (a) diffraction loss $\Delta\alpha$ (b) phase distortion $\Delta\beta$ and (c) corresponding instantaneous MER vs rotor angle ϕ ; no ground plane, SNR=∞ [121]

case (II). The link clearance of over 2 Fresnel zones is maintained for all four paths in both case (I) and case (II). The corresponding curves for $\Delta\alpha$, $\Delta\beta$ and instantaneous MER vs rotor angle ϕ for case (I) are shown in Fig. 5-3 (a), (b) and (c) respectively. It can be observed that for this case, the maximum values of diffraction loss and diffraction gain are only slightly higher than those without the ground plane (in Fig. 5-2). Accordingly, the decrease in the value of instantaneous MER is only slightly more than in the case without ground plane. The average value of MER is 30.9 dB which is only slightly lower than in the case without ground plane. Consequently, the link remains error free (BER=0).

Figure 5-4 (a),(b) and (c) displays the corresponding curves for $\Delta\alpha$, $\Delta\beta$ and instantaneous MER vs rotor angle ϕ for case (II). Significantly higher values of maximum diffraction loss (5.2 dB) and maximum obstruction gain (3.3 dB) are observed as compared to those of case (I) or the case without ground plane. As expected, this causes the corresponding minimum value of instantaneous MER to be considerably lower than both the previous cases. The average value of MER decreases to 21.3 dB. Fig. 5-5 (a) shows the corresponding BER for case (II) and it can be observed that the link is no longer error free. The minimum required value of MER for a bearable BER of 10^{-6} for a 16-QAM modulation system is 21 dB. Burst errors are observed for rotor angles where the MER value drops below the desired minimum level of 21 dB. Fig. 5-5 (b) displays the corresponding constellation diagram (scatter plot). The impact of the distortion caused by amplitude and phase modulation by the WT rotor can clearly be seen. It is interesting to note, that even though a link clearance of over 2 Fresnel zones is maintained for all four paths, a setup with strong destructive interference between the LOS path and the ground reflected path is susceptible to amplitude and phase distortions caused by the WT rotor.

The above observation is further emphasised by considering Gaussian noise in the channel. Fig. 5-6 shows a plot of the maximum and average values of BER (BER_{max} and BER_{avg} respectively) for cases (I) and (II) over the interval ϕ= 0-120°. It can be seen that the low BER values are obtained for case (I), whereas significantly high raw data BER values arise for case (II) due to unacceptably low values of the corresponding instantaneous MER. It can be concluded that even with a significant clearance (over 2 Fresnel zones in the considered scenario) a link setup with strong destructive

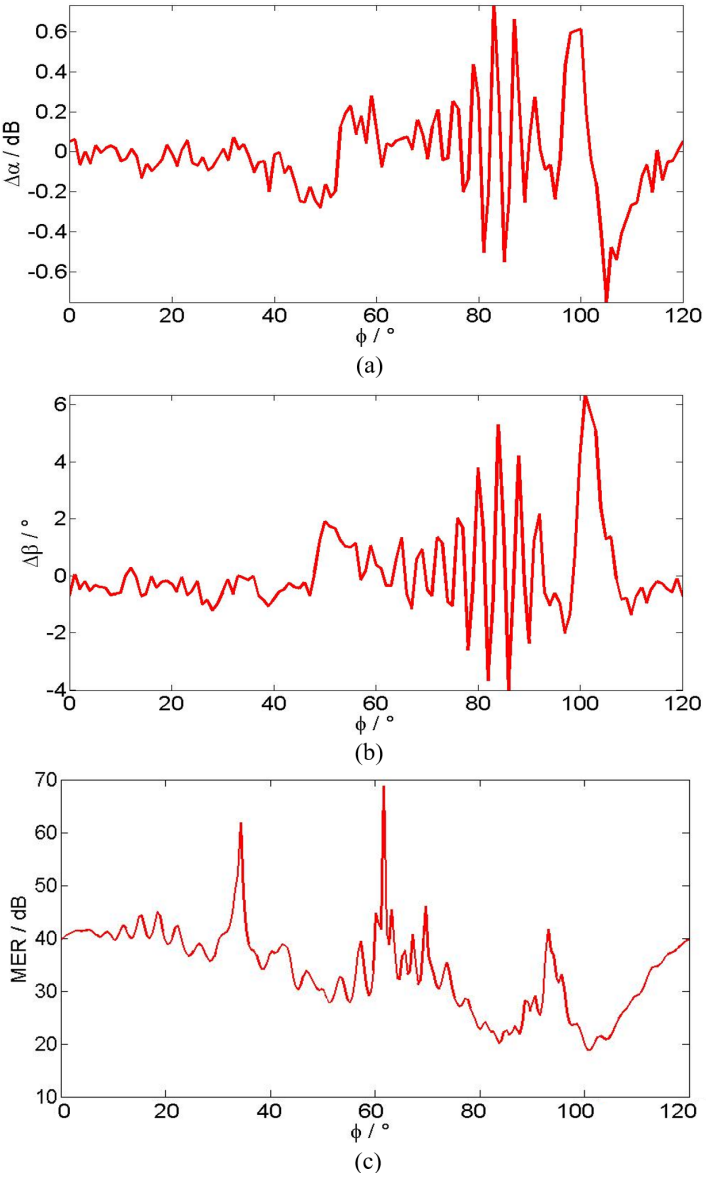

Figure 5-3: Simulated (a) $\Delta\alpha$ (b) $\Delta\beta$ and (c) corresponding instantaneous MER vs rotor angle ϕ ; PEC ground plane (vert. pol), SNR=∞, case (I) [121]

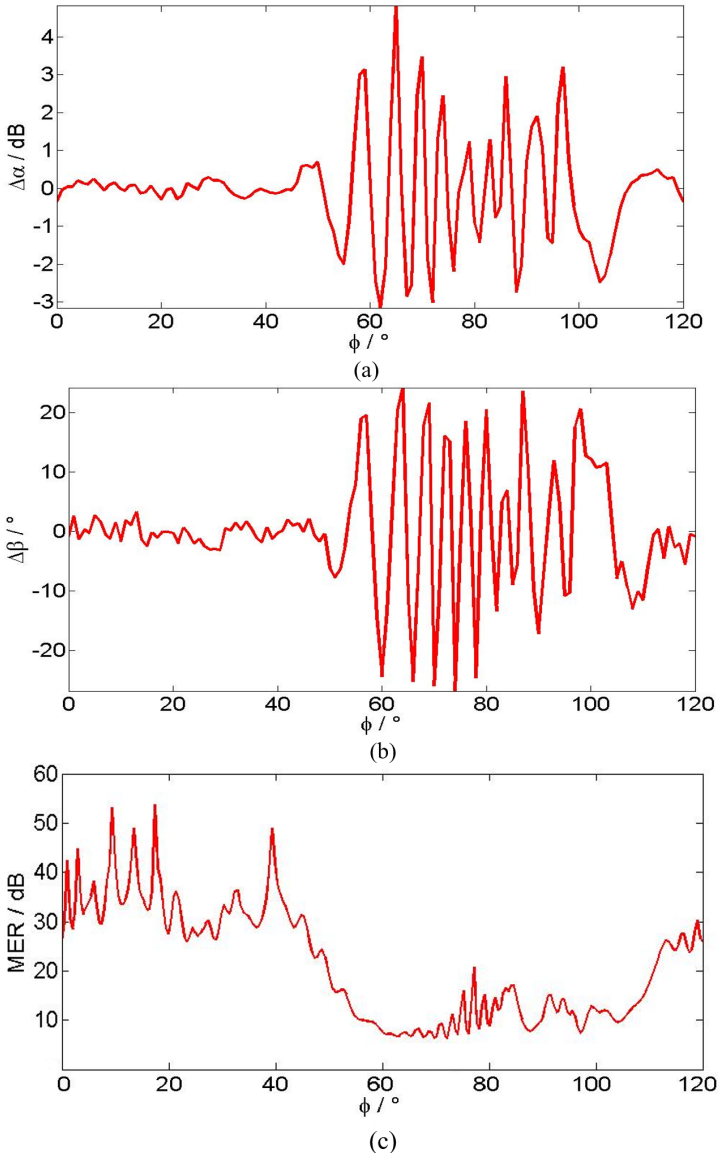

Figure 5-4: Simulated (a) $\Delta\alpha$ (b) $\Delta\beta$ and (c) corresponding instantaneous MER vs rotor angle ϕ ; PEC ground plane (vert. pol), SNR=∞, case (II) [121]

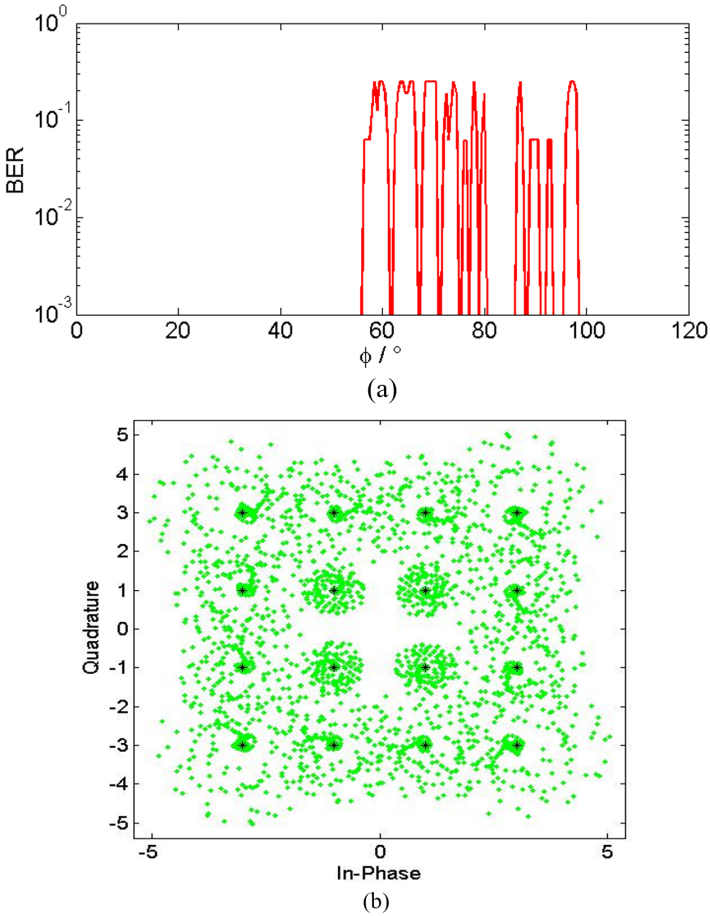

Figure 5-5: Simulated (a) BER and (b) constellation diagram for a whole rotation, PEC ground, SNR=∞, case (II) [121]

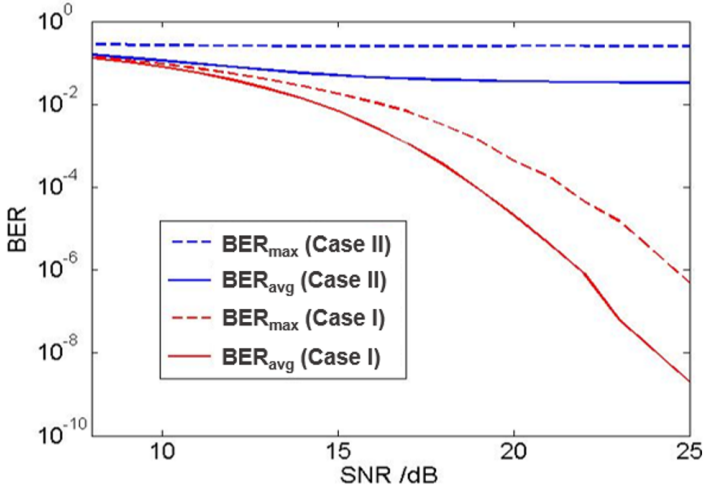

Figure 5-6: Simulated average and maximum BER vs SNR with added AGWN for case (I) and (II) [121].

interfering ground reflected path is very sensitive to amplitude and phase distortions caused by the rotor.

5.2 Radar Systems

An important aspect of WT forward scatter is the frequency deviation associated with the phase and amplitude modulation induced by the rotating blades which in radar applications will become apparent as an error in the measured Doppler spectrum. This frequency shift presents a vital figure of merit for the analysis of WT interference to radar systems, especially those dealing with low Doppler frequencies (e.g. weather radars).

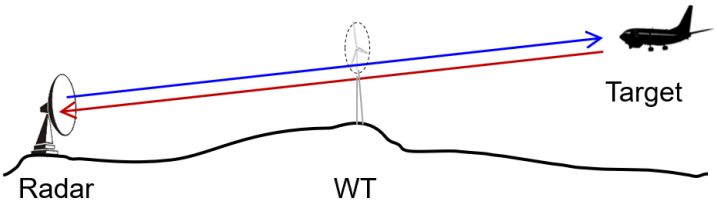

Figure 5-7: Forward Scattering - Radar signal obstructed by WT.

For a radar system, the 2D Fresnel-Kirchhoff diffraction model of section 3.3 (and the subsequent concepts developed in the preceding chapters) can be applied simply by replacing the receiver (Rx) with target (T). The signal is diffracted twice at the rotating blades, once along the forward path (radar-target, blue line in Fig. 5-7) and then along the return path (target-radar, red line in Fig. 5-7). Since the phase velocity of the electromagnetic waves is significantly higher compared to the WT rotor speed, it can be assumed for an isotropic point scatterer that the signal on both the forward and return paths will experience an identical modulation in case of a monostatic radar. The one-way diffraction loss and phase shift calculated can thus be multiplied by a factor of 2 to account for the round trip. The instantaneous frequency deviation Δf_D of the two-way signal can be calculated by performing a derivation of the diffraction induced two-way phase shift $\Delta\beta$ with respect to time as given below

$$\Delta f_D = \frac{1}{2\pi}\frac{\partial \Delta\beta}{\partial t} \tag{5.2}$$

The instantaneous temporal Doppler shift of a target is evaluated by a radar system while determining the respective Doppler spectrum. This spectrum can be obtained by performing a short time Fourier transform (STFT) of the modulating time signal $m(t)$=$\Delta\alpha$(t)$e^{j\Delta\beta(t)}$, which is essentially the modulation function $c(\phi)$ (used in section 5.1) represented in the time domain instead of the rotor angle ϕ domain.

In the following, a marine radar fitted on a large cargo vessel is considered and the impact of an offshore WT on the error in measurement of radial speed is investigated. Large cargo vessels generally contain an X band

radar which provides a higher resolution, along with an S band radar which is less prone to rain and fog effects. Errors in the estimations of the radial speed of a vessel can seriously deteriorate the performance of onboard automatic collision avoidance systems (ACAS) [37].

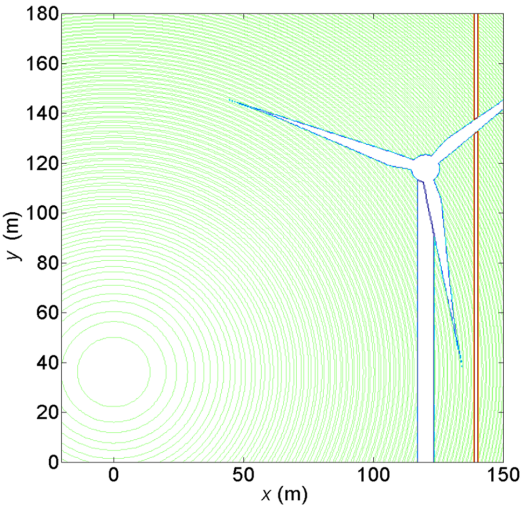

Figure 5-8: Plane of obstruction (view from Tx): WT with rotor angle ϕ=70° (blue), Fresnel zones of direct path Tx-T (green) and half power beamwidth (red); S band radar [127].

As the error in measured radial speed due to rotor forward scatter is higher for lower frequencies (discussed in section 6.1), the S band radar can be expected to have a higher impact of rotor forward scattering on the error in measured radial speed as compared to the X band radar. Thus, in the following discussion, a cargo vessel with an S band radar (f = 3.0 GHz) is considered. The radar is considered to be installed at a height of 59 m above sea level [127]. A sailing vessel is assumed to be fitted with a radar reflector at its mast (point target) mounted at a height of 13.4 m above sea level. The polarization of the radar signals is taken to be horizontal, which is typical for a marine radar. The -3dB beamwidths are assumed to be 2° and 30° in horizontal and vertical directions respectively. The disired beam profile is obtained by using Chebyshev weighting using a side lobe level

of below 30 dB. The properties of the sea water are defined by permittivity ϵ_r=81 and conductivity σ=5 S/m. The WT geometry considered is based on a Vestas V164-8.0 turbine, generally regarded as the largest offshore turbine available with a rotor blade length l_b = 82 m. The distance between radar and plane of obstruction (WT) is d_1 = 4000 m and the distance between plane of obstruction and target is d_2 = 4000 m. The rotor axis is located at a height of 118 m above sea level, assumed to be parallel with the radar line-of-sight (LOS) path Tx-T, with a lateral offset x_{off} = 120 m. Figure 5-8 displays the plane of obstruction for the considered scenario with the WT orientation corresponding to a rotor angle of ϕ= 70°.

Fig. 5-10 displays the relative amplitude and phase of the total received field along with the individual signal contributions of the four paths Tx–T, Tx–T, Tx–T and Tx–T as a function of rotor angle ϕ. In contrast to the scenario considered in section (4.3), the symmetry due to the same heights of the Tx and Rx (T in this case) does not exist in the current example since radar transmitter height and the target height are not the same. Thus, the the curves for the components originating from the paths Tx–T and Tx–T are not identical. Without WT this setting results in a scenario with almost destructive interference (phase difference 189° in Fig. 5-10 b)) of the LOS path (Tx-T) and the ground reflected path Tx–T [127]. In a scenario with destructive interference, small changes in phase difference of one path due to time-variant WT forward scattering can have a significant impact on the amplitude and phase of the overall signal. In the scenario under investigation, the remaining two ground reflected paths Tx–T and Tx–T experience a strong diffraction loss at the sea surface in the plane of obstruction and thus have minor contributions to the overall signal. However, a strong impact of rotor forward scattering on the measured Doppler error can be expected due to the almost destructive interference of the Tx-T and Tx–T paths. From Fig. 5-10 (a) is can be seen that the field on target is about 18 dB lower than the field due to the LOS path Tx-T. The impact of rotor forward scattering is most significant when two blades are about tangential to the Fresnel zones ($\phi \approx$ 55°-75°).

Next, both the cargo and sailing vessels are assumed to be moving parallel to the plane of obstruction with the same speed, which causes the lateral offset x_{off} of the LOS path with respect to the rotor axis in the plane of obstruction to vary. Figure 5-10 shows the diffraction loss $\Delta\alpha$ as a function

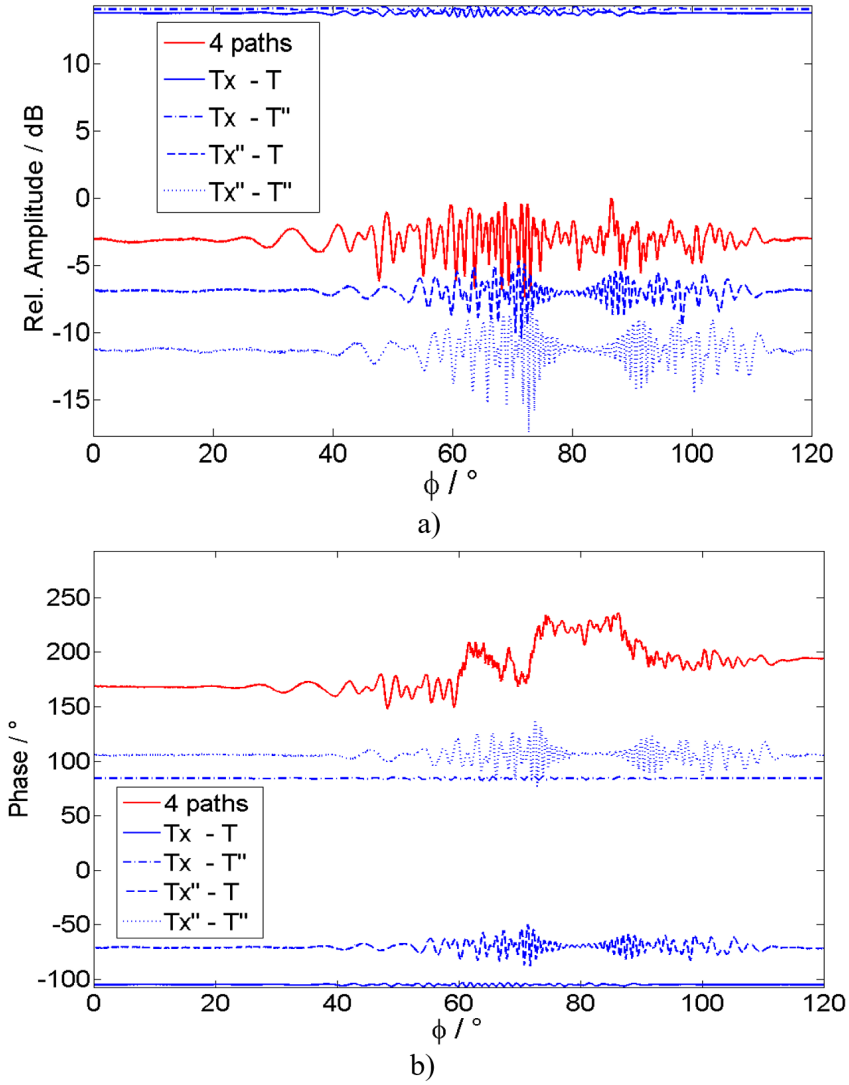

Figure 5-9: Forward scattering of S band radar signal: Field on target and contribution of the individual paths Tx–T, Tx–T, Tx–T and Tx–T: (a) relative amplitude and (b) phase vs rotor angle ϕ [127].

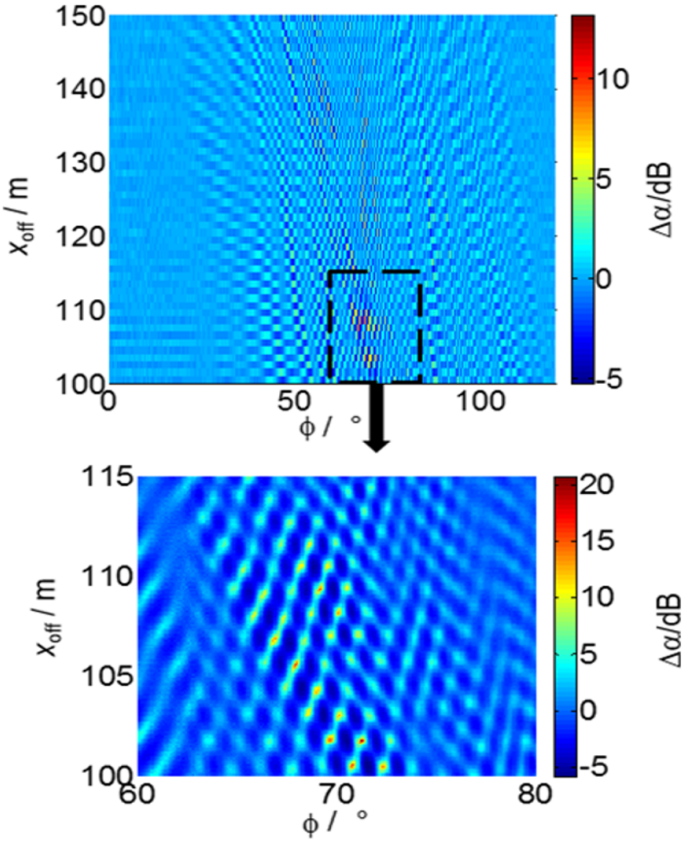

Figure 5-10: Diffraction loss $\Delta\alpha$ vs rotor angle ϕ and lateral offset x_{off} (top) with selected detail (bottom).

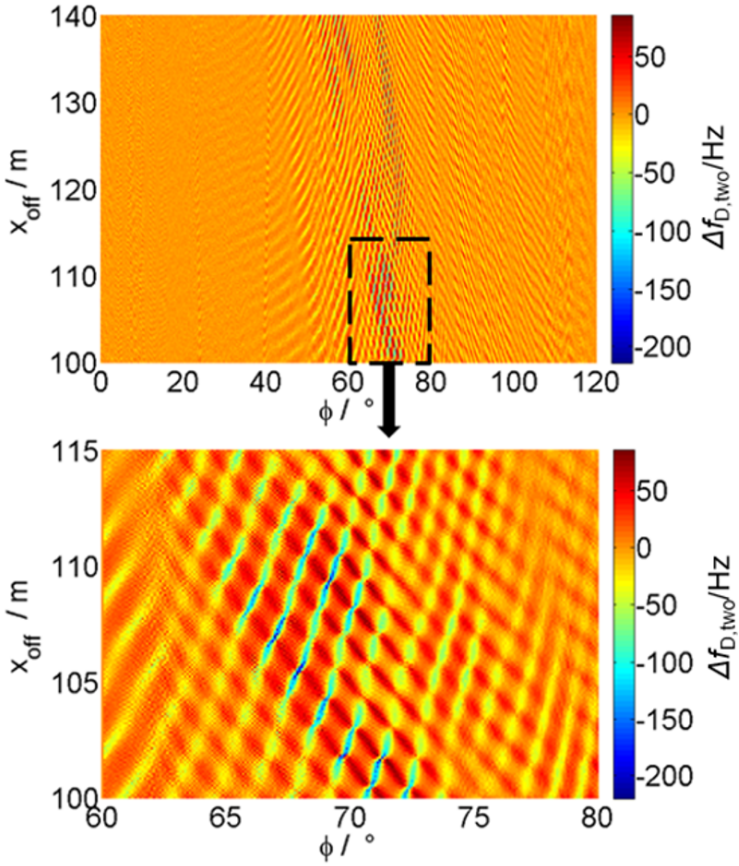

Figure 5-11: Two-way instantaneous Doppler shift $\Delta f_{D,\text{two}}$ - vs rotor angle ϕ and lateral offset x_{off} (top) with selected detail (bottom); rotational speed 15 RPM [127].

of rotor angle ϕ and the lateral offset x_{off}. Maximum value of $\Delta\alpha \approx 17$ dB is observed at ϕ=70° (see enlargement of selected area in Fig. 5-10 bottom). For an assumed rotor speed of 15 RPM, the corresponding instantaneous two-way Doppler deviation $\Delta f_{D,\text{two}}$ as a function of rotor angle ϕ and the lateral offset x_{off} is shown in Fig. 5-11. Maximum value of instantaneous two-way frequency deviation $|\Delta f_{D,\text{two}}|$ is -214 Hz observed at ϕ= 69.23° and x_{off}= 109.4m (see enlargement of selected area in Fig. 5-11 bottom). This value corresponds to an error in radial speed of almost 10 m/s. The strongest impact of the rotor observed for rotor angles where two blades are about tangential to the Fresnel zones.

In a practical scenario, the return signal will be evaluated by the radar over the time on target (pulse train) of duration τ_0 corresponding to the coherent processing time. To gain an insight into the diffraction induced time-frequency spectrum of the modulation signal m(t) corresponding to x_{off}= 109.4m, a value of τ_0 = 20ms is assumed. A Blackman window of length τ_0 is used to obtain the STFT of the time domain modulation signal m(t), shown in Fig 5-12. The obtained spectrum of the Doppler error contains significant signal components up to around 175 Hz.

5.3 Summary and Notes

An investigation of the impact of WT forward scattering on operational radar and radio communication links was presented in this chapter. Scenarios with destructive interference between LOS and ground reflected paths with expected strong impact of WT forward scatter are considered. Firstly, a fixed radio link with using 16 QAM modulation scheme is analyzed throughout end-to-end. The scenario considered is a link obstructed by a 3-blade rotor with a clearance greater than the 2nd Fresnel zone. Instantaneous MER as well as instantaneous and average raw data BER are used as important figures of merit. These are computed by considering amplitude and phase modulation calculated by the 2D Fresnel-Kirchhoff diffraction model. It is assumed that in the baseband, the spectrum of the diffraction induced amplitude and phase modulation lies above the crossover frequency of the amplitude and phase control loops of the receiver. Moreover,

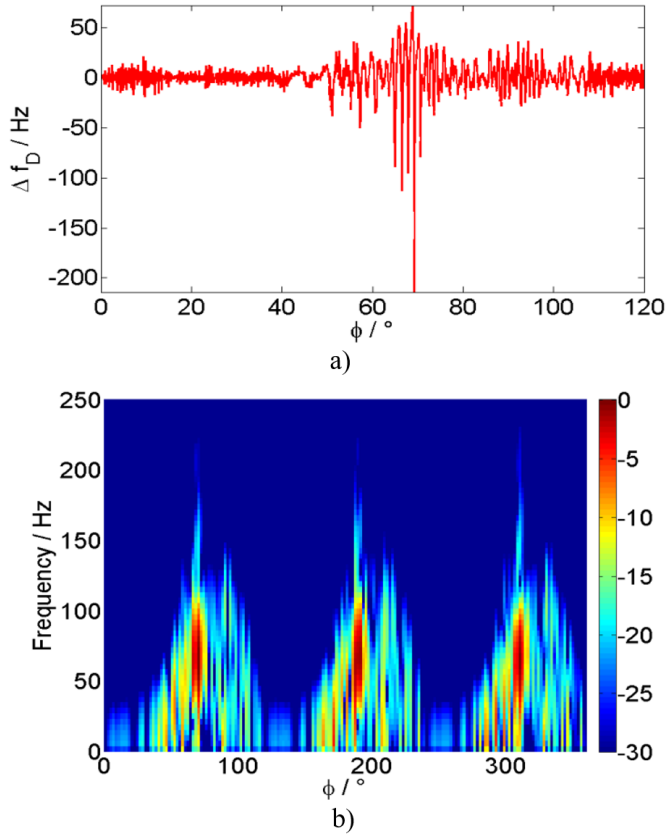

Figure 5-12: Impact of obstructing WT: (a) Two-way instantaneous Doppler shift $\Delta f_{D,\text{two}}$ and (b) STFT of round-trip signal vs rotor angle ϕ [127].

it is assumed that in the RF domain the interference will remain unaffected by filtering in the RF receiver chain. For the case of constructive interference of LOS path and ground reflected path (neglecting diffraction), the amplitude and phase modulation are only slightly higher than those for the case without the ground plane. Accordingly the corresponding MER values are only slightly lower causing the link to remain error free. However, for the case of destructive interference of LOS path and ground reflected path (neglecting diffraction) amplitude and phase modulation are significantly higher compared to those of the constructive interference case or the case without ground plane. Unacceptably low instantaneous MER values along with high corresponding BER values are observed in this case. This impact can only be mitigated by using pilot symbol assisted modulation. The investigation further highlights the fact that the high amplitude and phase distortion associated with destructive interference of direct and ground reflect paths can seriously deteriorate the performance of a fixed radio link.

To investigate the performance of radar systems under the effect of WT forward scatter, an S band marine radar fitted on a large cargo vessel is considered. A scenario based on almost destructive interference of LOS path and signal paths reflected at the sea surface has been investigated for a point target. The maximum instantaneous two-way Doppler error of $\mid \Delta f_{D,\mathrm{two}} \mid = 214$ Hz occurs where two blades are about tangential to the Fresnel zones. This value corresponds to an error in radial speed of 10 m/s. As the return signal is evaluated by the radar over the time on target (pulse train of duration τ_0) STFT with a window length of $\tau_0 = 20$ms has been applied. The time-frequency spectrum of the modulation signal thus obtained contains significant signal components up to 175 Hz. Principal results presented in this investigation are more general and except for the different beam profiles also hold true for S band air surveillance and weather radars.

The two examples considered in this chapter underline scenarios with strong impact of WT forward scatter on radar and fixed radio links. It has been verified that the strongest impact of WT forward scatter is observed when two rotor blades are tangentially obstructing the Fresnel zones. Moreover, it has been shown that rotor blades can cause strong interference even if located in higher order Fresnel zones. The investigation presented

further highlights the fact that the high amplitude and phase distortion associated with destructive interference of direct and ground reflect paths can seriously deteriorate the performance of a fixed radio link. Another major observation is that even with a clearance of more than two Fresnel zones usually suggested in literature, a serious impact of WT forward scatter is observed for a destructive interference case. A detailed study of various vital parameters presented in the next chapter aims to outline guidelines to avoid the strong impact scenarios highlighted above.

6 WT Forward scatter: Vital Parameters and Avoidance

The discussion leading up to this chapter has focused on efficient modeling and comprehensive analysis of WT forward scatter along with investigating its impact on radar and radio communication systems in order to outline the vital parameters and figures of merit for the comprehensive characterization of WT diffraction effects. From a practical point of view the degree of freedom for analysing WT forward scatter is extremely high. In terms of link parameters, there are frequency, antenna locations, orientations, and beam patterns. In addition, there are WT parameters like location, shape, size and operating parameters like wind speed, pitch, yaw, and rotor angle. Using a time consuming brute force method based on 3D numerical field simulation instead of Fresnel-Kirchhoff diffraction approach would not only be less computational efficient but also could not provide a definite answer on if the worst-case parameter constellation found is only a local solution. The comprehensive understanding presented so far allows for tracing critical conditions (worst case scenarios) of WT forward scatter. In this chapter we explore how various important (link and WT) parameters influence the forward scatter of a WT and aim to identify the critical conditions in terms of diffraction loss, phase modulation and frequency deviation. This goes a long way in outlining the guidelines to avoid the scenarios of strong impact of the WT forward scatter on communication links and radar systems.

6.1 Ray Path Parameters

Based on the investigation presented in the preceding chapters, some important conclusions can be drawn straight away. The most important aspect in characterizing the forward scatter is the way in which the Fresnel zones are obstructed. Fresnel zones of smaller width are observed for higher frequencies and smaller values of d_1 and d_2, according to eqn. (2.33). The faster a rotor blade traverses a Fresnel zone tangentially the higher the instantaneous frequency shift Δf_D of the forward scattered signal. For a radar system, as the operational frequency increases, the width of the Fresnel zones decreases inversely proportional to $1/\sqrt{f}$ and consequently the frequency deviation increases directly proportional to $\sqrt{f}$. However, as more generally the Doppler shift of a moving target is directly proportional to f, the error in calculated radial speed due to rotor forward scattering scales proportional to $1/\sqrt{f}$. Therefore, at higher frequencies, a lower impact of forward scattering on the error in measured radial speed can be expected as compared to lower frequencies. That is also the reason why the S band radar was considered in section 5.2 as it is more prone to errors in measured radial speed due to WT forward scatter than a X band radar.

For scenarios, where the WT is closely located to the signal path, the rotating blades cut through Fresnel zones of low order. This may result in rather high values for $\Delta\alpha$ and$\Delta\beta$, however the spectrum of these signals will contain rather low frequency components. If located further away from the signal path the blades will cut through Fresnel zones of higher order, moving through a higher number of Fresnel zones for a given time resulting in high frequency components in the spectrum of the forward scattered signal. For a given distance between transmit and receive terminals (d=d_1+d_2), the largest radius of the Fresnel zones is observed for the symmetrical case (d_1=d_2). If the LOS path lies within the WT rotor swept area, an asymmetrical link ($d_1 \neq d_2$) will result in narrower obstructed Fresnel zones and a relatively higher degree of obstruction of the lower order Fresnel zones and thus higher values of $\Delta\alpha$. For radar applications, smaller values of d_1 and d_2 will produce a smaller width of the Fresnel zones, resulting in a faster traversing of the zones by the rotor blades and thus an increase in the measured Doppler error.

An important link parameter is the beamwidth of the antenna, which determines the number of illuminated Fresnel zones. A wide beam will

ensure that the higher order zones of smaller width cannot be ignored, producing higher frequency components in the spectrum of the forward scattered signal, thus increasing the measured Doppler error. Fig. 6-1(a) displays the diffraction loss $\Delta\alpha$ versus rotor angle ϕ with varying HPBW for the link scenario considered in section 3.1 (f=1.30 GHz, d_1=d_2=4000 m, l_b=64 m, w_b=1.5 m). As can be expected the impact of higher order Fresnel zones decreases with reducing the antenna beamwidth. In the case of the narrowest beam (HPBW = 0.03°) significant signal modulation is observed only for a very narrow range of rotor angles around ϕ=0°. Fig. 6-1(b) displays the diffraction loss $\Delta\alpha$ versus rotor angle ϕ with parameter offset y_{off} between rotor and beam axis in the plane of obstruction for the case HPBW = 0.23°. A significant reduction of signal modulation is observed in those cases where the LOS path is not obstructed by the rotor swept area. It can be seen from the ripples in the curves around ϕ =60° that in those cases still higher order Fresnel zones will contribute to the signal modulation.

Another aspect of a wider beamwidth is the illumination of the ground plane, which gives rise to a complex interference between the four paths discussed in sections 4.3 and 5.2. If the heights of the antenna are such that a destructive interference scenario between the direct and ground reflected paths is produced, a serious impact of the forward scattered signal can be expected. The high amplitude and phase distortion associated with destructive interference of direct and ground reflect paths can seriously deteriorate the performance of a fixed radio link. For radar systems with wide beamwidths like marine radars, the impact on $\Delta\alpha$ will be stronger, and in addition to that, higher frequency components will be induced due to the contributions from the ground reflected paths.

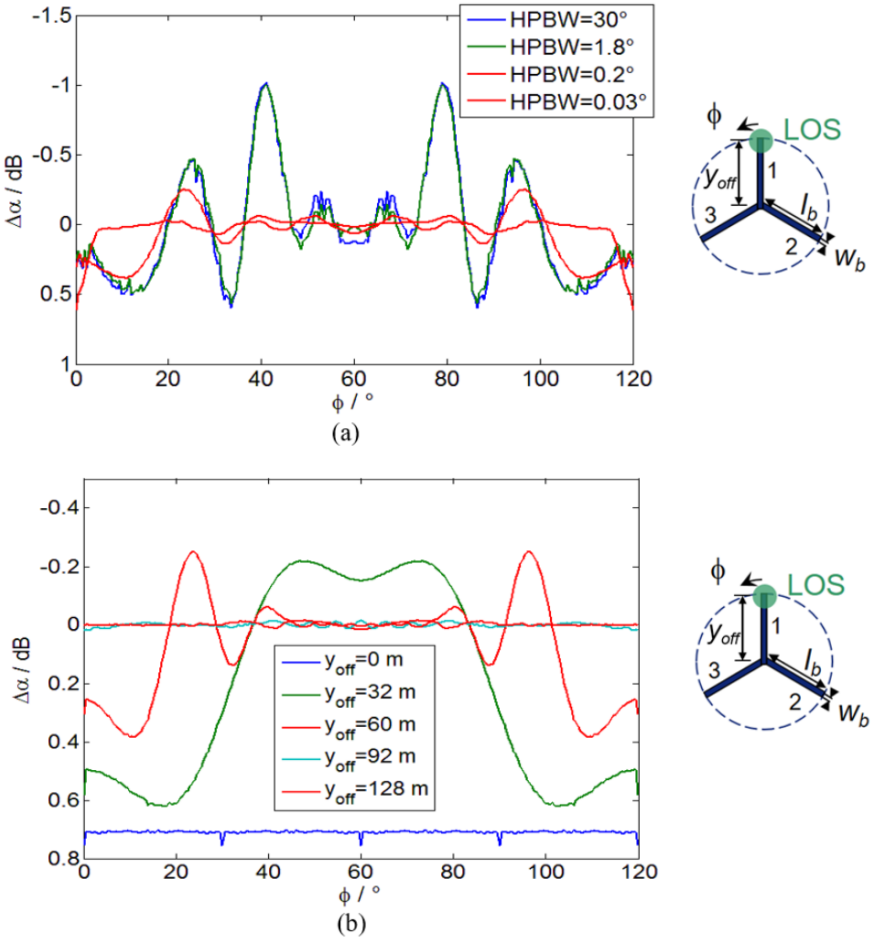

Figure 6-1: Diffraction loss $\Delta\alpha$ vs rotor angle ϕ for a) y_{off} =60m, varying HPBW b) HPBW=0.47°, varying y_{off} [122].

6.2 WT Parameters

In this section, the impact of important WT parameters which determine the extent of shading of the Fresnel zones is investigated. The 2D Fresnel-Kirchhoff diffraction approach is used to study the impact of parameters like blade dimensions and pitch and yaw angle dependent rotor orientation (Fig. 1-2). A spherical wave approximation is used which in effect removes the impact of the beam shape on rotor illumination. For simplification, it is assumed that the ground plane is not illuminated by the incident beam and thus ground reflections behind the WT due to diffraction can be ignored.

6.2.1 Blade Width

First, the impact of the blade width w_b is investigated by considering a single rectangular blade [126]. In the considered scenario, the LOS path is assumed to be aligned perpendicular to the rotor plane (collinear with the rotor axis) with frequency f = 5.64 GHz and d_1 = d_2 =4000 m. The impact of the tower and rotor hub is neglected. For the given parameters, the extent to which a Fresnel zone is obstructed, or the effectiveness of shading a zone is determined by the width, shape and the pitch angle of the blade. When the blade is tangentially aligned with respect to a particular Fresnel zone, the maximum impact at the tangential point in terms of amplitude modulation and frequency deviation can be expected if the blade width w_b is almost equal to the width W_n of the tangentially obstructed Fresnel zone of number n. The (outer) radius of the n^{th} Fresnel zone R_n (eqn. 2.33) can be expressed in terms of the radius of the 1st Fresnel zone R_n as shown below

$$R_n = \sqrt{n} R_1 \tag{6.1}$$

The corresponding width W_n of the n^{th} Fresnel zone can be given as the difference between the radius of the n^{th} and $n-1^{th}$ zones

$$W_n = R_n - R_{n-1} = (\sqrt{n} - \sqrt{n-1}) R_1 \tag{6.2}$$

The maximum impact in terms of $\Delta\beta$ will be observed when the blade is tangentially oriented at the outer boundary of a Fresnel zone such that w_b spans the width $W_{(n,n+1)}$ between the center of the n^{th} and n+1th zones as given below:

$$W_{(n,n+1)} = \left(\sqrt{n+\frac{1}{2}} - \sqrt{n-\frac{1}{2}}\right) R_1 \tag{6.3}$$

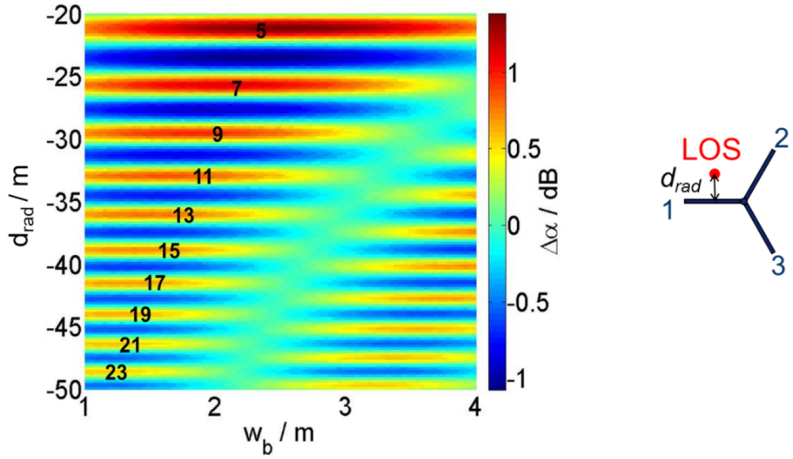

Figure 6-2: Diffraction loss $\Delta\alpha$ produced by a single rectangular blade oriented tangentially to the Fresnel zones (index n shown in graph) as a function of blade width w_b and radial distance to the LOS path d_{rad} [126]

For the considered scenario of a single blade tangentially oriented to the Fresnel zones, Fig. 6-2 represents the corresponding diffraction loss $\Delta\alpha$ as a function of blade width w_b and radial distance d_{rad} from the center of the blade to the LOS path. The numbers included in the plot show the index n of the respective tangentially obstructed Fresnel zones. The maximum value of diffraction loss can be observed when the 5th Fresnel zone is obstructed such that the width of the blade is almost equal to the corresponding zone width (w_b = W_5= 2.43 m). The corresponding radial distance between the center of the blade and LOS path (d_{rad} = R_4= 20.7 m) enables the blade to span the entire width of the 5th Fresnel

zone. An increase in the value of the radial distance d_{rad} also increases the order n of the Fresnel zone being obstructed consequently. As a result, the optimum value of w_b for extrema of $\Delta\alpha(w_b)$ is decreased. An increase in the value of w_b beyond this optimum value causes the blade to start obstructing both the neighboring Fresnel zones. This produces an increase in signal components with opposite phase thus reducing the overall value of $\mid \Delta\alpha(w_b) \mid$. A further increase in the value of w_b causes an obstruction of an odd number m of consecutive Fresnel zones ($n-1$, n, $n+1$ for m=3). More maxima and minima of $\Delta\alpha(w_b)$ are observed in this case, located at $d_{\text{rad}} = \left(\frac{R_{(n+1)}+R_{(n-1)}}{2}\right) = \left(\frac{\sqrt{(n+1)}+\sqrt{(n-1)}}{2}\right)R_1$ and $w_b = R_{(n+1)} - R_{(n-1)} = (\sqrt{n+1} - \sqrt{n-1})R_1$ as seen in the bottom right part of the plot in Fig. 6-2.

An important observation about Fresnel clearance for a WT rotor with rectangular blades can be made using the scenario under discussion. Traditional exclusion zone models prescribe Fresnel clearance based on half plane diffraction model (section 2.2.2). This may not be completely accurate for the case of a WT rotor, especially for scenarios where the blade width is equal to the width of an obstructed Fresnel zone. Figure 6-3 shows the diffraction loss plot (E_R/E_S in linear scale) obtained by using half plane diffraction approach for the scenario considered in this section. The blue vertical lines represent the extent of the first Fresnel zone. The first peak of diffraction loss outside the first Fresnel zone corresponds to a diffraction loss of 1.09 dB, which implies that for a clearance of first Fresnel zone, the maximum expected diffraction loss value can be of 1.09 dB. However, from the plot in Fig. 6-2, it can be seen that a diffraction loss of 1 dB is obtained even when a single blade is tangentially oriented inside the 7th Fresnel zone. It can be concluded that the Fresnel clearance for rectangular blade is higher than that prescribed for an obstructing half plane.

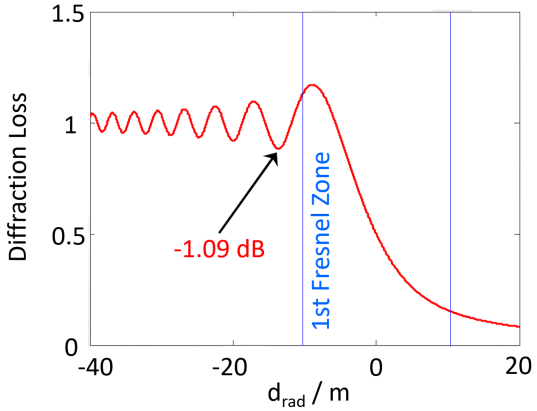

Figure 6-3: Diffraction loss for half plane obstruction

In contrast to the single blade considered so far in this section, for a three-blade rotor the Fresnel zones can be tangentially obstructed by two blades at the same time. Fig. 6-4 shows the diffraction loss for a three-blade rotor as a function of blade width w_b and the radial distance from the center of the blade to the LOS path d_{rad}. A significant interference due to the signal contributions from the two additional blades can be observed as the value of d_{rad} is increased. The order n of the obstructed Fresnel zones increases with an increase in the distance d_{rad}, causing a decrease in the optimum value of w_b for the extrema of $\Delta\alpha(w_b)$.

6.2.2 Blade Pitch

To study the impact of pitch angle, the WT blades can be characterized by an effective blade width w_{beff}, which is a function of the blade width w_b and pitch angle β_p as represented below

$$w_{beff} = w_b \cos \beta_p \tag{6.4}$$

A single rectangular blade is considered to be tangentially oriented with respect to the Fresnel zones, with a radial distance d_{rad} between the blade

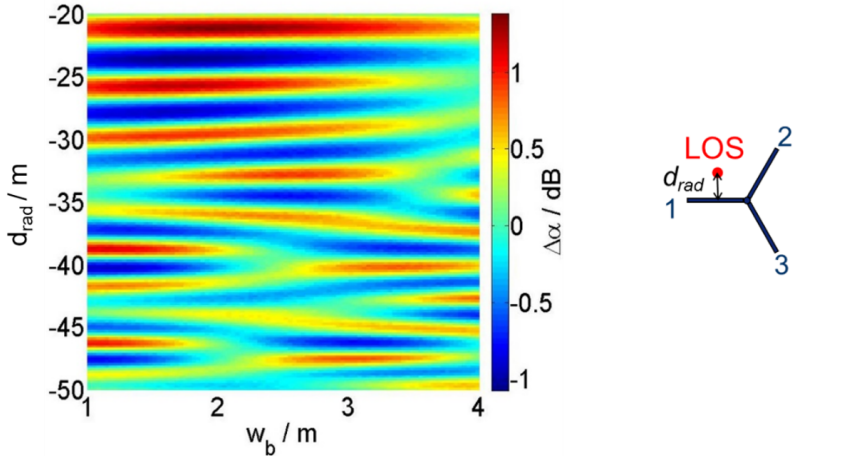

Figure 6-4: Diffraction loss $\Delta\alpha$ produced by three (rectangular) blade rotor as a function of blade width w_b and radial distance to the LOS path d_{rad} [126]

center and the LOS path. To simplify the investigation, the pitch angle β_p is considered to be unique for the whole blade. In practice, the maximum value of β_p is observed to be almost 25°. The corresponding effective blade width w_{beff} for the maximum β_p is about 90% of the actual blade width w_b. Based on the observations made in section 6.2.1, no significant consequent variation of $\Delta\alpha(w_{beff})$ can be expected if w_b is in the order of the width of a single Fresnel zone. A major impact of the pitch angle β_p will only occur if the variation of the effective blade width w_{beff} is in the order of the width of an obstructed Fresnel zone. This only holds true if several higher order Fresnel zones are being obstructed at the tangential point, implying a wide illuminating beam in most cases.

Fig. 6-5 shows the diffraction loss as a function of blade pitch angle β_p (ranging between w_{beff}= 2.5 – 2.8 m) and the radial distance d_{rad} from the center of the blade to the LOS path (covering 68$^{\text{th}}$ to 94$^{\text{th}}$ Fresnel zones for W_{68}= 0.628 m to W_{94}=0.533 m). The width of the rectangular blade w_b is assumed to be 2.8 m. All other parameters are same as the scenario considered in section 6.2.1. The maximum impact of β_p is observed to be

only a few tenths of a dB.

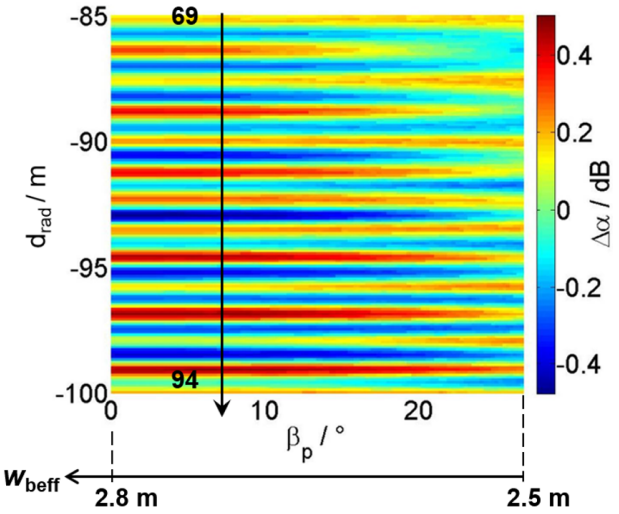

Figure 6-5: Diffraction loss $\Delta\alpha$ as a function of pitch angle β_p and radial distance to the LOS path d_{rad} ; single rectangular blade, w_b =2.8m [126]

6.2.3 Blade Shape

In addition to the generic rectangular blades used in our previous investigations, two other blade shapes are now considered. These include triangular blades, which is a decent approximation for a variety of recent WTs, and a scaled approximation of Vestas V164-8.0 rotor blades, closely resembling the blade shape of most large turbines. To compare the diffraction effects of the three shapes considered, a blade length l_b (radius of swept area) of 82 m is used. The width of the rectangular and triangular blades (symmetric along blade axis) is selected such that it matches the width of the Vestas V164-8.0 blade (asymmetric along blade axis) midway along the blade length $w_b(l = l_b/2)$ = 2.77 m, as shown in Fig. 6-6

.

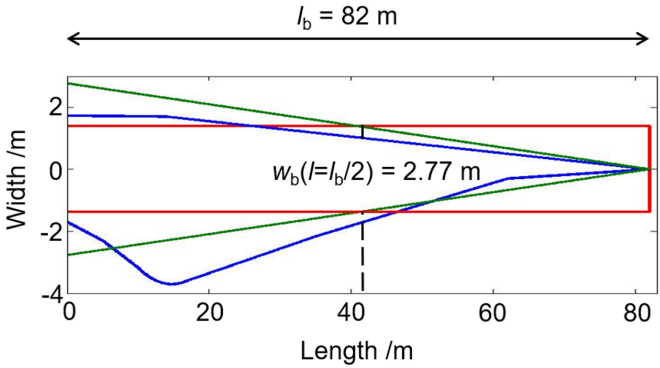

Figure 6-6: Blade shapes for zero pitch angle (not drawn to scale): generic rectangular (red) and triangular (green) blades, and approximation of Vestas V164-8.0 blades (blue) [126].

To study the impact of blade shape, consider a three blade rotor with a hub of radius r_{hub} =5.5 m, a frequency f = 5.64 GHz and d_1 =d_2 =4000 m. The pitch angle is set to β_p= 0°. The radial distance to the LOS path is now considered with respect to the rotor axis (represented by r_r) instead of the center of the blade (as in the case of d_{rad}). Fig. 6-7 represents the corresponding diffraction loss $\Delta\alpha$ as a function of rotor angle ϕ and radial distance r_r between rotor axis and the LOS path for the rectangular blade rotor. The range of r_r values is chosen such that the 4$^{\text{th}}$ to24$^{\text{th}}$ Fresnel zones are covered (W_4= 2.76 m to W_{24}=1.06 m) for the rectangular blade. Representing $\Delta\alpha$ in the (ϕ, r_r) space allows any horizontal or vertical offset between LOS path and rotor axis to be characterized by the single independent parameter r_r in addition with a simple shift along the ϕ axis in accordance with the angular orientation of LOS path with respect to the rotor axis.

For the considered scenario, blade 1 cuts through the LOS path for ϕ=0°, whereas the blade 2 does so at ϕ=120°. Therefore, the tangential point at blade 1 moves towards the rotor axis as the value of ϕ increases from 0° to 90°, while the point at blade 2 moves away from the rotor axis as value of ϕ increases from ϕ from 30° to 120°. The mutual interaction of the individual signal contributions from each blade produces an interference pattern. As

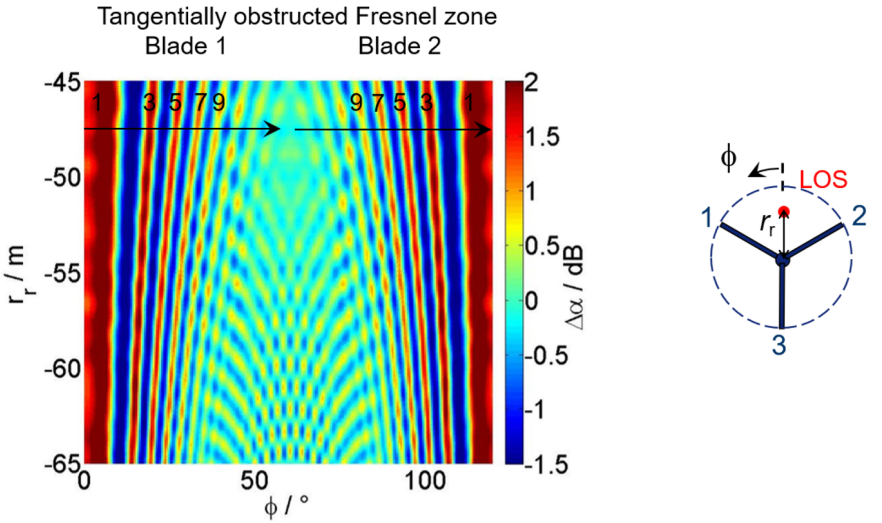

Figure 6-7: 3-blade rotor with hub: Diffraction loss $\Delta\alpha$ vs rotor angle ϕ and radial distance r_r for rectangular blades [126]

the three blades have different respective widths for $l \neq l_b/2$, differences in $\Delta\alpha$ due to blade shape become obvious for the tangential point at the Fresnel zones moving away from l=$l_b/2$. This is clearly evident from Fig. 6-8 (a) and (b) where the corresponding diffraction loss $\Delta\alpha$ for triangular and approximated Vestas V164-8.0 blades is represented as a function of rotor angle ϕ and radial distance r_r.

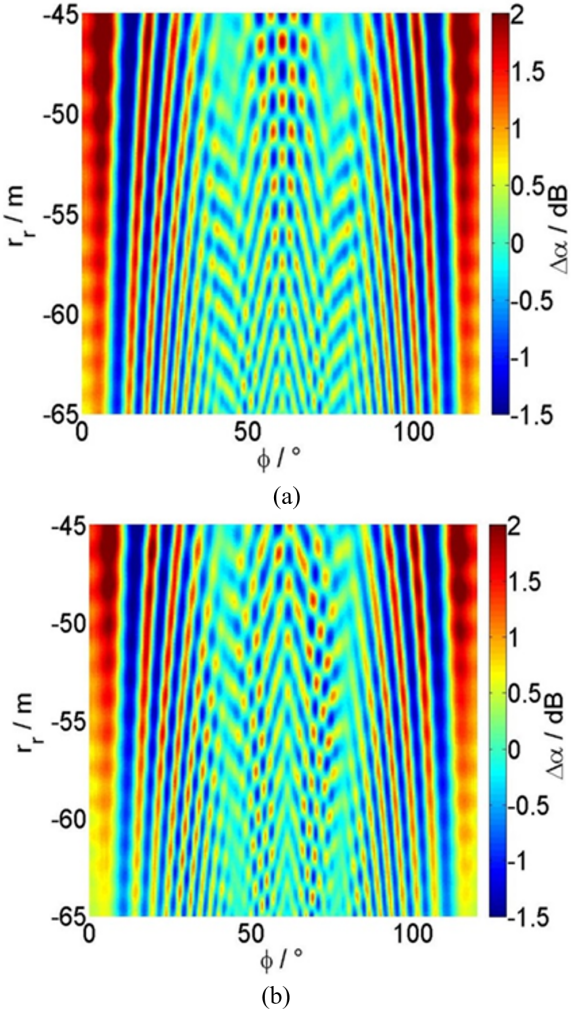

Figure 6-8: 3-blade rotor with hub: Diffraction loss $\Delta\alpha$ vs rotor angle ϕ and radial distance r_r for (a) triangular blades and (b) scaled version of Vestas V164-8.0 blades, β_p=0° [126].

6.2.4 Yaw Angle

To study the impact of the yaw angel, the 2D Fresnel diffraction model is used such that the aperture itself is rotated around the yaw axis corresponding to the yaw angel (γ = 0 – 360°) being considered (Fig. 6-9) [128]. Projecting the WT into the plane of obstruction, $\Delta\alpha$ is calculated as a function of ϕ and γ.

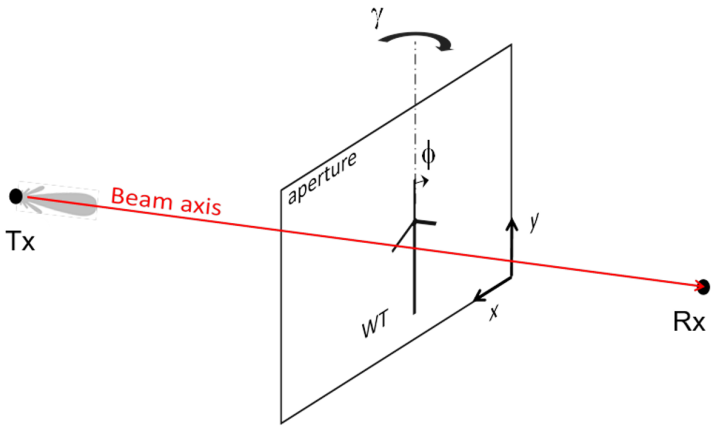

Figure 6-9: WT projected into plane of obstruction (aperture) with rotor angle ϕ and yaw angle γ [128].

The following analysis focuses on a scenario with frequency f = 5.64 GHz, a rotor with three rectangular blades of length l_b = 64 m and width w_b = 2.5 m, d_1 = d_2 = 6000 m. It is assumed that the ground plane is not illuminated by the incident beam. Moreover, the impact of the tower will be neglected as the tower only produces an offset in the overall value of $\Delta\alpha$ independent of yaw angle. In all the investigations presented in earlier chapters, yaw angle variations were not considered, and all results hold true for γ=0°. To conduct the analysis for highest values of $|\Delta\alpha|$, a rotor angle of ϕ =30° is considered (Fig. 6-10) such that two blades are oriented symmetrically and tangentially with respect to the Fresnel zones.
The corresponding diffraction loss $\Delta\alpha$ is displayed in Fig. 6-10 as a function of yaw angle γ and lateral offset of the LOS path from the rotor axis x_{off}. The order of the respective tangentially obstructed Fresnel zones (1$^{\text{st}}$ to 18$^{\text{th}}$) is shown by the numbers included in the graph. For $\gamma \neq 0°$, elliptically

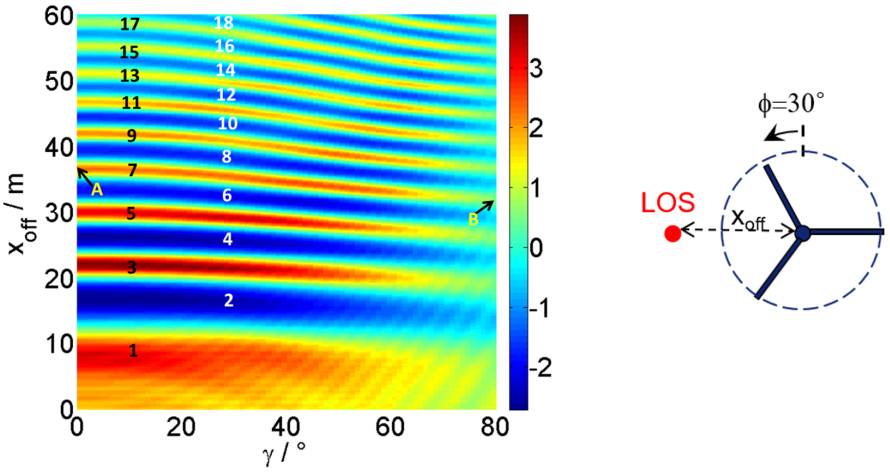

Figure 6-10: Diffraction loss $\Delta\alpha$ as a function of yaw angle γ and lateral offset x_{off} with numbering of the order of the shaded Fresnel zones ; (right) Simulated scenario: rotor model (ϕ =30°) [128].

shaped zones are obtained by the projection of the Fresnel zones into the rotor plane (as shown in Fig. 6-11 (b)). This causes the shaded Fresnel zones to appear as stripes slightly dipping towards higher values of the yaw angle γ. Increasing the value of γ reduces the relative overlap of the predominantly shaded zone and the two tangentially aligned blades as it is shortened alongside blade axis and narrowed relative to the growing projected zone width alongside blade width.

For lower order Fresnel zones (n= 1 to 4 in this case), as the blade width w_b is smaller than the zone width W_n, the maxima and minima of $\Delta\alpha$ within each zone can be expected to occur for γ= 0°. For zones n= 5 and n= 6, extrema of $\Delta\alpha$ are observed at γ equal to 29.3° and 46° respectively, with values only negligibly higher than the corresponding values of the extrema observed for γ = 0°. For these zones, the respective zone width W_n is only slightly larger than the blade width w_b due to which the blades remain inside the zone n without shading zone n+1 at one end and not shading zone n-1 around the tangential point at the same time. Consequently, a higher impact on the reduction of shading both neighboring zones $n\pm1$ next to the predominantly shaded zone n occurs. For higher order Fresnel

zones (for n >6 in this case), blade width w_b is larger than W_n. Despite this, extrema of $\Delta\alpha(\gamma)$ can be observed at γ >0° at instances when the increased projected zone width matches the width of the blade. This can be observed in Fig. 6-10 from the 7th Fresnel zone onwards (W_7 = 2.47 m). However, it is important to note that all the extrema ocurring in higher order zones have values smaller than the worst case values (here $\Delta\alpha_{max}$ = 3.88 dB for n= 3, γ=0, $\Delta\alpha_{min}$ = -2.57 dB for n= 2, γ= 0°). Another interesting obervation is that the maximum value of diffraction loss is obtained for obstruction of the 3rd instead of the 1st Fresnel zone. This is due to the fact that the rotor axis lies well within the 1st Fresnel zone such that both blades are not traversing this zone to the full extent, whereas in the former case, the 3rd zone is obstructed to a considerable extent by both the blades tangentially oriented within the zone. It has to be stated that the rotor hub which has been ignored in this analysis, would cause an additional obstruction of the Fresnel zones in a practical scenario. Moreover, since a 2D approach has been used in this investigation, the impact of the WT nacelle for higher values of yaw angle γ will be underestimated. From the example considered, it can be stated that if the dimensions of the WT rotor hub are significantly smaller than the radius of the 1st Fresnel zone and the blade width is not larger than the width of the 3rd Fresnel zone, maximum obstruction loss of a three-blade rotor occurs for two blades oriented symmetrically tangential within the 3rd Fresnel zone for yaw angle γ= 0°. If the dimensions of the hub are not significantly smaller than the radius of the 1st Fresnel zone, maximum obstruction loss occurs for two blades oriented symmetrically tangential within the 1st Fresnel zone (at γ= 0° as long as the hub does not exceed the first Fresnel zone). For the Fresnel zones where the zone width W_n is smaller than the blade width w_b, additional local extrema of obstruction loss are located for γ >0°. Similar principles apply to a similar symmetric scenario where the LOS path cuts through the plane of obstruction right above the rotor axis with ϕ = 60°.

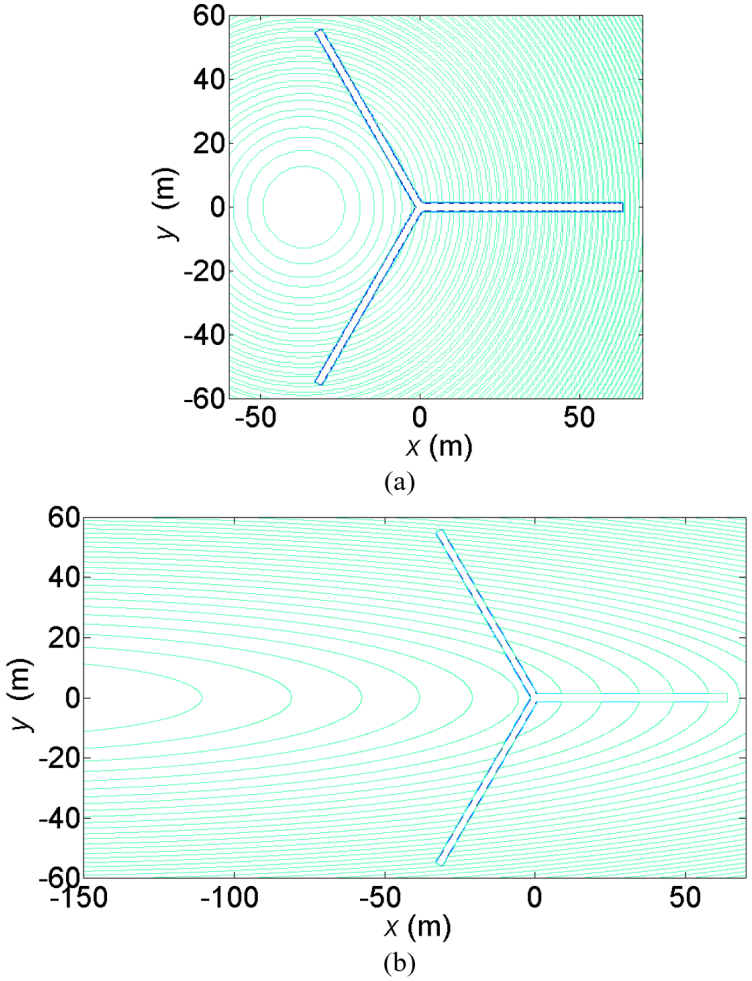

Figure 6-11: Plane of obstruction with rotor (blue) and Fresnel zones (green) for (a) point A (γ=0°, x_{off} = 36.5m) and (b) point B (γ=80°, x_{off}= 31.9m) [128].

6.3 Strongest Impact Avoidance Guidance

This chapter focused on investigating how important individual parameters effect the forward scatter of a wind turbine and outlining the critical conditions for strongest impact. Ray path parameters like the frequency of operation, along with distances d_1 and d_2 determine the size of the Fresnel zones and consequently dictate the constellation of parameters that determine how the Fresnel zones are being obstructed. Wider antenna beams result in significant ground plane reflections. Depending upon the antenna heights, this may result in a destructive interference between the direct and ground reflected signals which in worse case can be critical for radar and radio communication links. Other scenarios with significant impact of WTI will depend on WT parameters, most notably the width of the blade and how it compares to the width of the zones being obstructed. Blade width determines the extent of shading observed in a Fresnel zone and can have a strong impact if it is close to the width of the Fresnel zone being tangentially obstructed. Blade pitch and yaw has a low impact except for very narrow zones, observed at short distances or with very wide beams. Large WT rotor diameters (or longer blades) increase the affected area and the number of Fresnel zones being obstructed, along with the speed at the blade tip. Consequently, the error in measured radial speed by a radar system increases. Higher error in measured radial speed is also observed for higher rotational speed of the rotor resulting in the Fresnel zones being traversed faster, which in turn increases the error in the measure radial speeds.

As observed earlier, the Fresnel clearance for rectangular blade is higher than that prescribed for an obstructing half plane. From the discussion presented earlier, it can be recalled that when the blade width w_b is not significantly larger than the width W_n of an obstructed Fresnel zone, a strong impact of the forward scatter is observed when a rotor blade is aligned tangentially to a Fresnel zone. The strongest impact is observed when two blades are aligned tangentially to a Fresnel zone at the same time. To outline guidelines to avoid this condition of strong impact of WT forward scatter, consider a WT obstructing a beam such that the LOS path lies within the rotor swept area, as shown in Fig. 6-12. The blade width w_b is not significantly larger than the width W_n of an obstructed Fresnel zone. During one complete rotor cycle, the shaded half circle represents the instances (50% of the total time) where each blade will be

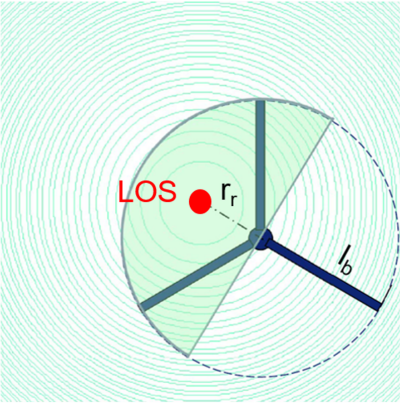

Figure 6-12: Plane of obstruction with rotor (blue) and Fresnel zones (green) with LOS path within the rotor swept area; Shaded region represents the time instances where a blade can tangentially obstruct the Fresnel zones

aligned tangential to a Fresnel zone. Around 50% of the total time, two blades will be tangential to the Fresnel zones at the same time. Half of this time (approx. 25% of the total time), two blades will be either tangentially obstructing an even zone or an odd zone. Outside the shaded half circle, no blade will cause a predominantly tangential obstruction of a Fresnel zone. This is summarized in table 6.1.

Table 6.1: Strong WT forward scatter Impact – LOS path inside rotor swept area

Tangential Fresnel Zone Obstruction	**Time Span (%)**
Each blade	50
Two blades at a time	50
Two blades in either even or odd zone at a time	25

Fig. 6-13 shows the case when the LOS path lies outside the rotor swept area, with a radial distance r_r between the rotor axis and the LOS path. In

this scenario, the percentage of time a blade causes a tangential obstruction of a Fresnel zone reduces (from 50% in the previous case) to $\frac{1}{\pi}\sin^{-1}(\frac{l_b}{r_r})$ ×100%, where $\sin^{-1}(\frac{l_b}{r_r})$ corresponds to the angle where the tangential point lies at the blade tip (Fig. 6-13). The two shaded sectors illustrate the instances when two blades at the same time are tangential to the Fresnel zones and thus the corresponding percentage of time can be given as $\frac{1}{\pi}(\sin^{-1}\frac{l_b}{r_r} - \frac{\pi}{6})$ ×100%. Half of this time $\left(\frac{1}{2\pi}(\sin^{-1}\frac{l_b}{r_r} - \frac{\pi}{6})100\%\right)$ two blades will both be tangentially obstructing the same parity zone. In other words, during these instances the two blades at the same time will be obstructing either even zones or both will be shading odd zones. These time span percentages are summarized in table 6.2.

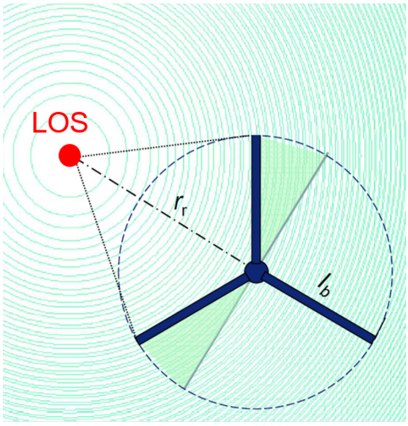

Figure 6-13: Plane of obstruction with rotor (blue) and Fresnel zones (green) with LOS path outside the rotor swept area; Shaded region represents the time instances where a blade can tangentially obstruct the Fresnel zones

In order to outline a scheme to avoid the critical scenario of WT forward scatter when two blades are tangentially obstructing the same Fresnel zone, the time span percentages represented in tables 6.1 and 6.2 can be plotted against the ratio of blade length to radial distance from the LOS path ($\frac{r_r}{l_b}$) as shown in Fig. 6-14. For $\frac{r_r}{l_b} < 1$, The LOS path lies within the rotor swept area and the time span of each blade or two blades at the same time tangentially obstructing a Fresnel zone is 50%, whereas two blades

Table 6.2: Strong WT forward scatter Impact – LOS path outside rotor swept area

Tangential Fresnel Zone Obstruction	**Time Span (%)**
One blade in either even or odd zone	$\frac{1}{\pi}\sin^{-1}(\frac{l_b}{r_r})$
Two blades at a time	$\frac{1}{\pi}\left(\sin^{-1}(\frac{l_b}{r_r})-\frac{\pi}{6}\right)$
Two blades in the same parity zone	$\frac{1}{2\pi}\left(\sin^{-1}(\frac{l_b}{r_r})-\frac{\pi}{6}\right)$

obstructing an even or an odd zone at the same time is 25%. For $\frac{r_r}{l_b} > 1$, the LOS path lies outside the rotor swept area. In this region, the curves for two blades tangentially obstructing the Fresnel zones diminish to zero for $\frac{r_r}{l_b} \geq 2$. It can be deduced that when the radial distance between the LOS path and the rotor axis is greater than twice the blade length, the severe situation where two blades are aligned tangentially to the Fresnel zones at the same time is not encountered.

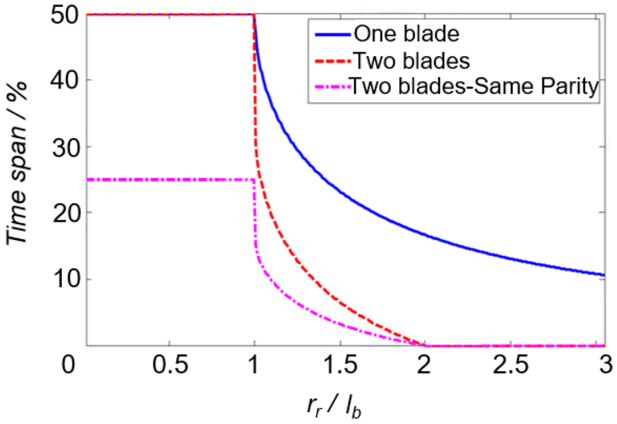

Figure 6-14: Percentage of time aligned tangential to Fresnel zones vs normalized radial offset LOS path – rotor axis

7 Summary and Conclusions

A comprehensive study of WT forward scatter is presented in this dissertation. A 2D Fresnel diffraction approach has been used for the first time to model the WT forward scatter. A straight forward 1D diffraction model proposed for the calculation of the dynamic amplitude and phase modulation has been found to produce decent approximations for a limited set of propagation scenario involving a single rotor blade with signal paths inside the rotor swept area and no ground plane effects. A more accurate and versatile 2D Fresnel-Kirchhoff diffraction approach has been applied for an inclusive modelling of the WT diffraction effects in more complex propagation scenarios involving signal paths in as well as outside the rotor swept area. Impact of an illuminated ground plane has been accounted for by considering an image transmitter and an image receiver (or target). The incorporation of the reflection coefficient of the ground plane allows for a decent approximation of both perfect conducting as well as lossy ground surfaces and provides a major flexibility in the modelling of complex interference scenarios. The polarization of the signal in the scenarios considered is assumed to be vertical, unless mentioned otherwise. The 2D Fresnel-Kirchhoff diffraction model results agree well with those obtained by FEKO UTD simulations, proving its suitability for the analysis of WT diffraction effects.

An in-depth understanding of the WT forward scatter has been presented by explaining the patterns of obstruction gain and loss along with the associated phase modulation in terms of obstructed Fresnel zones. For the rotor forward scatter, when a sufficient number of Fresnel zones are illuminated, maxima of diffraction loss $\Delta\alpha$ occur for rotor angles when a blade is oriented tangentially within an odd Fresnel zone, whereas the minima are observed when a blade is tangentially obstructing an even Fresnel zone. This holds true as long as only a single blade is tangentially oriented with

respect to the illuminated zones and the blade width w_b is not larger than the width of the obstructed Fresnel zone. Significantly higher impact is observed if two blades are oriented tangentially within either illuminated even or odd Fresnel zones at a time. The impact is at its strongest when the two blades are tangentially obstructing zones of the same parity (i.e. either both blades in odd or both blades in even zones). The maxima of diffraction induced phase shift $\Delta\beta$ occur for blade orientations at the outer boundary of an odd zone, whereas the minima are seen for blades oriented at the outer boundary of an even Fresnel zone. The WT tower contributes to the overall diffraction loss of the WT with an offset which is predominantly equal to the diffraction loss due to the tower alone. The time-variant overlap between tower and blades in the plane of obstruction results in a change of the AC component of $\Delta\alpha$ around rotor angles of ϕ= 60° (for rotor axis aligned collinear with LOS path). This change is significant in cases when the overlapping blade would be oriented tangentially within a Fresnel zone or cuts right through the line-of-sight (LOS) path at about $1/\sqrt{2}$ times the radius of the 1st Fresnel zone. In this case, the tower shades a distinct in-phase or distinct out-of-phase signal component, and, thus, reduces the corresponding maximum or minimum of $\Delta\alpha(\phi)$, respectively. The impact of an illuminated ground plane is presented by inspecting the obstruction of the Fresnel zones of the four paths (Tx–Rx, Tx–Rx, Tx–Rx, and Tx–Rx). In this regard, both symmetrical (d_1=d_2 and h_{Tx}=h_{Rx}) as well as asymmetrical links with constructive as well as destructive interference between direct and ground reflected paths are considered. It is observed that the paths without ground reflection (Tx–Rx) have high signal amplitude and lower modulation frequency components, whereas paths including double ground reflection (Tx–Rx) have small signal amplitudes but the highest modulation frequency components due to the obstruction of higher order Fresnel zones. Link scenarios which provide constructive interference of LOS path and ground reflected path are less prone to provide a strong influence of WTI, whereas a destructive interference produces a serious impact in terms of the observed values of the $\Delta\alpha$, $\Delta\beta$ and the instantaneous frequency deviation Δf_D. This is verified by investigating the impact of WT forward scattering on operational radar and radio communication links. Firstly, a fixed radio link with higher order modulation scheme (16 QAM) is analyzed. It is assumed that in base band, the spectrum of the interference signal lies above the crossover frequency of the amplitude and phase control loops of the receiver. Moreover, it is assumed that in the RF domain the interference will not be affected by

filtering in the RF receiver chain. For the case of constructive interference of LOS path and ground reflected path, the links remains error free. However, for the destructive interference case, unacceptable low instantaneous modulation error ratio (MER) values and high bit error rate (BER) values occur even with a clearance greater than the 2nd Fresnel zone. To investigate the performance of radar systems under the effect of WT forward scatter, only point targets are taken into account. An S band marine radar fitted on a large cargo vessel is considered. A scenario based on almost destructive interference of LOS path and signal paths reflected at the sea surface has been chosen where a strong impact of rotor forward scattering on Doppler error is expected. The maximum of instantaneous two-way Doppler error ($\mid \Delta f_{D,\mathrm{two}} \mid$ = 214 Hz equivalent to an error in radial speed of 10 m/s) and the highest component (up to 175 Hz) in the time-frequency spectrum of the modulation signal occur where two blades are about tangential to the Fresnel zones. Principal results obtained are more general and – except for their different beam shape – do apply also to S band air search and weather radars.

The influence of important individual parameters on the forward scatter of a WT is then investigated, in order to outline the critical conditions for strongest impact. Link parameters like the frequency of operation, along with distances d_1 and d_2 determine the size of the Fresnel zones which determines the extent of obstruction these zones are subjected to. Wider antenna beams result in significant ground plane reflections. Along with the beam profile of the transmitting and receiving antenna, the nature of interference (constructive or destructive) between the direct and ground reflected signals is determined by their respective heights. Blade width determines the extent of shading observed in a Fresnel zone and can have a strong impact if it is close to the width of the Fresnel zone being tangentially obstructed. The impact of blade shape is governed by the actual blade width w_b at the tangential point with the Fresnel zones. As this point moves along the blade by rotor rotation the effectiveness of shading the Fresnel zones is a function of w_b. Blade pitch and yaw has a low impact except for very narrow zones, observed at short distances (small values of d_1, d_1) or with very wide beams. If the LOS path is aligned collinear with the rotor axis, maximum impact of blade pitch is in the order of a few tenths of a dB only. However, this would require a wide beam illuminating Fresnel zones of high order (n $>>$ 10) which is unrealistic

for radar applications. For varying values of yaw angle (γ), maximum obstruction loss occurs for $\gamma = 0°$. Large WT rotor diameters (or longer WT blades) increase the affected area and the number of Fresnel zones being obstructed, along with the speed at the blade tip. Consequently the error in measured radial speed by a radar system can increase for larger blade length l_b. Higher error in measured radial speed is also observed for higher rotational speed of the rotor which results in the Fresnel zones being traversed faster, which in turn increases the error in the measure radial speeds.

The investigation yields the result that the critical scenarios of WT forward scatter impact are due to

a) Destructive interference of the direct and ground reflected paths
b) Tangential obstruction of Fresnel zones by two blades at the same time

The destructive interference depends mainly on link parameters like frequency of operation, antenna beam profile and antenna heights and is not directly dependent on the positioning or orientation of the WT. Moreover, the worst impact of the destructive interference is observed when condition (b) is fulfilled. Therefore, the prime concern is to avoid the case when two rotor blades are tangentially obstructing the Fresnel zones at the same time. Using the information about the fraction of time where the rotor blades can tangentially obstruct the Fresnel zones, the possibility to avoid the strong impact conditions are investigated. It has been shown that the strongest impact of WT forward scatter can be avoided by maintaining a radial distance from the LOS path greater than twice the rotor blade length ($r_r \geq 2l_b$). This is an important conclusion, which defines the clearance zone in terms of WT rotor dimensions and not the traditional method of prescribing the clearance in terms of Fresnel zones. This is further emphasised by the fact that the Fresnel clearance for rectangular blades is higher than that prescribed for an obstructing half plane.

The discussion presented in this dissertation focuses on the impact of a single WT. A WT is typically not located just by itself but arranged in a wind farm. The principles applied in this research can be applied to characterize the impact of wind farms for limited scenarios, where all the WTs lie in one plane. For other wind farm configurations (where the WTs are not all in the same plane), the interference due to a WT is

impacted by the interference caused by all preceeding WTs. While this cascaded interference between WTs may not be comprehensively modeled, a good approximation of the impact of wind farms on radar and radio communication links may still be predicted using the methods described in this research.

Bibliography

[1] W. Yang, C. Qi and Y. Zhang, ”Evaluation on EM Scattering Properties from a Wind Farm by an Efficient High-Frequency Method,” in IEEE Access, vol. 6, pp. 32425-32429, 2018.

[2] G. J. Poupart, ”Wind Farms Impact on Radar Aviation Interests – Final Report”, DTI PUB URN 03/1294, 2006.

[3] C. M. Goodman, J. Wilson, R. Gillanders, W. Tywoniuk and W. W. Y. Kim, ”The wind energy industry; A global perspective”, Internal Report, Independent Contracting, Southern Alberta, Canada, Sep. 2013

[4] J. J. McDonald, B. C. Brock, S. E. Allen, P. G. Clem, J. A. Paquette, W. E. Patitz, W. K. Miller, D. A. Calkins, and H. J. Loui, ”Radar-cross-section reduction of wind turbines (Part 1) ”, Sandia National Labs, Rept. SAND2012-0480, Mar. 2012.

[5] B. S. Randhawa (ERA) and R. Rudd (Aegis), ”RF Measurement Assessment of Potential Wind Farm Interference to Fixed Links and Scanning Telemetry Devices” ERA Report No. 2008 – 0568 (issue 3), March 2009.

[6] D. Chisholm, A. Tommy and P. Curtis, ”Project Hayes: Compatibility with Radio Services”, Broadcast Communication Limited, July 2006.

[7] J. S. Bae, C. Dong-Guk, S. Y. Lee, C. Yoo and D. Kim, ”Preliminary study on a fabric-covered wind turbine blade,” 2015 International Conference on Renewable Energy Research and Applications

(ICRERA), Palermo, 2015, pp. 1196-1200.

[8] J. Xu and Z. Lu, "Application of fiber-reinforced composites in wind turbine blades," 2010 World Non-Grid-Connected Wind Power and Energy Conference, Nanjing, 2010.

[9] D. L. Sengupta and T. B. A. Senior, "Wind turbine generator sitting handbook", Technical Report No.2, University of Michigan, December 1979.

[10] D. L. Sengupta and T. B. A. Senior, "Wind Turbine Technology. Fundamental Concepts of Wind Turbine Engineering", Ed. ASME Press, ISBN No. 0-7918-1205-7, New York, 1994.

[11] "Procedure for coordination with wind energy developments", JRC Report Version 2.0.2, March 2010.

[12] J. Doble, "Introduction to Radio Propagation for Fixed and Mobile Communications", Artech House, ISBN 0-89006-529-2, 1996.

[13] J. D. Parsons, "The Mobile Radio Propagation Channel", Halsted Press (John Wiley and Sons), New York, 1992.

[14] J. A. Richards, "Radio Wave Propagation - An Introduction for the non-Specialist", Springer ISBN-13: 978-3540771241, 2008.

[15] J. D. Kraus and D. A. Fleisch "Electromagnetics with Applications", McGraw-Hill, New York 1999.

[16] M. I. Skolnik, "Introduction to Radar Systems," 3rd Edition, McGraw Hill, New York, 2001.

[17] W. Morchin, "Radar engineer's handbook", Artech House, Boston, London, 2013.

[18] E. F. Knott, J. F. Shaeffer and M. T. Tuley, "Radar Cross Section", Artech House Inc.,2004.

[19] G. Greving, W. D. Biermann and R. Mundt, "Wind turbines as distorting scattering objects for radar - clutter aspects and visibility," Radar Symposium (IRS), 2010 11th International , vol., no., pp.1-4, 16-18 June 2010.

[20] F. Pedrotti and L. Pedrotti, "Introduction to Optics", PTR Prentice Hall Inc., New Jersy, USA, 3rd ed., 2006.

[21] M. Born and E. Wolf, "Principles of Optics: Electromagnetic Theory of Propagation, Interference, and Diffraction of Light", New York, Pergamon Press, 1980.

[22] B. A. Davis and G. S. Brown, "Diffraction of a Randomly Rough Knife Edge," IEEE Transactions on Antennas and Propagation, AP-SO, 12, December 2002.

[23] H. L. Bertoni, "Radio Propagation for Modern Wireless Systems", Upper Saddle River, NJ, Prentice Hall, 2000.

[24] Y. Yuping, Z. Zhenwei, P. Ding and W. Li, "Influence of Gouy Phase Shift on THz Time-Domain Spectroscopy," 2006 Joint 31st International Conference on Infrared Millimeter Waves and 14th International Conference on Teraherz Electronics, Shanghai, 2006, pp. 547-547.

[25] I. Angulo et al., "Empirical evaluation of the impact of wind turbines on DVB-T reception quality," IEEE Trans. Broadcast., vol. 58, no. 1, pp. 1–9, Mar. 2012.

[26] "Interference to Fixed Links and Scanning Telemetry Devices", Ofcom Report 2008-0568, March 2009.

[27] M. Kazerne, ”Radar, Radio Links, and Wind Turbines”, 60th IEA Topical Expert Meeting, Senternovem, Netherlands, Nov. 18-19, 2009.

[28] F. Weinmann and J. Worms, ”Specialist Meeting about Electromagnetic Waves and Wind Turbines [Meeting Reports],” in IEEE Antennas and Propagation Magazine, vol. 59, no. 3, June 2017.

[29] M. Borely, “Guidelines on How to Assess the Potential Impact of Wind Turbines on Surveillance Sensors”, Eurocontrol, June 2010.

[30] T. Sellner and A. Zalay, ”TV/radio interference measurements for large commercially available MW class wind turbines”, Transmission and Distribution Conference and Exposition, 2008.T&D. IEEE/PES, April 2008.

[31] V. C. Chen, ”The micro Doppler Effect in Radar”, Artech House Boston, London, 2011.

[32] F. Weinmann, and J. Worms. ”Time-variant scattering properties of wind turbines.” Antennas and Propagation (EuCAP), 2015.

[33] O. A. Krasnov and A. G. Yarovoy, ”Polarimetric micro-Doppler characterization of wind turbines,” 2016 10th European Conference on Antennas and Propagation (EuCAP), Davos, 2016.

[34] A. Naqvi, N. Whitelonis, and H. Ling, “Doppler features from wind turbine scattering in the presence of ground,” in Proc. Int. Symp. Antennas Propagation. Soc. Res. Lett., vol. 35, Jul. 2012.

[35] I. Angulo, D. de la Vega, I. Cascón, J. Cañizo, Y. Wu, D. Guerra, P. Angueira, “Impact analysis of wind farms on telecommunication services”, Renewable and Sustainable Energy Reviews, Vol. 32, pp. 84-99, April 2014.

[36] Civil Aviation Authority, “CAP 764: CAA Policy and Guidelines on

Wind Turbines. UK Civil Aviation Authority", Fifth ed., June 2013.

[37] I. Angulo, U. Gil, D. de la Vega, Y. Wu, P. Angueira and C. Fernández, "First Results of a Field Trial to Evaluate the Impact of Wind Turbines on DTV Reception Quality", 2010 IEEE International Symposium on Broadband Multimedia Systems and Broadcasting (BMSB), pp.1-5, March 2010.

[38] Radio Advisory Board of Canada / Canadian Wind Energy Association, "Technical Information and Coordination Process Between Wind Turbines and Radiocommunication and Radar Systems," 2010.

[39] V. Yaramasu, B. Wu, P. C. Sen, S. Kouro, and M. Narimani, "High-power wind energy conversion systems: State-of-the-art and emerging technologies," Proceedings of the IEEE, vol. 103, pp. 740-788, May 2015.

[40] I. Angulo, D. de la Vega, O. Grande, Y. Wu, C. Fernandez, P. Angueira, J. L. Ordiales, "Methodology for the empirical analysis of the scattering signals from a wind turbine," Antennas & Propagation Conference, LAPC Loughborough 2009.16-17 Nov. 2009.

[41] J. Van den Berg, "Wind turbines and interference to broadcast signals"; 2012.

[42] International Telecommunication Union, Rec. ITU-R BT.805, "Assessment of impairment caused to television reception by a wind turbine", 1992.

[43] International Telecommunication Union, Document 6A/352-E, "The effect of the scattering of digital television signals from a wind turbine", April 2010.

[44] International Telecommunication Union, Document 6A/353-E, "Preliminary Draft New Recommendation ITU-R [WINTURB]. Assessment of impairment caused to digital television reception by a

wind turbine", April 2010.

[45] J. A. Fernandes, L. M. Correia, C. Alves, L. Pissarro, and M. Teixeira, "Assessment of wind turbines generators influence in VOR aeronautical navigation systems," in IEEE International Symposium on Antenna and Propagation, July 2014.

[46] I. Angulo, O. Grande and D. Jenn et. al., "Estimating Reflectivity Values from Wind Turbines for Analyzing the Potential Impact on Weather Radar Services", Atmos. Meas. Tech. 2015.

[47] P. Tristant, "Impact of wind turbines on weather radars band". World Meteorological Organization. CBS/SG-RFC 2006/Doc. 3.1; 2006.

[48] L. Claudepierre, R. Douvenot, A. Chabory and C. Morlaas, "Assessment of the shadowing effect between windturbines," 2015 9th European Conference on Antennas and Propagation (EuCAP), Lisbon, 2015.

[49] C. Morlaas, M. Fares and B. Souny, "Wind Turbine Effects on VOR System Performance", IEEE Transactions on Aerospace and Electronic Systems, Vol. 44, No. 4, pp. 1464-1476, October 2008.

[50] P. Tristant, "Impact of Wind Turbines on Weather Radars Band", World Meteorological Organization, CBS/SG-RFC 2006/Doc. 3.1, March 2006.

[51] "Impact of Wind Turbines on Weather Radars", OPERA II WP 1.8, December 2006.

[52] R. J. Vogt, T. D. Crum and M. J. B. Sandifer, "A Way Forward Wind Farm – Weather Radar Coexistence", NEXRAD Radar Operations Center, NOAA's National Weather Service, 2009.

[53] D. L. Sengupta and T. B. A. Senior, "Electromagnetic interference to television reception caused by horizontal axis windmills", Proc. of

the IEEE, Vol. 67, No. 8, August 1979.

[54] D. L. Sengupta and T. B. A. Senior, “Electromagnetic interference from wind turbines”, Chapter 9, pp. 447-486 from the book “Wind Turbine Technology. Fundamental Concepts of Wind Turbine Engineering”, Ed. ASME Press, ISBN No. 0-7918-1205-7, New York, 1994.

[55] M. Brenner, “Wind Farms and Radar,” JSR-08-126 prepared by The Mitre Corporation, January 2008.

[56] G. Greving, W. D. Biermann and R. Mundt, ”On the relevance of the measured or calculated RCS for objects on the ground-case windturbines,” Antennas and Propagation, 2009. EuCAP 2009. 3rd European Conference, vol. no. pp.2216-2220, 23-27 March 2009.

[57] D. de la Vega, D. Jenn, I. Angulo and D. Guerra, ”Simplified characterization of Radar Cross Section of wind turbines in the air surveillance radars band,” 2016 10th European Conference on Antennas and Propagation (EuCAP), Davos, 2016, pp. 1-5.

[58] I. Angulo, O. Grande and D. Jenn, “Estimating Reflectivity Values from Wind Turbines for Analyzing the Potential Impact on Weather Radar Services”, Atmos. Meas. Tech. 2015, vol. 8, pp. 2183-2193.

[59] F. Weinmann and J. G. Worms, ”EM scattering effects caused by wind turbines,” 2016 10th European Conference on Antennas and Propagation (EuCAP), Davos, 2016, pp. 1-5.

[60] P. Hamel, J. Adam, Y. Béniguel, G. Kubické and P. Pouliguen, ”Radar cross section evaluation of a wind turbine, based on an asymptotic method,” 2016 10th European Conference on Antennas and Propagation (EuCAP), Davos, 2016, pp. 1-3.

[61] L. R. Danoon and A. K. Brown, “Modeling Methodology for Computing the Radar Cross Section and Doppler Signature of Wind Farms,” Antennas and Propagation, IEEE Transactions on, On page(s):

5166-5174 vol. 61, Issue 10, Oct. 2013.

[62] B. M. Kent , K. C. Hill , A. Buterbaugh , G. Zelinski , R. Hawley , L. Cravens, Tri-Van, C. Vogel and T. Coveyou, "Dynamic radar cross section and radar Doppler measurements of commercial general electric windmill power turbines – Part 1: Predicted and measured radar signatures", IEEE Antennas Propag. Mag., vol. 50, no. 2, pp.211-219 2008.

[63] L. Danoon, W. Al-Mashhadani and A. Brown, "Modelling the impact of offshore wind farms on safety radars onboard Oil and Gas platforms," 2016 10th European Conference on Antennas and Propagation (EuCAP), Davos, 2016, pp. 1-5.

[64] O. A. Krasnov and A. G. Yarovoy, "Radar Micro-Doppler of Wind Turbines: Simulation and Analysis Using Slowly Rotating Linear Wire Structures," International Journal of Microwave and Wireless Technologies, vol. 7 pp. 459-467, June 2015.

[65] L. Claudepierre, R. Douvenot, A. Chabory and C. Morlaas, "A method for computing the VOR multipath error - comparisons with in-flight measurements," 2016 10th European Conference on Antennas and Propagation (EuCAP), Davos, 2016, pp. 1-5.

[66] M. Levent, I. Munro, "Effects of windmills on television reception", CBC technology review; 2006.

[67] J. J. Lemmon, J. E. Carroll, F. H. Sanders and D. Turner, "Assessment of the Effects of Wind Turbines on Air Traffic Control radars", NTIA Technical Report TR-08-454, July 2008.

[68] Finnish Meteorological Institute. EUMETNET OPERA PROGRAMME (2004– 2006) – Operational programme for the exchange of weather radar information, Final report; 2007.

[69] International Civil Aviation Organization, "European Guidance Material on Managing Building Restricted Areas", ICAO EUR Doc

015, September 2009.

[70] "Impact of Wind Turbines on Weather Radars", OPERA II WP 1.8, December 2006.

[71] F. Kong, Y. Zhang and R. Palmer, "Wind Turbine Clutter Mitigation for Weather Radar by Adaptive Spectrum Processing", In Proceedings of the 2012 IEEE Radar Conference, Atlanta, GA, USA, 7–11 May 2012; pp. 471–474.

[72] S. Hegler, K. Wolf, C. Statz, N. Neumann and D. Plettemeier, "Investigation of the RCS of wind turbine rotor blades," 2018 International Applied Computational Electromagnetics Society Symposium (ACES), Denver, CO, 2018.

[73] R. M. Beauchamp and V. Chandrasekar, "Suppressing Wind Turbine Signatures in Weather Radar Observations," in IEEE Transactions on Geoscience and Remote Sensing, vol. 55, no. 5, pp. 2546-2562, May 2017.

[74] A. Belmonte, X. Fabregas, "Analysis of Wind Turbines Blockage on Doppler Weather Radar Beams," Antennas and Wireless Propagation Letters, IEEE, vol.9, no., pp.670-673, 2010.

[75] B. S. Randhawa, R. Rudd, "RF Measurement Assessment of Potential Wind Farm Interference to Fixed Links and Scanning Telemetry Devices," ERA Technology Ltd, Surrey, UK, 2008.

[76] G. Greving, W. Biermann and R. Mundt, "Wind turbines as distorting scattering objects for radar-Visibility, desensitization and shadowing, 13th International Radar Symposium (IRS), Warsaw 2012.

[77] S. Coutts, J. Eisenman, J. K. Jao, S. Rodriguez and W. Lee, "Wind turbine measurements and scattering model validation in the high frequency band (3-30 MHz)," 2018 IEEE Radar Conference (RadarConf18), Oklahoma City, OK, 2018.

[78] J. Bredemeyer, T. Schrader and S. Sandmann, "Measurements for Classification of Single Wind Turbine Echoes," 2018 19th International Radar Symposium (IRS), Bonn, 2018, pp. 1-10.

[79] R. Geise, B. Neubauer, G. Zimmer, A. Enders and N. Yonemoto, "An overview of scattering measurements of scaled dynamic wind turbines in the context of navigation systems," 2017 IEEE Conference on Antenna Measurements & Applications (CAMA), Tsukuba, 2017.

[80] C. Neumann and M. Steck, "Wind Turbine impact to ATC radars - an assessment approach," 2017 18th International Radar Symposium (IRS), Prague, 2017, pp. 1-9.

[81] W. Al-Mashhadani et al., "Measurements and modelling of radar signatures of large wind turbine using multiple sensors," 2018 IEEE Radar Conference (RadarConf18), Oklahoma City, OK, 2018.

[82] R. Geise, B. Neubauer, G. Zimmer, A. Enders and N. Yonemoto, "An overview of scattering measurements of scaled dynamic wind turbines in the context of navigation systems," 2017 IEEE Conference on Antenna Measurements & Applications (CAMA), Tsukuba, 2017.

[83] A. Naqvi, S. Yang and H. Ling, "Investigation of Doppler Features From Wind Turbine Scattering," in IEEE Antennas and Wireless Propagation Letters, vol. 9, pp. 485-488, 2010.

[84] Y. Zhang et.al., "Wind Turbine Radar Signature Characterization by laboratory measurements", Radar Conference(RADAR), IEEE Transactions on, pp. 162-166, 2011.

[85] I. Gonzalez, L. Lozano, J. Gomez, A. Tayebi, I. Etayo and M. Catedra, "Analysis of the scattering field of wind turbine using rigorous and asymptotic techniques," in Proceedings of the Fourth European Conference on Antennas and Propagation (EuCAP), April 2010.

[86] M. B. Raza and T. Fickenscher , "Investigating the Radar Returns of a Wind Turbine", Progress in Electromagnetics Research Symposium

PIERS 2013, Taipei Taiwan March 25-28, 2013.

[87] M. J. Algar, L. Lozano, J. Moreno, I. Gonzalez and F. Catedra,"Application of asympototic and rigorous techniques for the characterization of interferences caused by a wind turbine in its neighborhood," Int. J. Antennas Propagation, vol. 2013, 2013.

[88] A. Calo Casanova, M. Ramon, L. de Haroy Ariet and P. Blanco-Gonzalez, "Wind farming interference effects," in International MultiConference on Systems, Signals and Devices, July 2008, pp. 1–6.

[89] D. de la Vega, C. Fernandez, O. Grande, I. Angulo, D. Guerra, Y. Wu, P. Angueira and J. Ordiales, "Software tool for the analysis of potential impact of wind farms on radiocommunication services," in IEEE International Symposium on Broadband Multimedia Systems and Broadcasting (BMSB), June 2011, pp. 1–5.

[90] J. A. Fernandes, L. M. Correia, C. Alves, L. Pissarro and M. Teixeira, "Assessment of wind turbines generators influence in VOR aeronautical navigation systems," in IEEE International Symposium on Antenna and Propagation, July 2014.

[91] F. Weinmann, "Accurate Prediction of EM Scattering by Wind Turbines," EuCAP 2014 8th European Conference on Antennas and Propagation, 6-11 April 2014, The Hague, Netherlands.

[92] F. Weinmann and J. G. Worms, "Time-variant Scattering Properties of Wind Turbines," EuCAP 2015 9th European Conference on Antennas and Propagation, 13-17 April 2015, Lisbon, Portugal.

[93] W. Yang, C. Qi and Y. Zhang, "Evaluation on EM Scattering Properties From a Wind Farm by an Efficient High-Frequency Method," in IEEE Access, vol. 6, pp. 32425-32429, 2018.

[94] E. Aarholt and C. A. Jackson, "Windfarm gapfiller concept solution" in Proceedings of the 2010 European Radar Conference (EuRAD)

2010.p.236–9.

[95] F. Kong, Y. Zhang and R. Palmer, ”Wind Turbine Clutter Mitigation for Weather Radar by Adaptive Spectrum Processing. In Proceedings of the 2012 IEEE Radar Conference, Atlanta, GA, USA, 7–11 May 2012; pp. 471–474.

[96] L. Danoon and A. K. Brown, “Modeling methodology for computing the radar cross section and Doppler signature of wind farms,” IEEE Trans. Antennas Propagation, vol. 61, pp. 5166-5174, Oct. 2013.

[97] P. Hamel, J.-P. Adam, G. Kubické and P. Pouliguen, “Design of a stealth wind turbine,” Antennas and Propagation Conference (LAPC), 2012 Loughborough, Nov. 2012, doi: 10.1109/LAPC.2012.6403021.

[98] L. S. Rashid and A. K. Brown, ”Radar cross-section analysis of wind turbine blades with radar absorbing materials,” Radar Conference (EuRAD), 2011 European , vol., no., pp.97-100, 12-14 Oct. 2011.

[99] L. Sergey, O. Hubbard, Z. Ding, H. Ghadaki, J. Wang and T. Ponsford, ”Advanced mitigating techniques to remove the effects of wind turbines and wind farms on primary surveillance radars,” 2008 IEEE Radar Conference, Rome, 2008, pp. 1-6.

[100] L. Danoon and A. Brown, ”Reducing the effect of offshore wind farms on the REWS CFAR detection threshold,” 2018 22nd International Microwave and Radar Conference (MIKON), Poznan, 2018.

[101] VINDRAD. Project report v1.0, ”A tool for calculation of interference from wind power stations to weather radars ”; 2011.

[102] D. F. Bacon, “Fixed-link wind-turbine exclusion zone method”, OFCOM, October 2002.

[103] S. -T. Yang and H. Ling, “Electromagnetic Simulation of the Near-Field Distribution around a Wind Farm,” International Journal

of Antennas and Propagation, vol. 2013, Article ID 105071, 9 pages, 2013.

[104] C. A. Balanis, "Edge diffraction and field transition along shadow boundaries using UTD," 2008 IEEE Antennas and Propagation Society International Symposium, San Diego, CA, 2008.

[105] D. Bouche, F. Molinet, R. Mittra, "Asymptotic Methods in Electromagnetics," Springer Science & Business Media, 2005.

[106] U. Jakobus, J. van Tonder and F. Illenseer, "Overview of Recent Extensions in FEKO with Regard to the MLFMM and Cable Coupling," 2007 2nd International ITG Conference on Antennas, Munich, 2007.

[107] T. Rylander, P. Ingelström, A. Bondeson, "Computational Electromagnetics", Springer Science & Business Media, 2012.

[108] P. R. Foster, "The region of application in GTD/UTD," 1996 Third International Conference on Computation in Electromagnetics (Conf. Publ. No. 420), Bath, UK, 1996, pp. 382-386.

[109] J. B. Keller, "Geometrical theory of diffraction," J. Opt. Soc. Amer., vol. 52, no. 2, pp. 116-130, February 1962.

[110] T. Fickenscher and M. B. Raza, "Diffraction Loss and Phase Modulation of Terrestrial Radio-Link by Wind Turbine," International Workshop on Antenna Technology iWAT 2014, Sydney March 4-6, 2014.

[111] T. Fickenscher and M. B. Raza, "Impact of Ground Plane on Wind Turbine Forward Scattering", International Workshop on Antenna Technology iWAT 2015, Seoul March 6-9, 2015.

[112] M. B. Raza and T. Fickenscher, "2D Fresnel Diffraction Approach for Wind Turbine Forward Scattering", German Microwave Conference

GeMiC 2015, Nürnberg March 16-18, 2015.

[113] A. Fourie and D. Nitch, "SuperNEC: antenna and indoor-propagation simulation program," in IEEE Antennas and Propagation Magazine, vol. 42, no. 3, pp. 31-48, June 2000.

[114] U. Jakobus, A. Aguilar, E. Attardo, M. Schoeman, J. van Tonder and K. Longtin, "Review of selected new features in FEKO 2018," 2018 International Applied Computational Electromagnetics Society Symposium (ACES), Denver, CO, 2018.

[115] C. Anjana and G. A. S. Sundaram, "Simulating the impact of wind turbine on RADAR signals in L and S band using XGtd," 2015 International Conference on Communications and Signal Processing (ICCSP), Melmaruvathur, 2015.

[116] F. Cátedra et al., "Useful techniques included in NEWFASANT tool for electromagnetic analysis and design," Proceedings of the 2012 IEEE International Symposium on Antennas and Propagation, Chicago, IL, 2012.

[117] M. B. Raza and T. Fickenscher, "Radar Doppler Deviation by Wind Turbine", International Radar Symposium IRS 2014, Gdansk, June 16-18, 2014.

[118] M. B. Raza and T.Fickenscher , "Time Frequency Spectrum and Path Loss by Wind Turbine Forward Scattering", Progress in Electromagnetics Research Symposium PIERS 2014, Guangzhou August 25-28, 2014.

[119] Measurement Guidelines for DVB systems, ETSI Technical Report, TR101 290 V1.2.1 (2001-05) Digital Video Broadcasting (DVB); European Telecommunications Standard Institute.

[120] Digital Video Broadcasting (DVB); Framing structure, channel coding and modulation for cable systems EN 300 429 V1.2.1 (1998-04)

European Standard (Telecommunications series).

[121] M. B. Raza and T.Fickenscher , "Impact of Wind Turbine Rotor Forward Scattering on 16-QAM Based Communication System", International Symposium on Antennas and Propagation ISAP 2015, Hobart 9-12th November 2015.

[122] T. Fickenscher and M. B. Raza, "A Comprehensive Understanding of the Forward Scattering of Radar Signals at the Rotor of a Wind Turbine", International Radar Symposium IRS 2015, Dresden June 24-26, 2015.

[123] T. Fickenscher and M. B. Raza, "Interaction of Tower and Rotor of a Wind Turbine in the Context of Diffraction", International Conference on Antenna Measurements & Applications CAMA 2015, Chiang Mai, November 30-December 2, 2015.

[124] T. Fickenscher and M. B. Raza, "Obstruction of Fresnel Zones by Wind Turbine on Illuminated Ground Plane", European Conference on Antennas and Propagation EuCAP 2016, Davos, April 10-15, 2016.

[125] T. Fickenscher and M. B. Raza, "Analytical Investigation of Diffraction at Multiple Blades of Wind Turbine Rotor", European Microwave Week EuMW 2016, London October 3-7, 2016.

[126] M. B. Raza and T. Fickenscher, "Impact of Blade Shape and Pitch Angle on Wind Turbine Forward Scattering", ICEAA - IEEE APWC 2016, Cairns, September 19 -23.

[127] M. B. Raza and T. Fickenscher, "Impact of off-shore wind turbine on forward scattering of marine radar signals", 2017 IEEE MTT-S International Microwave Symposium (IMS), Honololu, HI, 2017, pp. 894-896.

[128] M. B. Raza and T. Fickenscher, "Impact of yaw angle of wind turbines on diffraction loss of radar signals", 2017 International

Symposium on Antennas and Propagation (ISAP), Phuket, 2017.

[129] J. Großkopf, "Wellenausbreitung I", Hochschultaschenbuchverlag, Mannheim 1970.

[130] R. S. Longhurst, "Geometrical and Physical Optics",London, Prentice Hall Press, 1967.

[131] S. V. Hum, "Diffraction", Technical note, University of Toronto , ECE 422: Radio and Microwave Wireless Systems.

[132] H. Lehpamer, "Wind Farms and Microwave Links," 2013 ENTELEC, Houston, Texas.